SYNAPTIC ACTIVITY OF AUDITORY AND VESTIBULAR HAIR CELLS

by

Viviana L Davila

A DISSERTATION

Presented to the Neuroscience Graduate Program
and the Oregon Health & Sciences University
School of Medicine
in partial fulfillment of
the requirements for the degree of
Doctor of Philosophy
December 2006

School of Medicine
Oregon Health & Science University

CERTIFICATE OF APPROVAL

This is certify that the Ph.D. dissertation of

Viviana Davila

has been approved

[redacted]

Wolf Almers

[redacted]

Peter Gillespie

[redacted]

Edwin McCleskey

[redacted]

Teresa Nicolson

[redacted]

John Williams

TABLE OF CONTENTS:

CHAPTER I: The inner ear and hair cell resonant frequency

Introduction:

CHAPTER II: The afferent synapse

Introduction:

Results:

Discussion:

CHAPTER III: The efferent synapse

Introduction:

Results:

Discussion:

CHAPTER IV: Calcium noise and non-voltage gated calcium flux

Introduction:

Results:

Discussion:

SUMMARY AND CONCLUSIONS:

MATERIALS AND METHODS:

APPENDICES:

LIST OF TABLES:

LIST OF FIGURES:

LIST OF ABBREVIATIONS:

α-BTX	alpha-bungarotoxin
ACh	acetylcholine
AOTF	acoustic optical tunable filter
ATP	adenosine triphosphate
ATPase	adenosine triphosphatase
Ba^{2+}	barium
BAPTA	1,2-bis(2-aminophenoxy)ethane N,N,N',N'-tetraacetic acid
BK channel	large-conductance calcium-sensitive potassium channel
BSA	bovine serum albumin
Ca^{2+}	calcium
CCHC	central cylindrical hair cell
CFHC	central flask-shaped hair cell
CGRP	calcitonin gene-related peptide
ChAT	cholineacetyltransferase
CICR	calcium-induced calcium release
CRAC	calcium release-activated calcium current
Cs^{2+}	cesium
CtBP	C-terminal binding protein
CV	coefficient of variance
ΔC_m	change in membrane capacitance
$\Delta F/F_0$	change in fluorescence over initial fluorescence
DIC	differential interference contrast
DNase	deoxyribonuclease
E_{ion}	reversal potential for a given ion
EGTA	ethylene glycol-bis(aminoethylether) N,N,N',N'-tetraacetic acid
EM	electron microscopy
EPSC	excitatory post-synaptic potential
ER	endoplasmic reticulum
EtOH	ethanol
GABA	γ-aminobutyric acid

G-protein	GTP-binding regulatory protein
GTP	guanosine triphosphate
IACUC	Institutional Animal Care and Use Committee
IHC	inner hair cell
I_{hold}	holding current
I_K	voltage-sensitive delayed rectifier potassium channel
IP_3	inositol-1,4,5- triphosphate
IP_3R	inositol triphosphate receptor
IV plot	current to voltage plot
K^+	potassium
K_V	voltage-sensitive potassium channel
LCS	low calcium saline
mRNA	messenger ribonucleic acid
Na^+	sodium
nAChR	nicotinic acetylcholine receptor
NCX	sodium-calcium exchanger
NMG+	*N*-methyl-D-glucamine
OHC	outer hair cell
PMCA	plasma membrane calcium ATPase
ROI	region of interest
RRP	ready-releasable pool
RT	room-temperature
RyR	ryanodine receptor
SD	standard deviation
SE	standard error
sER	smooth endoplasmic reticulum
SERCA	sarcoplasmic endoplasmic reticulum calcium ATPase
SHC	short hair cell
SOC	store-operated calcium channel
SOCE	store-operated calcium entry
TEA	tetraethylammonium ion
THC	tall hair cell

TIRF	total internal reflection fluorescence
TRPV	transient receptor potential vanilloid (channel)
VGCC	voltage-gated calcium channel

ACKNOWLEDGEMENTS and *thanks*...

Many thanks go to Dr. Wolfhard Almers for his patience while carrying out this work and to all who have participated as committee members over the years:
Dr. Peter Gillespie, Dr. Edwin McCleskey, Dr. Teresa Nicolson, Dr. John Williams,
Dr. Paul Fuchs, Dr. Craig Jahr and Dr. Henrique von Gersdorff.
I am indebted to them for their encouragement and support of the work presented here.

The work on both bullfrog saccular and chick cochlear hair cells would not have possible without the generous direction from Drs. Peter Gillespie and Paul Fuchs, respectively, on cell isolation procedures and enthusiastic discussion about the results.

Immunofluorescent labeling of hair cells with CtBP antibody was expertly done by Dr. Lei Wan.
Electron microscopy was skillfully made possible by Michael Webb.

Fellow lab members and friends: Drs. Sebastian Barg, Trillium Blackmer, Xi Chen, Felix Felmy, (soon-to-be Dr.) Jeff Hubbard, Michelle Knowles, Jose-David Machado, Christien Merrifield, David Perrais, Justin Taraska, Oleg Varlamov, Lei Wan, Wei-Hong Xiong and David Zenisek, Johnny Powell and Steve Arch have been wonderful colleagues and have all contributed in my learning experiences during my time in graduate school.

To everybody in the "front office" who took care of all the paperwork and particulars and to Liz Lawson-Weber who has been simply amazing and helpful.

I also want to thank my dear friends without whose care and support I could not have persevered these eight long years: My former roommate, fellow NGP student and friend Lisa L., Lisa A., Sarah H., Satinder S., Meg B. and Jen A.
and to my wonderful husband Miten who kept me fed, made me chai and gave me endless hugs when I was glued to the computer and would have starved otherwise.

Thanks and gratitude also goes to my former boss and friend Dr. David Sulzer who encouraged me by graciously giving me the opportunity to carry out my own projects. I would not have even made it to graduate school without his support.

To my mother and my father, for their courage to move away from the familiar and establish a life for themselves in a new country. For their perseverance, ingenuity, sacrifice and unyielding resolve to maintain hope. I am inspired by your example and keep you in my heart always.
I love you mom! I love you dad!

To my Grandparents, whom I know have been
with me during the most difficult times

ABSTRACT

Hair cells of the auditory and vestibular organs in the inner ear sense information about sound and movement in space, respectively. Head tilt or sound waves are sensed by movement of hair bundles, which are located at the apical end of hair cells; here, mechanical information is translated into an oscillating membrane voltage in the basolateral cell surface. Receptor potentials can then transmit sensory information to the brain through ribbon-type afferent synapses, dense bodies in hair cells, where voltage gated calcium channels (VGCC) congregate and synaptic vesicle exocytosis and release of neurotransmitter presumably occurs. However, hair cell activity can also be modulated by a cholinergic efferent input from the brain that, in most hair cells, causes membrane hyperpolarization and dampened activity at the afferent synapse.

Various aspects of hair cell activity such as synaptic vesicle exocytosis and VGCC activity at presumed afferent synapse sites, as well as the role of calcium at the efferent synapse, were explored in this thesis. Hair cells from either the vestibular bullfrog sacculus or the auditory chick cochlea were acutely dissociated and plated onto glass wells. Various electrophysiological methods such as membrane capacitance, current, and voltage clamp recordings were used to measure cell activity. Electrophysiological recordings were sometimes used in tandem with total internal reflection fluorescence (TIRF) microscopy, a fluorescence imaging method that effectively limits illumination to within 100 nm of the cell surface. Use of both methods together allows one to monitor synaptic vesicle exocytosis, ion channel activity and

transient, local increases in calcium concentration at the plasma membrane concurrently.

Three observations regarding vesicular activity at the afferent synapse of bullfrog saccular hair cells are that, 1) two rates of exocytosis could be generated depending on stimulus duration, 2) an increase in extracellular calcium increases the number of vesicles that undergo stimulated exocytosis, and 3) a basal oscillation in membrane voltage close to the gating potential of the voltage-gated calcium channel found in these cells may support stochastic exocytosis. One observation regarding the efferent synapse of bullfrog saccular hair cells was that only inward currents could be generated upon acetylcholine application at resting membrane voltage. On the other hand, acetylcholine application onto chicken cochlear hair cells generates a voltage-sensitive outward current at resting membrane voltage that reverses close to the reversal potential of potassium. The reversal potential of the acetylcholine response in chicken cochlear hair cells could be shifted closer to the reversal potential of calcium when the calcium buffer EGTA was replaced with BAPTA, a calcium buffer with faster binding kinetics. Finally, some observations in both bullfrog saccular and chicken cochlear hair cells indicate the presence of calcium noise or a non-voltage-gated calcium flux at the membrane. Some of the differences between bullfrog saccular and chicken cochlear hair cells, particularly at the efferent synapse, may reflect differences in how hair cells in each sensory system may process sensory information. Overall, these observations can provide clues to further understanding of hair cell synaptic physiology in both the vestibular and auditory systems.

CHAPTER I: The inner ear and hair cell resonant frequency

INTRODUCTION

Sensory organs of the inner ear and innervation:

The senses of hearing and of balance are dependent on the activity of mechanosensory cells called hair cells, which reside in six sensory organs that comprise the inner ear. These organs are divided into two major sensory systems, the auditory and the vestibular systems. The auditory organ for hearing is called the cochlea; the five major vestibular organs are the sacculus, which senses vertical movements and low-frequency vibrations, the utriculus, which senses lateral movement, and the three semi-circular canals, which sense angular acceleration in three orthogonal planes (Fig. 1). The equivalent sensory organ for the mammalian cochlea is the basilar papilla in birds and turtles. The structures where hair cells sit in the sacculus and utriculus and of the semi-circular canals are called the macula and crista, respectively. Detection of auditory or vestibular stimuli begin with the translation of sound or head-tilt into the movement of otoconia and consequent movement of a tectorial or otolithic membrane, which directly moves the hair bundles which protrude from the apical ends of hair cells. In the cochlea, various frequencies of sound or ground-borne vibrations are selectively distributed along the sensory epithelium in a tonotopic fashion. The vestibular sensory organs are, however, primarily sensors of linear or angular acceleration where all cells are exposed to the same stimulus without tonotopy. Hair cells then communicate sensory input to the central nervous system by the release of an excitatory neurotransmitter, presumably glutamate (Eybalin, 1993), onto afferent fibers that traverse the 8th nerve to nuclei in the brainstem. The signal from hair cells can also be reciprocally modified by inhibitory efferent fibers, primarily cholinergic (Flock and Lam, 1974), which emanate from the brainstem (Precht et al., 1974) or cerebellum (Llinas and Precht, 1969; Hillman, 1969). Efferent fibers contact either the basolateral hair cell surface or contact afferent fibers themselves and are found in both auditory (Wiederhold, 1970; Art et al., 1985) and vestibular (Goldberg and Fernandez, 1980; Gribenski and Caston, 1976) sensory organs.

Hair cell shape and innervation of the cochlea and sacculus:

In the mammalian organ of Corti, hair cells are physically divided into two populations and are referred to as the inner and outer hair cells (IHC and OHC, respectively). In the chicken basilar papilla (Fig. 2a, b), there are also two types of hair cell, the tall and short hair cells (THC and SHC, respectively), which are thought to be functionally equivalent to the inner and outer hair cells, respectively (Manley et al., 1989; Spoendlin, 1972). The THC and SHCs vary in cell shape in a graded fashion along the sensory epithelium where the THC to SHC ratio is higher towards the neural apical end and vice versa towards the abneural basal end (Takasaka and Smith, 1971; Tanaka and Smith, 1978) (Fig. 3a). THCs are thought to be the output cells as they are primarily contacted by afferent fibers; by contrast, efferent input is more prevalent among the SHC population (Hirokawa, 1978; Fischer, 1992). Still, gradients of both afferent and efferent innervation exist along the sensory epithelium where some THCs have a few efferent contacts and some SHCs are contacted by a few or no afferent fibers (Rebillard and Pujol, 1983; Hirokawa, 1978) (Fig. 3b). In the organ of Corti, whereas OHCs maintain efferent contact through adulthood (Dulon and Lenoir, 1996), direct efferent innervation of IHCs is lost during the development of the rat (Uziel et al., 1981; Katz et al., 2004). A greater number of afferent fibers are modulated by a relatively smaller number of efferent fibers in the cochlea and vestibule of the cat (Warr, 1975).

In the bullfrog sacculus (Fig. 4a, b), hair cell types of at least three distinct shapes co-exist within the sensory macula (Chabbert, 1997). However, the hair cells of the sacculus appear to be more homogeneously distributed than the IHC and OHCs of the organ of Corti. Saccular hair cells communicate with multiple afferent fibers and, in possibly only one of the cell types, are also contacted by multiple efferent fibers sometimes even in close proximity to the afferents (Lenzi and Roberts, 1994, review) (Fig. 5a, b).

The auditory and vestibular sensory organs mediate a considerable amount of signal processing before sensory information is sent to the brain. Hair cells themselves play an active role in modifying sensory input to increase the effectiveness of auditory and vestibular signal detection. The focus of this thesis is to describe synaptic activity at both the afferent and efferent synapses of hair cells. Since auditory stimuli and intrinsic behavior of hair cells are oscillatory by nature, frequency detection and the generation of resonant frequency will be briefly summarized. Two model preparations, dissociated hair cells from the bullfrog sacculus (Fig. 4) or the chick basilar papilla (Fig. 2) were used in these studies and will be the focus for the remainder of this chapter with some reference to the mammalian cochlea for comparison.

Frequency detection in the cochlea and sacculus:

The sensory epithelia of the mammalian and non-mammalian cochlea or sacculus are structured in such a way as to detect sound or movement in space. Hair cells possess several methods to amplify sounds of low energy in a frequency selective manner. One is by physically exposing hair cells to a graded distribution of tones due to a graded stiffness of the basilar membrane (von Bekesy, 1960; Crawford and Fettiplace, 1983). Another method of amplification is by active amplification by the hair bundle (Hudspeth, 1997). In the case of non-mammalian organisms, resonating ionic conductances on the basolateral membrane is a third method by which hair cells can amplify sound. Electrical resonance, however, has not been demonstrated in the mammalian cochlea (Kros and Crawford, 1990).

Electrical resonance allows the hair cells of non-mammalian organisms to respond best to certain frequencies and is called the resonant, “best” or “characteristic” frequency of a given cell. This phenomenon has been shown in the frog sacculus (Ashmore, 1983; Lewis and Hudspeth, 1983), the goldfish sacculus (Sugihara and Furukawa, 1989), in the turtle basilar papilla (Crawford and Fettiplace, 1981) and the chick basilar papilla (Fuchs et al., 1988). In the basilar papilla of the chick, a gradient of hair cells with resonant frequencies varying from 50 to 5000 Hz (Gray and Rubel, 1985; Manley, 1996) exists in a tonotopic arrangement along the length of the sensory epithelium (Manley et al., 1987). Tonotopy of electrical resonance has also been demonstrated in the basilar papilla of the turtle (Crawford and Fettiplace, 1980; Hudspeth, 1989, review; Fettiplace and Fuchs, 1999, review). In the chick, cell body shape is also correlated with resonant frequency (Smith, 1961 & 1968) (Fig. 6).

In the frog sacculus, no tonotopy has been observed. Rather, all hair cells are exposed to frequencies between 15-200 Hz, useful for detecting rapid movements and ground-borne vibrations (Koyama et al., 1982; Lewis et al., 1982). Even still, there happens to be some non-tonotopically arranged variation in electrical resonance between saccular hair cells. Immunocytochemical and electrophysiological data suggest that at least three types of hair cell can be found in the bullfrog saccular macula each in possession of distinct ionic properties and cell shape (Chabbert, 1997) (Fig. 7).

Since this thesis is focused on the synaptic activities of hair cells in the bullfrog sacculus and chick basilar papilla, where electrical resonance is a major feature of their ionic activity, electrical resonance will be further described.

Resonant frequency in non-mammalian hair cells:

There are primarily two types of ion channel which together generate the oscillatory behavior of hair cells, the voltage-gated calcium channel (VGCC) and large-conductance calcium-sensitive potassium channel (BK). The VGCC and BK channels are found clustered at afferent synapse sites where hair cells communicate information about sensory activity to the brain in turtle basilar papilla (Art and Fettiplace, 1987), frog sacculus (Issa and Hudspeth, 1994; Roberts et al., 1990), and chicken basilar papilla (Fuchs and Evans, 1990; Zidanic and Fuchs, 1995) (Fig. 8). During sound detection, excitatory hair bundle deflection generates a graded membrane depolarization that activates the L-type calcium channels, permitting calcium ion entry and consequent synaptic vesicle exocytosis. The microdomain of elevated calcium concentration following calcium influx also activates nearby BK channels, which in turn hyperpolarize the cell via potassium ion efflux; this terminates stimulated exocytosis (Roberts et al., 1991, review). The regenerative oscillation that arises by alternating depolarizing and hyperpolarizing currents from alternating L-type calcium and BK potassium channel gating, initiated either by bundle deflection or current injection, comprises the mechanism of electrical resonance.

The VGCC at the afferent synapse of hair cells most resembles the L-type calcium channel (Nowycky et al., 1985) but differs from typical L-type currents in that it is gated at relatively hyperpolarized potentials (-50 mV), does not inactivate, quickly reactivates with repolarization, and is sensitive to cadmium or dihydropyridines, such as nifedipine, in turtle (Art and Fettiplace, 1987), in frog (Roberts et al., 1990) and in chick (Zidanic and Fuchs, 1995). The hair cell L-type calcium channel belongs to the $Ca_v1.3$ family (Brandt et al., 2003) and consists of four subunits, α_1, β, γ and $\alpha_2\delta$ (Catterall, 2000, review). The pore of the hair cell L-type calcium channel is formed by the α_{1D} subunit (Kollmar et al., 1997). The BK potassium channels are part of a family of calcium-sensitive potassium channels that are sensitive to charybdotoxin, iberiotoxin, cesium and TEA. These channels are named for their large potassium currents and are composed of α- and β-subunits (Vergara et al., 1998, review). The α-subunit of the pore is encoded by the *slo* gene, first identified in Drosophila (Atkinson et al., 1991).

Each hair cell possesses a characteristic resonant, or best, frequency that allows it to amplify low energy sounds of the same frequency. The resonant frequency of a given hair cell depends upon a number of factors. Electrophysiological studies of membrane patches demonstrate that L-type calcium and BK channels are found clustered at a fixed 2:1 ratio of L-type calcium channels relative to BK potassium channels in turtle (Art et al., 1993), and in frog (Roberts et al., 1990) (Fig. 8). The overall number of L-type calcium and BK channels varies from cell to cell (Fig. 9) in a graded fashion along the length of the auditory epithelium (Art et al., 1993) where a total increase in both L-type calcium and BK channel numbers corresponds to an increase in the resonant frequency (Art and Fettiplace, 1987). Additionally, the gating kinetics of the type of L-type or BK channel relates to the resonant frequency. Single-cell biochemical experiments in the chick basilar papilla indicate the presence of distinct α_{1D} (Kollmar et al., 1997) and BK channel mRNA splice variants (Rosenblatt et al., 1997; Navaratnam et al., 1997; Jiang et al., 1997), each with slightly different kinetics. Splice variants of the BK channel α-subunit have also been described in turtle basilar papilla (Jones et al., 1998). Evidence also exists for splice variants of the β subunit of BK channels in chick cochlear hair cells found near the apex of the sensory epithelium (Ramanathan et al., 1999) and in turtle (Jones et al., 1999).

In the bullfrog sacculus, where low frequency sounds are sensed, a voltage-sensitive potassium channel (K_V) also takes part in generating lower frequency membrane resonances (Armstrong and Roberts, 1998). Furthermore, in the intact turtle basilar papilla, electrical resonances of <60 Hz were also found to be mediated by a type of K_V channel instead of BK channels (Goodman and Art, 1996). The kinetics of K_V channel activation is slower than the BK channel and therefore will generate lower frequency oscillations. A voltage-sensitive delayed potassium rectifier (I_K) has also been described in the chick with more frequent expression in cells located towards the apex which exhibit lower resonant frequencies (Fuchs and Evans, 1990). Therefore, the number of L-type calcium and BK channels and the splice variant for either that are expressed can influence the resonant frequency of a given hair cell. Extended variations toward lower resonant frequencies can also be generated in those cells which express the K_V or I_K channel.

Since the combination of L-type calcium, BK potassium channels and K_v channels have a strong effect on the membrane voltage and on calcium influx at the afferent synapse, it follows that vesicle release is related to the resonant frequency of a given hair cell.

CHAPTER II: The afferent synapse

INTRODUCTION

Afferent synapse architecture:

In addition to L-type calcium and BK potassium channels, the afferent synapse is identified by the presence of a spherical or rod-shaped ribbon-type structure called the "dense-body" in hair cells. The dense body is similar to the ribbon structure found in the retina, where graded membrane voltages also stimulate exocytosis (Lenzi and von Gersdorff, 2001). Typically 18 to 20 dense bodies are distributed along the hair cell basolateral membrane in the frog sacculus, with a slightly higher concentration towards the most basal end below the nucleus (Roberts et al., 1990; Issa and Hudspeth, 1994; Zenisek et al., 2003). In turtle, it was estimated from confocal calcium imaging that about 6 dense bodies are present (Tucker and Fettiplace, 1995). In goldfish saccular hair cells, 5-7 dense bodies are seen (Hama and Saito, 1977). In chick, dense body number varies from cell to cell along the basilar papilla with higher numbers among the THC population (Martinez-Dunst et al., 1997).

A wide range in dense body diameter, 0.2 to 1 μm, has been observed in hair cells of different animals; they can be up to ten times larger than those found in retinal bipolar cell terminals. Dense body diameter can vary even within an individual sensory organ as in the basilar papilla of the chick, where dense body size varies between hair cells along the length of the sensory epithelium (Martinez-Dunst et al., 1997). Dense body size is related to the exocytic activity of hair cells since the dense body, as is the ribbon, is studded with and surrounded by a cloud of small, clear synaptic vesicles as observed in images using electron microscopy (Hama and Saito, 1977) and electron tomography (Lenzi et al., 1999) of frog saccular hair cells. The reported synaptic vesicle diameters range from 25-50 nm in bullfrog (Jacobs and Hudspeth, 1990; Lenzi et al., 1999), or 40-50 nm in goldfish (Hama and Saito, 1977). A variety in the number of vesicles directly associated with the dense body has been estimated from static images of the dense body with electron microscopy and electron tomography. In frog saccular hair cells, image sections through the afferent synapse with electron tomography reveals 32 vesicles associated with the active zone underneath the dense body and 380 vesicles associated around the perimeter of each dense body (Lenzi et al., 1999 and 2002).

A number of theories as to the role that dense bodies play at the synapse have been proposed. Membrane capacitance measurements and the imaging of FM1-43 dye release during stimulated exocytosis in retinal bipolar cell terminals have given rise to the idea that the ribbon may serve as a type of scaffold (Gray and Pease, 1971) or as a conveyor belt to guide synaptic vesicles to afferent synapse sites (Bunt, 1971; Von Gersdorff et al., 1996) or as a vesicle capture site necessary for exocytosis (Zenisek et al., 2000). Early electron micrograph images of the afferent synapse in goldfish saccular hair cells led researchers to speculate that synaptic vesicles move along in rows between the dense body and the plasma membrane (Hama and Saito, 1977) similarly observed at the frog neuromuscular junction (Heuser and Reese, 1981) (Fig. 10). It is unknown what dense bodies are made of, but their electron-dense appearance in electron micrographs implies a protein-rich composition. Photoreceptor ribbons could indeed play an active role at the hair cell afferent synapse since a kinesin motor protein, KIF3A, has been detected in ribbons (Muresan et al., 1999). Another major component of ribbons and dense bodies is a splice variant of the transcription factor, C-terminal binding protein (CtBP), called ribeye (tom Dieck et al., 2005; Schmitz et al., 2000; Zenisek et al., 2003); however, it is unclear what its role is there. Additionally, it has been shown that hair cell dense body formation is dependent on the expression of Bassoon, an active zone scaffolding protein (Khimich et al., 2005).

Exocytosis at the afferent synapse:

Even though synaptic vesicles are found in close association with the dense bodies in hair cells, direct observation of exocytosis at these structures has not been made as of yet. The cluster of synaptic vesicles at the dense body is reminiscent of the vesicle clusters seen in classic electron micrograph images of the neuromuscular junction, where exocytosis is thought to occur. The presence of synaptic vesicle clusters and omega figures suggests that synaptic vesicle fusion occurs at the neuromuscular junction (Heuser and Reese, 1981). Freeze-fracture electron microscopy of the neuromuscular junction also reveals the presence of an array of transmembrane particles, suggestive of calcium channels and calcium influx (Heuser and Reese, 1981), a necessary trigger for stimulated exocytosis (Augustine et al., 1991) (Fig. 10).

In hair cells, there is substantial evidence that calcium entry at the dense body can support exocytosis. Electron tomography of frog saccular hair cells reveals omega figures near dense body sites (Lenzi et al., 1999) (Fig. 11 A, B). Presumed ion channel particles were also detected in freeze-fracture electron micrographs at the afferent synapse in bullfrog saccular hair cells (Roberts et al., 1990) (Fig. 11 C). Electrophysiological recordings of membrane patches of frog saccular hair cells also revealed clusters of VGCCs at a density similar to the density of dense bodies observed in serial EM (Roberts et al., 1990; Issa and Hudspeth, 1994) (Fig. 11 D). Similar results were observed in chick cochlear hair cells, where the mean barium current during a voltage step was related to the number and size of dense bodies (Martinez-Dunst et al., 1997) (Fig. 12). Furthermore, antibodies raised against VGCC and BK channels revealed clustering of the two channels along the basolateral chick hair cell membrane (Samaranayake et al., 2004). With Fluo-3 calcium-sensitive dye labeling of dense bodies (Issa and Hudspeth, 1994 and 1996b), direct observation of calcium influx through VGCCs with confocal microscopy was observed at these sites as an increase in fluorescence intensity during a voltage step (Issa and Hudspeth, 1996a) (Fig. 13). The estimated local concentration at dense bodies ranged from 10 μM to over 1 mM (Roberts, 1993), which is thought to be enough to support exocytosis of synaptic vesicles at ribbon sites (Heidelberger et al., 1994). In fact, only one or a few calcium channels are necessary for exocytosis (Brandt et al., 2005).

Calcium-dependent exocytosis can be measured in neurons by electrophysiological and imaging methods. Measurement of changes in membrane capacitance (ΔC_m) following a voltage step has been instrumental in elucidating some aspects of exocytosis (Neher and Marty, 1982) (Fig. 14 A – D), namely, the properties of the pool of vesicles found closest to the active zone. An estimate of this pool of vesicles using ΔC_m measurements in a ribbon-type synapse was made in the retinal bipolar terminal, where a maximum of 150 fF worth of vesicular membrane was added following a voltage stimulus for a maximum duration of 200 ms (von Gersdorff et al., 1994) (Fig. 14 E). Longer voltage steps did not produce a larger ΔC_m jump. The maximum ΔC_m jump observed was equivalent to ~6000 synaptic vesicles, assuming each vesicle is 29 aF, which matched the number of vesicles seen tethered to the ribbon in thin section reconstructions imaged with electron microscopy. The fact that the capacitance increase equals the number of vesicles physically tethered to ribbons implies that vesicles tethered to the ribbon are fusion-competent and comprise the ready-releasable pool (RRP). Furthermore, a smaller ΔC_m jump of 30 fF, or 1100 vesicles, following brief voltage steps of less than 10 ms, lends further support to the importance of the ribbon for the placement of vesicles at active zones. The smaller pool of synaptic vesicles that are positioned between the ribbon and the plasma membrane appear to be the first to undergo fusion as an ultra-fast pool of 22 synaptic vesicles per active zone (Mennerick and Matthews, 1996) (Fig. 14 F).

Estimates of the RRP size have also been carried out with ΔC_m measurements of hair cell exocytosis in frog sacculus (Parsons et al., 1994; Edmonds et al., 2004; Rutherford and Roberts, 2006), in chick THCs (Eisen et al., 2004), and in mouse IHCs (Moser and Beutner, 2000). Several studies report that the ΔC_m jumps following voltage steps are several times larger than the expected pool of vesicles found tethered to the dense body (Parsons et al., 1994; Edmonds et al, 2004) and in chick THCs (Eisen et al., 2004). It has also been suggested that synaptic vesicles fuse together to cause the large increase in ΔC_m jumps observed in hair cells (Edmonds et al., 2004). However, the stimulations used for ΔC_m measurements are much stronger than what a hair cell would normally be exposed and respond to. Perhaps long voltage steps push hair cell capabilities to an extreme where bulk endocytosis has to occur in order to replenish a largely depleted pool of vesicles. As mentioned earlier, vibrations in the form of sound or movement travel as an oscillatory waveform. In fact, it has been shown that exocytic rates are maximal when the oscillatory stimulus matches the hair cell's resonant frequency in the turtle basilar papilla (Crawford and Fettiplace, 1980). Furthermore, a recent study demonstrates that exocytosis of release-ready vesicles is apparently related to the best frequency of a given hair cell in the bullfrog sacculus (Rutherford and Roberts, 2006). Membrane voltage oscillations of +/- 5 mV around their resting membrane voltage of -60 mV evoked maximal amounts of release at 50 Hz and less release at lower or higher frequency stimulations (Fig. 15). This frequency selectivity of exocytosis was absent for large voltage stimulations of +/- 10 mV around -55 mV and probably also for voltage steps to 0 mV used in previous studies.

Post-synaptic recording of the afferent fiber has also provided some insight into hair cell exocytic behavior and is capable of detecting quantal neurotransmitter release from the hair cell afferent synapse directly (Crawford and Fettiplace, 1980; Furukawa et al., 1982; Glowatzki and Fuchs, 2002; Keen and Hudspeth, 2006). Post-synaptic recording of the afferent synapse also eliminates the contribution of any extrasynaptic neurotransmitter release assuming that a dense body exists wherever an afferent fiber contacts the hair cell and the afferent fiber is in contact with only one dense body. An interesting observation is the presence of multivesicular events in intact preparations of both the rat IHC (Glowatzki and Fuchs, 2002) and frog auditory papilla (Keen and Hudspeth, 2006) (Fig. 16). These intriguing results from postsynaptic recordings suggest that spontaneous multivesicular fusion events occur in hair cells and may even ensure the integrity of the input signal transmission to the brain.

Another method that can visualize exocytosis directly at the plasma membrane surface involves total internal reflection fluorescence (TIRF) microscopy where laser light and illumination of fluorescent particles is effectively limited to within 100 nm of the plasma membrane. Real-time images of the release of fluorescent lipophilic dye (FM1-43) during stimulated exocytosis revealed localized sites of vesicle fusion in retinal bipolar terminals using this method (Zenisek et al., 2000) that was similar in density to that of ribbons observed by EM in retinal bipolar terminals (von Gersdorff et al., 1996).

Although there is much data demonstrating that stimulated exocytosis can occur in hair cells, the question still remains whether exocytosis occurs solely at the dense body or if extra-synaptic release can occur as has been suggested in retinal bipolar cells (Zenisek et al., 2000). In electron tomography reconstructions of the area around the dense body, many ‘outlying’ docked vesicles with the PM could be seen hundreds of nanometers away from the dense body. Both associated and outlying docked vesicles were depleted in equal proportions with strong stimulation, whereas, a higher percentage of vesicles not associated with a dense body in the cytoplasm was depleted than the total percentage of dense body associated vesicles. This leaves open the possibility that outlier vesicles might undergo fusion with the PM at extrasynaptic sites without a dense body.

Vesicle replenishment:

Even though a fast RRP can undergo exocytosis within 10-20 ms in frog saccular hair cells (Edmonds et al., 2004; Rutherford and Roberts, 2006), rates of exocytosis do not slow down but, rather, stay constant for longer voltage steps up to 5 sec in the frog sacculus (Edmonds et al., 2004; Parsons et al., 1994). Synaptic depression does not seem to occur in hair cells as it does in other ribbon synapses, or it is very brief. Something about hair cell exocytosis and replenishment of new release-ready vesicles is different from retinal bipolar cells. It is unclear how vesicles were replenished and how they got there so quickly within the duration of the voltage step.

Curiously, a strong and continuous depolarization is not capable of depleting the dense body's complement of synaptic vesicles in frog saccular hair cells as imaged with electron tomography (Lenzi et al., 2002). A certain percentage of synaptic vesicles could always be found on the dense body implying that replenishment of the dense body's complement of synaptic vesicles is not a rate limiting factor. An increase in the surface area of intracellular cisterns and long infoldings of the plasma membrane in the vicinity of dense bodies was also observed in these images. This suggests that hair cells may quickly replenish synaptic vesicles by budding new ones from these intracellular organelles (Fig. 17). Electron micrograph images of hair cells reveal the presence of an extensive network of tubulo-vesicles referred to as "Canaliculi" in gerbil organ of Corti and semi-circular canals (Spicer et al., 1999; Cunningham III et al., 2000) or "anastomosing tubules" in goldfish saccular hair cells (Hama and Saito, 1977). Horseradish peroxidase uptake into coated vesicles in the IHC of cats was also observed (Leake and Snyder, 1987). These networks appear to contact mitochondria further into the cytosol and extend into the vicinity of dense bodies where budding figures, perhaps new vesicles, are present. Since hair cells seem to have a privileged ability to support high rates of exocytosis involving the fusion of thousands of vesicles for several seconds, a feat that retinal bipolar cells seem to lack (but see Lagnado et al., 1996), it would be interesting to determine how this can be done. Continuous sensory inputs of sound or movement would seem to require that the capacity for exocytosis be maintained. In addition to the various activities that take place within the hair cell during stimulus detection, descending efferent projections from the brain stem and cerebellum to auditory and vestibular hair cells add an extra level of control.

RESULTS

Calcium entry sites in hair cells:

Because dense bodies in frog saccular hair cells bind the calcium indicator Fluo-3 (Issa and Hudspeth, 1994), they fluoresce even when calcium channels are shut. Hence, calcium indicator fluorescence can be used to locate dense bodies. Fig. 18 shows a hair cell loaded with calcium indicator imaged under differential interference contrast (DIC) and under evanescent field fluorescence. Like previous authors (Roberts et al., 1990; Issa and Hudspeth, 1994 and 1996a), we concentrated on the basal half of the cell, which carries most active zones (Fig. 18 B, *white* outline). Two small fluorescent spots are readily seen in the basal portion (Fig. 18 B). Hair cells were imaged before (Fig. 19 A), during (B), and after (C) voltage pulses that opened Ca^{2+} channels. During the voltage step, the two fluorescent spots brightened dramatically (Fig. 19 B) without spreading significantly (Fig. 19 D). The result resembles those from bipolar cells, except that while Ca^{2+} channels are shut, the Ca^{2+} entry sites are more clearly visible in hair cells. The fluorescence at hot spots from eight cells showed both fast and slow kinetic components, whereas only a slow component appeared in quiet regions of the cell (example shown in Fig. 19 G, compare *green* and *red traces*). In all eight cells, all 19 Fluo-3-stained regions showed a rapid rise and fall of fluorescence as the plasma membrane was depolarized and then repolarized. The fluorescence changes outside these regions were slow and gradual. To count calcium entry sites, cells were divided into basal (Fig. 18 B, *white outline*) and apical (*gray outline*) regions. As expected for dense bodies (Roberts et al., 1990), most calcium entry sites (19 of 21) were found in the basal half of the cell. They populated the plasma membrane there at a density of 0.034 +/- 0.008 (n = 7) sites per square micrometer.

We also could generate an increase in fluorescence intensity at dense bodies when a depolarizing current step was applied to the cell (Fig. 20 B). Furthermore, both the inward current and the corresponding increase in fluorescence intensity were inhibited when external calcium was removed; however, the basal fluorescence of the dense body was unaltered (Fig. 21).

CtBP staining of hair cell dense bodies:

Ribbons contain the protein CtBP (Schmitz et al., 2000). Fig. 22 shows immunofluorescence images from a hair cell labeled with anti-CtBP. Bright punctate fluorescence is readily seen near the top or bottom surfaces. Fluorescent spots were concentrated in the basal region, with no staining found in the stereocilia (data not shown). Hair cells contained 23.9 +/- 3.0 spots (mean +/- SD), similar to the number of dense bodies estimated from electron microscopy (18.6 +/- 2.3) (Roberts et al., 1990). Similar to what has been reported for dense bodies in electron micrographs (73 %) (Roberts et al., 1990), 79.1 % of the fluorescent spots in nine cells were found within the basal half of the cell. Figure 22 *B–D* shows individual confocal sections. Spots occupy locations throughout the bottom surface (Fig. 22 B) but populate only the periphery in sections near the cell equator (Fig. 22 C and D). The staining pattern is consistent with most or all fluorescent spots located on the cell surface. We counted the number of CtBP-positive spots in the bottom-most confocal sections of the basal half of cells. Their average number was similar to that of calcium hot spots (Table 1).

Voltage gated inward current and exocytosis:

In order to further characterize the calcium currents in bullfrog saccular hair cells, whole-cell voltage-clamp or membrane capacitance recordings were made in the presence of potassium channel blockers and modulators of calcium channels. In some cases, these recordings were correspondingly imaged with TIRF microscopy and Fluo-3 dye. We initially tested whether replacement of external calcium (4 mM) with the same concentration of barium, a more permeant substrate for calcium channels than calcium, could enhance the voltage sensitive current. The voltage-sensitive current could indeed be enhanced by barium implicating voltage-sensitive calcium channels in the currents observed (Fig. 23). To see if the inward current could be blocked, we applied the non-specific calcium channel blocker cadmium at a concentration of 100 μM. Cadmium could block 88.4% of the inward current generated at -20 mV from a holding voltage of -70 mV (Fig. 24). To test whether calcium channel blockade can alter exocytosis at the afferent synapse, we measured changes in membrane capacitance in response to a depolarizing voltage step in the presence or absence of 100 μM cadmium. We observed that exocytosis could indeed be inhibited by cadmium (Fig. 24 C, D).

Spontaneous fluorescence and membrane voltage oscillation at rest:

In two unclamped cells labeled with the membrane-permeant Fluo dye AM (Fig. 25 A), we noticed that the fluorescence intensity at some labeled spots oscillated at a frequency of ~3 Hz imaged with TIRF microscopy (Fig. 25 B). We could not differentiate whether these spots reflected the opening and closing of either isolated VGCCs or of the VGCC clusters located at dense body sites. Many labeled spots did not oscillate in intensity, therefore, differentiating a dense body spot from non-specific staining of other organelles or debris on the coverslip could not be easily done. In some current clamp experiments of other cells, we sometimes observed that the membrane voltage also oscillated. The current trace of one of these cells exhibited an oscillating membrane potential around -70 mV (Fig. 25 C).

Fluo-3 fluorescence transients:

In addition to the fluorescence changes at dense bodies in response to voltage steps to 0 mV, hair cells also exhibited small discrete locations in which fluorescence fluctuated independently of the cell stimulus. Fig. 26 A–C shows an example. In a small region circled in blue (Fig. 26 A), the fluorescence transiently increased starting ~500 ms after the membrane potential had been returned to -70 mV (Fig. 26 C, *blue trace*). Similar fluorescence fluctuations were observed in eight of nine bullfrog saccular hair cells.

A fast RRP observed in hair cells:

Next, we wanted to test the exocytic capability of hair cells in response to voltage steps of various durations. We applied voltage steps from -70 to 0 mV for various durations of 5, 10, 20, 50, 100 and 500 ms and measured the jump in membrane capacitance that occurs during synaptic vesicle fusion with the plasma membrane in six bullfrog saccular hair cells. Each cell was given all six stimuli in order of increasing duration. To calculate the number of vesicles following each voltage step, we assumed that the membrane capacitance equals 1 $\mu F/cm^2$ and each synaptic vesicle would add 37 aF worth of membrane.

We observed a two-fold increase in the rate of exocytosis following short voltage step durations of 5, 10 and 20 ms relative to the rate following long voltage step durations of 50 ms or greater (Fig. 27). The average rate of exocytosis during the initial fast phase (<50 ms) was 223,874 synaptic vesicles/sec and average rate during the slow phase was 111,423 synaptic vesicles/sec (Table 2). The number of synaptic vesicles that is thought to have fused in the maximum of the fast phase (10 ms) is 2586 vesicles/cell, 114 vesicles/dense body assuming 20 dense bodies per cell. It is important to note that the external calcium concentration was relatively high (17 mM) in these experiments than the normal physiological concentration (~1-2 mM).

Spontaneous release of FM1-43 dye observed with TIRF microscopy:

To look at vesicle fusion directly, hair cells were then stimulated with 70 mM K^+ saline in the presence of FM1-43 dye to label vesicles, washed and then imaged with TIRF microscopy (frame rate = 20 Hz) to observe vesicle fusion and dye release. Fluorescently labeled vesicles were seen moving into and out of and laterally in the evanescent field. Sometimes FM1-43 dye was released in a stochastic manner (Fig. 28). Since the cells were not voltage clamped, their membrane voltage was unknown; presumably it was at rest around -70 mV, based on current clamp recordings performed in other bullfrog saccular hair cells (see Fig. 25 C). Spontaneous dye release events (n events = 7; Fig. 28 B, *red dots*) were observed in two cells and occurred at a density of $0.034/\mu m^2$ throughout the footprint. The density of spontaneous dye release events in the footprint within the basal half of the cell is 0.026/μm^2. This density is similar to the estimated density of dense bodies labeled with either CtBP immunofluorescent antibodies or Fluo-3 dye in fixed or living bullfrog saccular hair cells, respectively (Zenisek et al., 2003). An example of one fusion event is shown in Fig. 28 C (*red trace*). Visiting FM1-43 labeled vesicles that did not release dye (n events = 16; Fig. 28 B, *yellow dots*) were also observed in the footprint at a density of 0.076/μm^2. An example of one visit is shown in Fig. 28 D (*yellow trace*). No FM1-43 labeled visitors in cell shown in Fig. 28 released dye at a later time while the cell was imaged. Spontaneous dye release events occurred early after labeling (~30 min) and FM1-43 spots were not seen in image streams acquired later, perhaps because they have already undergone fusion or the image had bleached over time or both.

Possible fusion of a small, synaptic vesicle:

In one voltage-clamped bullfrog saccular hair cell labeled with FM1-43 and imaged with TIRF microscopy (as in Fig. 28), a small fusion event was observed (Fig. 29). The experiment differed in that <25 μg/ml amphotericin B was included in the recording pipette and the FM dye was washed for 65 min after loading. Amphotericin B was used to create perforations in the membrane allowing for electrical continuity but limiting dialysis of the cytosol with the internal solution within the pipette. Fig. 29 A shows the differential interference contrast (DIC) image of the hair cell with the voltage clamp recording pipette on the left. The corresponding footprint imaged in the evanescent field (Fig. 29 B, same scale as in *A*) is outlined in *blue* and has a *red* region of interest (ROI) drawn over the fusion site and a *green* ROI drawn over an adjacent part of footprint. These regions within the footprint were used to measure the fluorescence intensity over time. A rectangular ROI in Fig. 29 B (*purple*) is drawn over the glass where there is no cell. Fig. 29 C shows the current response to a voltage step from -70 to 0 mV depicted in Fig. 29 D. The current is outward because the pipette solution (containing cesium and TEA) could not diffuse into the cytosol from the pipette and block voltage-sensitive potassium channels. This suggests that the integrity of the perforated patch was maintained by the time the data presented here was acquired. (The capacitance of the cell was 18.8 pF, the series resistance was 23 MΩ, the membrane capacitance was >1 GΩ and the holding current was ~40 pA). The fluorescence intensity of the glass region was subtracted from the red and green ROIs in every frame of the image stack and the fluorescence intensity traces were normalized (Fig. 29 E).

Varied vesicle diameters at the dense body in electron micrographs:

We wanted to image the vesicles surrounding dense bodies by electron microscopy to determine what diameters they have and their position relative to dense bodies to explain the results from electrophysiological recordings and TIRF images of FM1-43 labeled cells. Afferent synapses were identified by the presence of the osmiophilic dense body and its complement of small, clear synaptic vesicles. Electron micrographs show the presence of dense bodies with diameters between 300-600 nm surrounded by synaptic vesicles ~30-50 nm in diameter as well as larger ~80-100 nm diameter vesicles (Fig. 30).

Dense bodies at presumed afferent synapses in electron micrographs:

Dense bodies were sometimes found in close proximity to each other where two were apparently in synaptic communication with one afferent fiber (Fig. 31). In other instances, one dense body was found in contact with only one afferent fiber in the same 80-100 nm slice of tissue imaged (Fig. 32).

DISCUSSION

Experiments were carried out to identify the afferent synapse and image exocytosis at these sites in living hair cells. The calcium-sensitive Fluo dye has been found to label dense body-like structures in living hair cells (Issa and Hudspeth, 1994 and 1996b). We used this finding to label dense body structures in dissociated bullfrog saccular hair cells using TIRF microscopy. Next, we wanted to determine whether these fluo dye labeled structures are indeed the dense bodies by immunolabeling fixed saccular hair cells with antibodies directed against CtBP1. This antibody also recognizes CtBP2, a splice variant of the ribbon protein ribeye. Furthermore, we wanted to test whether the fluo-dye structures co-localize with VGCC clusters that are found at the dense body (Issa and Hudspeth, 1996a) with combined TIRF imaging and voltage clamp recording. Voltage clamp and membrane capacitance recordings, without TIRF imaging, were carried out to determine whether the L-type VGCC mediates exocytosis at the afferent synapse. Finally, vesicular activity in hair cells was monitored with either membrane capacitance recordings or TIRF microscopy imaging of exocytic FM1-43 dye release.

Identification of the afferent synapse in hair cells:

It has been demonstrated that Fluo dye can label dense body structures even when the hair cell membrane voltage is at rest (Issa and Hudspeth, 1994). Identifying the afferent synapse is necessary for live cell imaging of calcium dynamics and vesicle fusion with TIRF microscopy at these sites. We demonstrate here that the dense bodies in bullfrog saccular hair cells contain the ribbon protein ribeye and that the dense bodies normally found at the afferent synapse can be accurately identified with Fluo dye in living hair cells. Furthermore, we also demonstrate that the VGCC clusters normally found at the afferent synapse (Roberts et al., 1990; Issa and Hudspeth, 1994) are co-localized with these Fluo dye labeled structures in living hair cells. The lack of a change in fluorescence intensity when the external calcium was removed indicates that the fluorescence of the dense body is not dependent on external calcium. Therefore, it could be said that CtBP2 antibody and Fluo dye can identify the dense bodies and that dense bodies are like other ribbon structures where calcium-influx and, possibly, exocytosis occur.

Voltage gated calcium channels in bullfrog saccular hair cells:

We could either enhance the inward current with barium or block the voltage-dependent inward current with cadmium. Not all of the inward current was blocked with the concentration of cadmium we used. However, cadmium could block exocytosis measured in membrane capacitance recordings indicating VGCC localization to the afferent synapse. It has been shown that a VGCC similar to the L-type calcium channel (Nowycky et al., 1985) is present in bullfrog saccular hair cells by its sensitivity to dihydropyridines. It is accepted that L-type calcium channels are primarily clustered at the afferent synapse. Other studies have found that more than one VGCC channel type may exist in bullfrog saccular hair cells, possibly an N-type-like channel (Su et al., 1995; Rodriguez-Contreras and Yamoah, 2001). However, the voltage-sensitive fluorescence intensity increases we see at the dense bodies are likely mediated primarily by the L-type VGCC, which supports exocytosis there.

Membrane voltage oscillation in bullfrog saccular hair cells:

The L-type VGCC that exists in bullfrog saccular hair cells tends to open at more hyperpolarized potentials than the L-type VGCC found in neurons. In keeping with this observation, we noticed in two cells that the fluorescence intensity at spots labeled with Fluo-4AM oscillated at a frequency similar to membrane voltage oscillations, in other cells, between -60 and -90mV in current clamp recordings. Since electrophysiological recordings were not run concurrently with these TIRF images, we cannot correlate fluorescence intensities with membrane voltage. However, since both the fluorescence intensity and the membrane voltage oscillated at a similar frequency, it is possible that they are related. However, since the membrane voltage oscillation is lower than the expected activation range of the hair cell L-type VGCC, it is possible that another voltage gated calcium channel could underlie the oscillating fluorescence intensity observed. An argument against a spontaneous low resonant frequency oscillation in these cells is that they have been treated with papain, which is known to eliminate the K_V channel thought to underlie resonant frequencies in the low frequency range. Alternatively, these oscillations might be due to spontaneous hair-bundle oscillations (Martin et al., 2003), although, the pre-treatment with EGTA during the dissociation procedure is expected to destroy the tip-links at the mechanotransducer channels there.

Fluo dye fluorescence transients imaged with TIRF:

Because fluorescence “flickers” persist even in the absence of significant calcium fluxes, they may represent calcium release from internal stores in response to a lingering elevation in calcium after VGCCs have opened. Indeed, the existence of internal calcium stores, such as the synaptic cistern, has been suggested for both cochlear (Shigemoto and Ohmori, 1991; Sridhar et al., 1997; Fuchs, 2002; Kennedy and Meech, 2002) and vestibular (Yoshida et al., 1994) hair cells. These fluorescence transients could also reflect the stochastic activities of VGCCs that operate at more hyperpolarized potentials found in bullfrog saccular hair cells (Su et al., 1995; Rodriguez-Contreras and Yamoah, 2001). The N-type VGCC is not expected to be co-localized to any great extent at the dense body sites and has been shown to be primarily located in the basolateral membrane away from the dense bodies. So, these channels may be responsible for the fluorescence transients that are not co-localized with a dense body. However, since these fluorescence transients more frequently appear after a voltage step, it seems more likely that a mechanism such as CICR is at play. Furthermore, although calcium release from mitochondria cannot be ruled out, the synaptic cisternae always located within the thin evanescent field.

Ready-releasable pool:

It was expected that a linear relationship between the membrane capacitance change and voltage step durations would be observed as seen in a previous study (Parsons et al., 1994). It was determined that exocytosis occurs at a constant rate of ~500 synaptic vesicles sec^{-1} at each of ~20 dense bodies for voltage steps to -10 mV for durations up to at least 2 sec (assuming 32 aF synaptic vesicle^{-1}, ~80 vesicles between the dense body and plasma membrane at the active zone, equivalent to the “ultra-fast pool”. In the Parsons et al. (1994) study, the number of fused vesicles in 1 sec exceeded the number of synaptic vesicles thought to be located at each active zone (~80 synaptic vesicle active zone^{-1}) by >5 times.

A linear relationship between ΔC_m jumps and voltage step duration was indeed observed here for step durations of 50 ms up to 500 ms. However, a two-fold increase in the exocytic rate was observed following step durations below 50 ms that was reminiscent of the ultrafast pool of vesicles in retinal bipolar cells (Mennerick and Matthews, 1996) (Compare Fig. 14 E with Fig. 27 A). Similar observations of a RRP of vesicles that undergoes exocytosis at a faster rate within 20-50 ms of a voltage step have been reported by several other groups in hair cells from frog sacculus (Edmonds et al., 2004; Rutherford and Roberts, 2006) and in chick THC (Eisen et al., 2004).

In a study using frog saccular hair cells (Edmonds et al., 2004), ΔC_m measurements revealed two rates of exocytosis (assuming 37 aF synaptic vesicle^{-1}, 32 vesicles between the dense body and plasma membrane at active zones and 20 dense bodies cell^{-1}). The slower rate corresponded to an exocytic rate of ~1500 vesicles sec^{-1} active zone^{-1} for up to 5 sec, a 3-fold higher rate than what was reported in Parsons et al. (1994). Furthermore, shorter voltage step durations revealed an even faster rate of exocytosis where the equivalent of 280 synaptic vesicles fused with the membrane at each active zone within a 20 ms voltage step, or ~14,000 vesicles sec^{-1} active zone^{-1}. Rutherford and Roberts (2006) also report a pool of vesicles that undergoes exocytosis at a faster rate and depletes by 10 ms. The number of vesicles that undergo exocytosis at a faster rate may be equivalent to the RRP of fusion-competent vesicles at the active zone.

The estimated RRP size exceeds the dense body's complement of vesicles in frog saccular hair cells:

For comparison, we assume that each synaptic vesicle contributes 37aF worth of membrane during exocytosis (Lenzi et al., 2002), there are 20 dense bodies per cell (Roberts et al., 1990) and 43 synaptic vesicles are found at the active zone between the dense body and the plasma membrane (Lenzi et al., 1999). In the data presented here, the number of vesicles calculated to comprise these capacitance jumps exceeds the expected number of vesicles tethered to the active zone between the dense body and the plasma membrane by 3-fold. The exocytic rate in Edmonds et al. (2004) also exceeded expectations by 7 to 9-fold, depending on whether one assumes 43 or 32 synaptic vesicles, respectively, at each active zone. However, the ΔC_m jumps in Rutherford and Roberts (2006) were smaller and closely matched the number of synaptic vesicles that are seen at the active zone beneath the dense body in electron tomography images.

In the membrane capacitance recordings presented in this thesis, the rate of exocytosis (227,000 vesicles/sec, depleted ~20 ms) is comparable with what has been reported in other studies which saw a fast rate: Edmonds et al. (2004) (282,432 vesicles/sec, depleted in 20 ms) or Rutherford and Roberts (2006) (65,586 vesicles/sec, averaged rates for 10, 25 and 30 ms). Furthermore, the calculated number of vesicles within the faster releasing pool of vesicles is about 2.6 times smaller than what was reported in Edmonds et al. (2004) and was more than double the size of what was reported in Rutherford and Roberts (2006). It is not clear why there are such big differences in the calculated RRP sizes, although one point in common was that the fastest rate is always at 10 ms: Edmonds et al. (2004) = 610,811 ves/sec, Rutherford and Roberts (2006) = 135,135 ves/sec, and in the data presented here = 227,027 ves/sec. If we assume that the RRP depletes in 10 ms for all three studies then the calculated RRP at each db is 305 (Edmonds et al., 2004), 68 (Rutherford and Roberts, 2006) and 114 (data presented here). For comparison, the ΔC_m jumps reported in this thesis and by different groups have been plotted against increasing stimulus duration for up to 100 ms (Fig. 33) or longer (Fig. 34).

It should be noted that the external calcium was higher (~17 mM) than what was used in the above mentioned studies (4 mM Parsons et al. (1994); 1.8 mM, Edmonds et al. (2004); 1.8 mM Rutherford and Roberts (2006)). The calcium microdomain was probably larger and, therefore, recruited more vesicles that underwent exocytosis at either the active zone or elsewhere with this high external concentration of calcium. An elevated amount of exocytosis is reflected in the large capacitance jumps seen at voltage step durations longer than 100 ms (Fig. 34). However, the fact that the fastest rate of exocytosis is seen at 10 ms in all three studies may indicate the lower limit of fusion readiness of vesicles close to the active zone. Furthermore, the dip in the exocytic rate starting at 25 ms in the Rutherford and Roberts (2006) study is not visible in the data presented here. One explanation for this is that those time points were not tested and the dip then might have been missed. A slowing of the exocytic rate is revealed only by 50 ms.

Physiologically relevant stimulation and the RRP:

Rutherford and Roberts (2006) suggest that physiological stimulations are oscillatory and that the frequency of a stimulus that provokes the maximum amount of exocytosis occurs at 50 Hz. Lower ΔC_m jumps were seen at low or high frequencies of stimulation (5 or 200 Hz, respectively) that caused the membrane voltage to oscillate no more than 5 mV around -60 mV. It is important that the stimulus is oscillatory; Bullfrog saccular hair cells supported higher ΔC_m jumps when a square-pulse wave of about 50 Hz (20 ms peak to peak, from -80 to -50 mV) was applied than when a sustained 30 ms pulse was applied. Therefore, stimuli that simply depolarize the membrane potential to the peak calcium current (-10 to 0 mV) used in previous studies to characterize the RRP in hair cells may have been too strong and missed an important aspect of hair cell physiology. Nevertheless, the RRP in hair cells (defined by the elevated rate of exocytosis at shorter voltage step stimulations) is depleted much more quickly (~30 ms) than in retinal bipolar cells where the RRP is depleted by 200 ms. Furthermore, hair cells seem capable of recruiting vesicles for exocytosis at a faster rate than retinal bipolar cells when the calcium concentration in the bath is elevated beyond the physiological level.

Spontaneous vesicle fusion in bullfrog saccular hair cells:

It is unclear whether these fusion events are related to stimulated exocytosis previously observed with membrane capacitance recordings since they apparently occur in a non-stimulated manner. However, since membrane voltage oscillations have been observed in these cells as well as oscillatory fluorescence intensity of Fluo dye, it is possible that the spontaneous dye release events are supported by an oscillatory opening and closing of VGCCs. This could be further supported by the findings in Rutherford and Roberts (2006) where ΔC_m jumps could be seen even when a "weak" oscillatory stimulus of +/- 5 mV around -60 mV at a frequency of 5 Hz was applied.

The similarity of the density of dye release events with the expected density of dense bodies in these hair cells indicates that the observed dye release events may reflect vesicle fusion at dense body sites. If the visitor and dye release events are pooled, then the density is becomes 0.11/ μm^2, three times higher than the expected dense body density. The decrease in dye release events could be because the pool of vesicles that have been labeled during the initial high potassium stimulation in the presence of FM1-43 dye has been depleted. Unlabeled vesicles may undergo exocytosis without detection.

Endosome size and multi-vesicular release:

Since electron micrographs reveal vesicles of various diameters and because the number of FM1-43 dye molecules in each fusion event was not measured, we cannot be sure what size the vesicles were that released dye. However, it is possible that the spontaneous release events were due to the release of large organelles thought to form following strong stimulations in retinal bipolar cells (Paillart et al., 2003). These large endosomes are thought to form by a homeostatic mechanism whereby a large amount of membrane undergoes endocytosis to compensate for the large amount of exocytosis that occurs with strong stimulation. These large endosomes are also thought to undergo exocytosis soon after a strong stimulation which could explain the FM1-43 dye release events here. Large infoldings of membrane were also observed in electron tomography images following strong stimulation as well (Lenzi et al., 2002). Perhaps, the FM1-43 dye release events observed with TIRF microscopy here were of these large endosomes.

There is, however, a growing body of evidence that suggests that multi-vesicular release or compound fusion occurs in hair cells of the frog sacculus (Edmonds et al., 2004), of the frog basilar papilla (Keen and Hudspeth, 2006), and in rat IHC (Glowatzki and Fuchs, 2000). Edmonds et al. (2004) speculates that the compound fusion of vesicles before they fuse with the plasma membrane can account for the large jump in ΔC_m that is beyond the capacity of vesicles tethered to the dense bodies. Glowatzki and Fuchs (2000) and Keen and Hudspeth (2006) both record quantal neurotransmitter release from the hair cell onto the afferent fiber where a certain number of exocytic events generate larger than expected (excitatory post-synaptic potential) EPSCs or generate events that undergo fusion in a highly synchronized manner. If the multivesicular events are indeed highly synchronized at one dense body, or two as has been observed in electron micrograph images here, then perhaps the FM1-43 release events seen with TIRF microscopy are of vesicles that had fused together beforehand generating a large fusion event, or, are the result of dye release from more than one vesicle at the same time.

CHAPTER III: The efferent synapse

INTRODUCTION

Efferent synapse activity:

In addition to relaying mechanosensory information to the brain, a population of hair cells in each sensory organ of the inner ear also receives a modulatory input from the brain stem or cerebellum as well. Efferent input is primarily cholinergic as evidenced by histochemical detection of acetylcholinesterase activity in the goldfish saccule (Sugihara, 2001), or of cholineacetyltransferase (ChAT) activity in chick (Zidanic, 2002) (Fig. 35). Recordings of spontaneous neurotransmitter release onto IHCs of the rat organ of Corti demonstrate that the efferent neurotransmitter is acetylcholine (Glowatzki and Fuchs, 2000). Cholinergic neurotransmitter release from efferents has also been shown in the goldfish sacculus (Furukawa, 1981). Although their role is less obvious, other neurotransmitters, such as γ-aminobutyric acid (GABA) in guinea pig IHC (Felix and Ehrenberger, 1992), adenosine triphosphate (ATP) in OHC of guinea pig (Ashmore and Ohmori, 1990), and calcitonin gene-related peptide (CGRP), have a presence in efferent innervation as well; the focus here will be on the dominant cholinergic activity.

In hair cells, cholinergic efferent input is primarily inhibitory. Efferent stimulation induces a membrane hyperpolarization and diminished tuning ability of hair cells in the turtle basilar papilla (Art et al., 1985) (Fig. 36) and in the frog sacculus (Ashmore, 1983). Membrane hyperpolarization and an increase in a calcium-sensitive potassium conductance in response to cholinergic agonists have been reported in the chick basilar papilla (Fuchs and Murrow, 1992a, b) and in the frog sacculus (Sugai et al., 1992; Yoshida et al., 1994). Although cholinergic efferent stimulation is usually reported as inhibitory, there are also reports in the literature that it can induce a facilitation of afferent activity in the frog sacculus (Guth et al., 1994) and semi-circular canals (Rossi et al., 1988; Valli et al., 1986).

Cholinergic efferent effects on sensory detection:

There are a number of ways in which efferent stimulation may influence auditory and vestibular function. Some ideas are that olivocochlear stimulation can impart protection from hair cell damage due to acoustic overexposure in the OHCs of the cat (Rajan, 2001) and guinea pig (Reiter and Liberman, 1995). It has also been suggested that efferent stimulation increases the gain of sensory organs (Goldberg and Fernandez, 1980). Furthermore, there is evidence that efferent input can improve hearing by increasing the signal to noise ratio of sounds of interest over background sounds (Tomchik and Lu, 2006; Guinan and Stankovic, 1996).

Ionic activity at the cholinergic efferent synapse:

Unlike classical studies of muscle and neurons in the brain, where cholinergic innervation induces an excitatory response, the cholinergic efferent synapse in hair cells induces an inhibition by membrane hyperpolarization. Membrane hyperpolarization is achieved by the combined activity of nicotinic acetylcholine receptor channels (nAChRs) and small-conductance calcium-sensitive potassium (SK) channels located on the postsynaptic hair cell membrane (Fuchs and Murrow, 1992b;

Martin and Fuchs, 1992) (Fig. 37, *left*). Activation of nAChRs initially results in a brief depolarization by mixed sodium and calcium influx, which is rapidly overshadowed by a hyperpolarizing potassium efflux through SK channels (Fig. 37, *right*). In addition to nAChR and SK channels, a flat organelle called the synaptic cistern is frequently seen at the efferent synapse and may be involved with calcium handling there (Fig. 37, *left*).

Nicotinic ACh receptors:

The hair cell nAChRs are ligand-gated channels that are permeable to both sodium and calcium. The nAChR expressed in most hair cells is the α9/α10 nAChR subtype of $(\alpha 9)_2(\alpha 10)_3$ stoichiometry (Plazas et al., 2005) with unique properties compared with the nAChR type expressed in the brain (Elgoyhen et al., 1994 and 2001). Mature IHCs lose both the efferent input and the α10 nAChRs, however, leaving behind the α9 subunit (Elgoyhen et al., 2001). The α9/α10 nAChR has unusual pharmacology in that it does not bind to nicotine, but is reversibly blocked by α-BTX (Elgoyhen et al., 1994) and strychnine (a glycine receptor antagonist) and is activated by muscarinic pharmacological agents (Verbitsky et al., 2000). The α9/α10 receptor has pharmacological similarity to $GABA_A$, glycine and type 3 serotonin receptors (Rothlin et al., 1999).

There are reports of a GTP-binding regulatory protein (G-protein) mediated hyperpolarization through mAChRs in the toadfish saccule (Steinacker and Rojas, 1988) and chick cochlea (Shigemoto and Ohmori, 1991) where bath applied cholinergic agonists increased the potassium conductance recorded within a cell-attached patch of membrane. Also, muscarinic agonists and ATP increased cytosolic calcium concentration and ATP induced a membrane hyperpolarization (Shigemoto and Ohmori, 1990). However, the α9/α10 nAChRs in hair cells can respond to typical muscarinic agonists (Verbitsky et al., 2000). It is possible that these results could be alternatively explained by the unique features of the hair cell efferent synapse, namely, the presence of α9/α10 nAChRs and of the diffusion of calcium released from stores thought to result from their activation.

SK channels:

Apamin, an SK channel antagonist, selectively blocks the outward current in response to depolarizing steps in frog sacculus (Chabbert, 1997) or to acetylcholine application in frog sacculus (Yoshida et al., 1994) and in frog crista (Ohtani et al., 1994). Apamin also blocks the outward current generated by cholinergic neurotransmission from efferent fibers in rat cochlea (Glowatzki and Fuchs, 2000) and in frog sacculus (Holt et al., 2001). In turtle basilar papilla hair cells, apamin also blocks the SK channel tail current (Tucker and Fettiplace, 1996).

In frog saccular hair cells, SK and nAChRs are thought to be in close proximity to each other because of the rapidity of SK channel activation in response to ACh (Fuchs and Murrow, 1992b) and because of the high concentration of BAPTA that is required to eliminate the SK response. Because of the rapid onset of SK currents following nAChR activation even in the presence of BAPTA, it is thought that SK channels were activated only by the calcium that enters through nAChRs. Although calcium influx through nAChRs may be sufficient to activate SK channels, there is growing evidence that a subsurface organelle found in hair cells can augment or may even be required for cholinergic activation of SK channels at the efferent synapse.

Synaptic cisternae at the efferent synapse:

In addition to nAChRs and SK channels, an organelle resembling smooth endoplasmic reticulum (sER), called the synaptic cistern, can also be seen lying flat within ~100 nm against the postsynaptic membrane opposite presumed efferent terminals filled with small, clear vesicles in electron micrographs of OHCs (Ross, 1997; Sridhar et al., 1997) and in chick SHCs (Tanaka and Smith, 1978) (Fig. 38). The distance from the plasma membrane can be ~8-40nm in OHCs (Sridhar et al., 1997). It is thought that the synaptic cistern may serve as a calcium source that can amplify the calcium influx signal through the nAChRs by calcium-induced calcium-release (CICR) (Fig. 39). This mechanism has been described in bullfrog saccular hair cells (Yoshida et al., 1994), IHCs of guinea pig (Yamashita et al., 1993), frog crista (Ohtani et al., 1994) and in cochlear OHCs resulting in changes in cell morphology (Dallos et al., 1993; Dallos, 2006; Sridhar et al., 1997). Activation of SK channels by CICR has also been shown in mammalian inner hair cells following voltage depolarization (Kennedy and Meech, 2002) possibly by secondary diffusion of calcium entering through VGCCs.

There is precedence for the presence of CICR at the efferent hair cell synapse since CICR has been observed in many other cell types including dorsal root ganglion cells (Mathers and Barker, 1981), cardiac (Fabiato, 1983; Cheng et al., 1993), skeletal (Tsugorka et al., 1995), and smooth muscle (Nelson et al., 1995), adrenal chromaffin cells (Montero et al., 2000), oocytes (Berridge, 1988), as well as various types of neurons. CICR has been implicated as a modulator of a variety of cellular activities such as muscle contraction, calcium wave generation, exocytosis and synaptic plasticity (Tsien and Tsien, 1990; Berridge, 1998; Rose and Konnerth, 2001, reviews).

It has been shown in bullfrog saccular hair cells (Yoshida et al., 1994) and guinea pig OHCs (Blanchet et al., 1996) that acetylcholine (ACh) can, indeed, induce an increase in calcium concentration in the basal portion of the hair cell where efferent contact is presumably made. The increase in calcium concentration was suspected to originate from the synaptic cisternae. Calcium release from the cisternae could be mediated by calcium binding to ryanodine receptors (RyR) and possibly also to inositol triphosphate receptors (IP_3R) followed by release through these channels.

It is curious that the synaptic cisternae are so closely associated with efferent terminals of cochlear and vestibular hair cells. It is possible that the tight space between the cisternae and the plasma membrane can serve to physically limit calcium diffusion away from entry sites as through the nAChRs in order to ensure SK channel activation. Structural similarity of synaptic cisternae to sER and possession of the sarcoplasmic endoplasmic reticulum calcium ATPase (SERCA) ion exchanger (Kennedy, 2002) implies that it could also serve as a calcium sink by active removal of cytosolic calcium by the production of ATP. However, it still is not known how significant or necessary calcium release from the synaptic cisternae is to SK channel activity or general efferent synapse function since calcium release in response to cholinergic stimulation has not been directly observed.

RESULTS

ACh-induced current is inward in bullfrog saccular hair cells:

Isolated bullfrog saccular hair cells were whole-cell voltage-clamped while an ionophoretic pipette was placed within ~1 μm from the cell surface (Fig. 40 A). Ionophoresis of 1M ACh (in deionized water) induced an inward current at -60 mV in 6 out of 14 of cells tested with stable electrophysiological recordings. An example of one of these current responses to ionophoretic application of ACh (500 ms duration) is shown in Fig. 40 B. The *black bar* above the current trace in Fig. 40 B indicates the timing of the pulse. The amplitude, onset and offset of the current response are the same if a 50 or 500 ms ionophoretic pulse of ACh was applied (not shown). In some cells which responded to ionophoretic application of ACh, the response could be repeated multiple times (not shown). In another bullfrog saccular hair cell, an inward current with a similar amplitude and similar kinetics to the ionophoresis of ACh (Fig. 40 B) was generated by microperfusion of 100 μM ACh (in bath) through a ~1 μm tip pipette for 600 ms (Fig. 40 C). The *grey bar* above the trace in *B* indicates the timing of the ACh puff for the trace in *C*.

Electron micrograph images of synaptic cisternae in bullfrog saccular hair cells:

We wanted to see whether bullfrog saccular hair cells indeed have synaptic cisternae and where they are located. We used electron microscopy to image intact, fixed slices of the sacculus (Fig. 41). We looked for sites where vesicle-filled terminals contacted hair cells on the basolateral surface to see if there was a corresponding organelle like the synaptic cistern beneath the plasma membrane. We noticed structures that had a flat, electron-dense rough ER-like appearance located directly opposite some vesicle-filled terminals beneath the plasma membrane at presumed efferent synapses (Fig. 41 A – D). However, there was no obvious membranous cistern associated with these electron-dense structures, except in one of these images (Fig. 41 D). Another electron micrograph of the base of a bullfrog saccular hair cell also showed multiple small-clear vesicle-filled termini at the base of the hair cell with no obvious synaptic cistern counterpart (Fig. 42). It is unknown what neurotransmitter the vesicles in each terminal contain.

ACh-induced currents in chicken cochlear hair cells:

We tested ACh-induced SK channel activation in chicken cochlear SHCs from embryos (e19-21) and chicks (p0-10) by microperfusion of 100 μM ACh in bath saline for 90 ms and recording in either voltage clamp or current clamp mode. ACh induced either an outward current in 37 out of 42 cells or an inward current in 5 out of 42 cells at a holding potential of -40 mV. ACh induced a membrane hyperpolarization in current clamp recordings of cells that responded to ACh in voltage clamp whenever tested (not shown). Figure 43 illustrates an example of a typical voltage-sensitive response to ACh in one cell filled with 11 mM EGTA through the recording pipette. Traces on the left are the responses to various test voltages and traces on the right are the responses following each trace shown on the left at the control holding potential of -40 mV. The black traces on the left and right are the first two responses to ACh in this figure at a holding potential of -40 mV. The reversal potential of the ACh-induced current was close to the expected reversal potential for potassium. The polarity reversal of the current is also demonstrated when current responses to ACh microperfusion were pooled from a total of 43 chick hair cells (Fig. 44). The cells included in Fig. 44 were micro-perfused with 100 μM ACh for 90 ms while the membrane potential was held at both a test and the control membrane potential of -40 mV. Different cells were dialysed with one of three calcium buffers: 11 mM EGTA (orange circles), 1 mM BAPTA (blue triangles) or 10 mM BAPTA (green squares) BAPTA. It can be seen that the reversal potential of the ACh response shifted closer to the reversal potential for calcium when 1 or 10 mM BAPTA was used as an intracellular buffer as opposed to when EGTA was used. Data values for cells dialysed with 11 mM EGTA at the indicated voltages are: Current responses to ACh were calculated using a modified IGOR macro kindly supplied by Dr. Felix Felmy. Briefly, the macro first smoothes the traces by applying a rolling average of every three points and repeats this rolling average two more times. The average current is calculated for a range of 7000 data points before the ACh puff and this value is then subtracted from the peak current (highest point for positive-going currents or lowest point for negative-going currents) for a user-specified range of time following the start of the ACh puff. Only one measurement per cell was used per voltage step per calcium buffer. Some cells may have contributed more than one current measurement if each response was to a different voltage. Although, some cells may have been brought to the same voltage more than once, only the first response to a particular voltage was included in the data set.

The ACh-induced response was also sensitive to a blocker of nAChRs (300 nM α-BTX) and to a blocker of SK channels (10 μM apamin). The traces shown in Fig. 45 A and B are six applications of ACh in the same cell in sequential order with varied amounts of time in between where additional puffs of ACh were applied not shown. The membrane voltage was held at -40 mV throughout these recordings. The sensitivity to α-BTX is shown in Fig. 45 A where the blue trace shows the ACh response in the presence of the drug. Note that the concentration of α-BTX used was not enough to completely block the outward current response. Washout of α-BTX and recovery of the response to ACh is shown in the grey trace in Fig. 45 A. The sensitivity of the response to ACh was tested with 10 μM apamin and is shown in Fig. 45 B. The orange trace shows that the ACh response was completely blocked by apamin. Complete washout of apamin could not be achieved; however, a small amount of the inward calcium current through nAChRs and outward potassium current through SK channels is visible in the magnified "recovery" trace (grey) in the inset.

ACh-dependent fluorescence transients in chicken cochlear hair cells:

ACh (100 μM in bath saline) was puffed through a micropipette (3-5 psi) for 90 ms onto short hair cells that appeared to be well-adhered to the glass. We tried to pick cells that were oriented such that the hair bundle was more or less pointing up perpendicular to the plane of the glass. The hope was that a large enough surface area would adhere to the glass and any fluorescence changes at the efferent synapse could be monitored within the evanescent field of laser light. One observation, which in the end may have served as a positive control for ACh perfusion, was that ACh was mildly auto-fluorescent and could be detected during the puff with the camera. Separate measurement of the ACh solution in a fluorimeter, however, did not reveal any autofluorescence (not shown). It is unclear what caused this autofluorescence during the ACh puff.

A localized increase in fluorescence intensity was observed in 1 out of 27 cells (filled with 11 mM EGTA) and 0 out of 10 cells (filled with BAPTA) that exhibited an ACh-dependent current change and were imaged with TIRF microscopy (Fig. 46). The localized fluorescence intensity increase in this one cell was much greater than the fluorescence intensity of the ACh puff itself. Fig. 46 A shows the DIC image of the cell that was contacted by the whole-cell voltage clamp pipette on the right. The perfusion pipette containing ACh is pointing towards the cell from the left (not shown). Fig. 46 B shows the footprint of the cell in *A* (same magnification) and two circular ROIs (10 pixel diameter) drawn over either the ACh responding site (ROI 1, *blue*) or a non-responding site (ROI 2, *grey*). A rectangular 30 x 40 pixel ROI (Fig. 46 B, *white*) was drawn over the glass where there was no cell and was in the path of ACh perfusion. Current responses to ACh at three different membrane voltages by the same cell shown in *A* and *B* are presented in Fig. 46 C. The voltage sensitivity of the current responses to ACh is similar to that shown previously in Figs. 43 and 44. Despite a voltage-sensitivity of the current response to ACh, the local increase in fluorescence intensity upon exposure to ACh was unaffected by membrane voltage (Fig. 46 D). The ACh-dependent increase in fluorescence intensity when the membrane potential was held at -60 mV, however, exhibited an obvious double-peak that was not seen in the corresponding current trace (Fig. 46 D, right-most *blue trace*). Note that the onset of the ACh-dependent increase in fluorescence intensity at ROI 1 increases slightly with each application of ACh relative to the onset of the ACh puff (Fig. 46, compare *blue trace* with *dotted grey lines*). This delay in the response is likely due to a slight, but additive, delay imposed by the image acquisition software. No attempt to align the onset of the current and the F/F_0 response to ACh was made. The fluorescence intensity at ROI 2 exhibited no change with the ACh puff. Fluorescence intensity data values at ROI 1 and 2 were first subtracted by the fluorescence intensity within the rectangular glass ROI in each frame and then normalized to the average fluorescence before each ACh puff while the membrane potential was held at a given test voltage.

Whole-footprint fluorescence intensity during ACh perfusion:

Because an obvious and localized ACh-dependent increase in fluorescence intensity was so infrequently observed, we looked to see whether small changes in fluorescence intensity in response to ACh may have gone undetected. The fluorescence intensity of the whole footprint of 17 hair cells (filled with either 11 mM EGTA or no added buffer other than Fluo dye) that exhibited a positive-going current response to ACh at -40 mV was measured in an image stack. The region was drawn along the perimeter of the footprint as shown in an example in Fig. 47 B. To cancel out background mechanical changes in the fluorescence intensity, the fluorescence intensity within a rectangular 30 x 40 pixel ROI (Fig. 47 B, *white rectangle*) was subtracted from the footprint region in each frame of the image stack. Note that this rectangular glass region was placed close to the mouth of the perfusion pipette where there was no cell in the path of ACh perfusion. Since ACh seems to exhibit a consistent, but unexplainable, autofluorescence, subtraction of the glass fluorescence from the footprint fluorescence will result in a negative value if the footprint response to ACh is very small.

We looked at 16 cells that were all dialysed with 11 mM EGTA through the recording pipette and that were also included in the data set for Fig. 44. An example of a typical cell where the electrophysiological response to ACh is positive-going, but the fluorescence intensity response to ACh following subtraction is negative is shown in Fig. 47 C – E. Fig. 47 C shows the current response to ACh and Fig. 47 D shows the raw fluorescence intensity values for both the footprint region (*blue, top trace*) and the glass region (*grey, bottom trace*). Fig. 47 E shows the resultant glass-subtracted footprint F/F_0 values normalized to the average intensity before the ACh puff. Compare the decrease in the F/F_0 values with the traces above in *C* and *D*. Dotted grey lines indicate the duration of the 90 ms ACh puff. Some cells that were not dialysed with calcium buffer other than Fluo dye also did not exhibit any small increases in fluorescence intensity following the same analysis method described above (not shown).

The one cell that did exhibit a change in fluorescence intensity with ACh (Fig. 46) had a different F/F_0 profile (Fig. 48). Again, the current response to ACh is shown in *B*, and the raw fluorescence intensity values for the footprint (*blue*) and glass (*grey*) regions are shown in *C*. Note that a small decrease in F/F_0 is visible between the grey dotted lines that indicate when ACh was perfused. The decrease between the grey lines is likely due to subtraction of the ACh solution in the glass region before the cell was exposed by it and had a chance to respond by then. The larger decrease before the ACh puff may be due to a magnifcation of the footprint intensity values following glass intensity subtraction (compare *blue* and *grey* traces in *C*). The increase in footprint F/F_0 after the ACh puff illustrates the increase in footprint fluorescence intensity above the autofluorescence of the ACh perfusion solution. However, the amplitude of the footprint F/F_0 response to ACh is smaller than that previously shown in Figure 46 D. The diminished amplitude of the footprint F/F_0 response presented in Fig. 58 D is because much of the footprint that exhibited no response to ACh was averaged along with the small region which did.

DISCUSSION

The goal of these experiments was to test whether the synaptic cistern, a presumed calcium store, activates SK channels in response to nAChR activation by CICR at the efferent synapse. While recording with whole-cell voltage or current clamp, either ionophoresis or microperfusion was used to locally apply ACh, one of the primary neurotransmitters acting at the efferent synapse. Acutely isolated bullfrog saccular or chick cochlear hair cells were used for these experiments. Calcium fluxes at the membrane were measured directly with TIRF microscopy, a method of illumination that effectively limits laser light to within 100 nm of the plasma membrane. This method could allow one to image the opening and closing of calcium-permeable channels at the plasma membrane as well as from synaptic cisternae, the width of which could almost fit entirely within the evanescent field.

Acetylcholine-induced current in bullfrog saccular hair cells:

In only a small population of bullfrog saccular hair cells tested with stable recordings did we see a response to ACh exposure either by ionophoresis or microperfusion (Fig. 40 B and C, respectively). Furthermore, the response was always an inward current, never an outward one as would be expected for SK channel activity. Although there were some measurable responses to ACh, there were many cells where ACh was applied with no response. One problem was that the stability of the recording deteriorated at voltages above resting when there was no cesium or TEA in the pipette. A high baseline current at depolarized membrane potentials was frequently observed (not shown). This posed a problem for testing whether the response we saw to ACh was voltage-sensitive. This may be because these cells express a large number of other voltage-sensitive potassium channels that likely contribute to a large outward current above -50 mV (Chabbert, 1997; Guth et al., 1998). Unfortunately, cesium could not be included in the pipette because it could potentially affect the CICR response (Kennedy and Meech, 2002).

It is also possible that the SK channels, and perhaps some nAChRs, may have been damaged during cell isolation leaving behind the inward current through the nAChR in a small population of cells. In fact, many cells tested without responses were dissociated with papain, a known destroyer of ion channels, particularly of potassium channels (Armstrong and Roberts, 1998). Trypsin was also tried since it was better than papain for preserving the nAChR currents in frog vestibular hair cells (Holt et al., 2001). Unfortunately, trypsin did not seem to work in our hands. The above responses, however, were from cells that were dissociated with EGTA and subtilisin (see Materials and Methods).

Another explanation for the lack of an outward current, even at -40mV is that the hair cells that were frequently chosen for recording might have lacked an apamin-sensitive current described for bullfrog saccular hair cells (Chabbert, 1997) (Fig. 49). Central flask-shaped hair cells (CFHC) possess an apamin-sensitive current, whereas central cylindrical hair cells (CCHC) lack it (Fig. 49, *below*, B and D). Even so, it is important to point out that an ACh-mediated inward current could have a similar inhibitory effect on hair cell activity as SK channel current activation. Membrane depolarization following calcium influx through nAChRs would, in turn, diminish the driving force for calcium influx through transduction channels located in the hair bundle effectively limiting the signal arising from bundle movement. Therefore, the inward current in response to ACh and apparent lack of an outward current may reflect a mechanism for dampening hair cell activity without SK channel activation at the cholinergic efferent synapse in bullfrog saccular hair cells.

Synaptic cisternae at efferent synapses in bullfrog saccular hair cells:

It is not clear whether bullfrog saccular hair cells possess synaptic cisternae or not. In images with TIRF microscopy and Fluo dye, changes in fluorescence intensity were never seen, even in the one cell where an ACh-sensitive inward current was observed. The presumed synaptic cisternae in electron micrographs have a different appearance than the smooth ER appearance that was expected from electron micrographs of other hair cell types (Ross, 1997, Sridhar, 1997). There were also a number of presumed efferent terminals that did not have an obvious synaptic cistern counterpart in the hair cell (Figs. 41 C, *asterisk* and 42). This suggests that, in bullfrog saccular hair cells, not all efferent synapses have cisternae. If there are only a small number of cholinergic efferent synapses and cisterns are only found at cholinergic synapses, it may explain the lack of an ACh-sensitive fluorescence intensity change in the membrane imaged within the TIRF field. Perhaps the efferent terminals seen in electron micrograph images were not even cholinergic, but rather contained other neurotransmitters such as GABA, ATP, or CGRP, which have also been implicated at the efferent synapse. Therefore, since the cell types chosen for recordings may have lacked an apamin-sensitive current, ion channels at the efferent synapse may have suffered mechanical damage from dissociation, or not all synapses were cholinergic, detection of an ACh response was essentially hit or miss.

Acetylcholine-dependent ionic activities in chicken cochlear hair cells:

Since typical efferent activities could not be measured reliably in bullfrog saccular hair cells, we decided to repeat the same experiments using SHCs isolated from the chick cochlea. The benefit of using chick SHCs is that they possess a large synaptic cistern that directly opposes a calyx-like efferent terminal at the base (Fig. 38). Furthermore, the ACh response in SHCs is large since they primarily receive an efferent input with little or no afferent contact (Hirokawa, 1978; Fischer, 1992; Martinez-Dunst et al., 1997) (Fig. 3 B and Fig. 12 A).

A number of observations indicate that SK channel activity at the cholinergic synapse was observed in our chick hair cell preparation: 1) ACh induced a membrane hyperpolarization at resting membrane voltage (not shown), 2) the ACh-induced current response reversed at the expected reversal potential for potassium when EGTA, a calcium buffer with slow binding kinetics, was used in the recording pipette (Fig. 43 and 44), 3) BAPTA, a calcium buffer with fast binding kinetics, shifted the ACh response closer to the reversal potential for calcium (Fig. 44), and 4) the response to ACh was sensitive to both α-BTX and apamin (Fig. 45). These observations indicate that ACh-dependent SK channel currents can be reliably induced in our preparation of hair cells from the chicken cochlea and further studies of ACh-sensitive CICR from the synaptic cisternae are possible.

TIRF microscopy of a response to ACh in chicken cochlear hair cells:

Since typical SK channel activity could be generated with acetylcholine in chicken cochlear hair cells, we wanted to demonstrate whether or not the synaptic cistern participates in the activation of the ACh-dependent current response. We combined electrophysiological recording with TIRF microscopy to directly monitor acetylcholine-dependent calcium flux at the membrane in chick SHCs. The large calyx-type efferent terminal in the chick SHCs can allow one to image calcium fluxes at the efferent synapse where no other obvious marker for it exists in bullfrog saccular hair cells. In one chick SHCl, an increase in Fluo dye fluorescence intensity was detected upon ACh exposure. It is unknown whether this fluorescence intensity increase reflected calcium influx through the nAChR presumably located there or calcium release from the synaptic cistern due to CICR or both. It was also surprising that the fluorescence response was so defined (~37 pixels, 104 nm^2 pixel^{-1}) and only one of these responsive regions was seen in a footprint area of 3033 pixels, 104 nm^2 pixel^{-1} (Fig. 46 B). If the base of SHCs are contacted by a calyx-type efferent terminal and the synaptic cisternae is found along the entire length of the terminal, one might expect that nAChRs would be located throughout this region too. If this response indeed reflected, at least in part, calcium influx through open nAChRs, it is surprising that they are clustered into a small space ~1 % the size of the footprint.

When ACh was reapplied to the same cell in current clamp mode, the membrane voltage hyperpolarized as expected for a cholinergic induction of SK channels (not shown), however, by this time, the general fluorescence increased by three-fold and the localized increase in fluorescence was lost. The unexpected outcome was that the

$\Delta F/F_0$ for all regions measured within the footprint *increased* in fluorescence when the membrane voltage was *hyperpolarized* from -30 to -60 mV. Why was there an increase in fluorescence at hyperpolarized membrane potentials? This will be further discussed in Chapter IV.

INTRODUCTION

Calcium noise and non-voltage-gated calcium flux:

Calcium plays significant roles at the afferent synapse as a trigger for exocytosis and modulator of BK channel activity and at the efferent synapse in mechanisms that may serve as negative feedback to limit neurotransmitter release at the dense body. Observations of calcium revealed with TIRF microscopy may reflect further aspects of calcium handling at the hair cell plasma membrane. One observation includes a transient activity here described as calcium noise. The appearance of calcium noise resembles a process described in other cells called "sparking" that is generated by CICR described in Chapter III. Another observation with TIRF microscopy was the development of a more sustained activity over time that resembled a non-voltage-gated calcium flux. There are at least two possible explanations for the observation of a non-voltage-gated calcium flux at the plasma membrane. One possibility is that hair cells may possess calcium-release activated calcium (CRAC) channels that, in other cells, are thought to provide a fast and direct pathway to refill emptying calcium stores with extracellular calcium. This mechanism is referred to as capacitative calcium entry (CCE) or store operated calcium entry (SOCE) (Putney, 1986). Another possible mechanism that also involves external calcium entry may involve a voltage-mediated reversal of the sodium-calcium exchanger (NCX) found in the guinea pig OHC plasma membrane (Ikeda et al., 1992), but not in neonatal mouse IHCs (Kennedy, 2002). The development of the CRAC current and SOCE as well as NCX activity will be described using examples from other cell types where these activities have been characterized.

CRAC channel and SOCE:

The CRAC channel has been the subject of much research for the last 20 years since they were first described in parotid acinar cells (Putney, 1986). CRAC currents have since been identified in a variety of cell types and are thought to mediate SOCE across the plasma membrane to refill calcium store organelles. For example, CRAC channel activity is necessary for the immunological response in T lymphocytes (Feske et al., 2001; Lewis, 2001). The CRAC channel has not been cloned and there are no known pharmacological agents for it, however, there are some criteria that have been used to demonstrate a current mediated by CRAC, albeit not exclusively from other channels, such as TRPV5 and 6. These criteria are: 1) the current amplitude goes to zero pA as the voltage approaches the reversal potential for calcium and, 2) the current shows a prominent inward rectification at hyperpolarized potentials in part due to calcium-dependent inactivation of the CRAC current that is diminished when the external calcium is replaced with sodium.

There is, however, recent evidence on the identity of the SOC channel and a proposed mechanism for the generation of SOCE in Jurkat T cells (Luik et al., 2006) based on the identification of the putative calcium sensor on the ER (Stim) (Roos et al., 2005) and of an essential pore subunit of the CRAC channel (Orai1) (Prakiya et al., 2006). The model proposes that Stim senses depletion in luminal ER calcium concentration, forms clusters and then initiates the movement of the ER toward the plasma membrane where Orai1, the presumed pore subunit of the CRAC channel, is located. Orai1 likewise forms clusters in the plasma membrane opposite Stim and Stim and

Orai1 molecules are thought to then form the SOC channel through which extracellular calcium can enter efficiently into the ER.

Even though CRAC channel activity has not yet been described in hair cells, it is conceivable that hair cells could utilize CRAC channels, especially since the architecture of the efferent synapse almost always includes the synaptic cistern, a presumed calcium store organelle. CRAC channels could be part of a refilling mechanism for a depleting calcium supply in the synaptic cistern.

Calcium export:

Hair cells are dependent on intracellular calcium to carry out various activities that take place within a small distance of each other. Increases in calcium concentration and diffusion from points of entry must be tightly regulated to avoid complications due to its excess. Intracellular calcium buffers, calcium uptake into store organelles and calcium export across the plasma membrane are all methods in which the maintenance of intracellular calcium concentration in hair cells is achieved (Tucker, Art and Fettiplace, 1996).

The observations presented in this chapter are thought to be related to a calcium flux at the plasma membrane that is not due to VGCC activation. There are at least two methods used by many types of cells to export calcium across the plasma membrane; one is the NCX and the second is an ATP-driven calcium pump (PMCA) (DiPolo and Beauge, 2006; Guerini et al., 2005, reviews). In outer hair cells, there is evidence for calcium export by NCX (Ikeda et al., 1992) as well as by PMCA (Schulte, 1993; Tucker and Fettiplace, 1995). Although the activity of PMCA is more obvious than the activity of NCX in hair cells (Tucker and Fettiplace, 1995), it is unlikely that the direction of ion flow through PMCA would be sensitive to changes in membrane voltage.

Sodium-calcium exchanger:

There are three members of the NCX gene family (Blaustein and Lederer, 1999). The coupling ratio of ion exchange is generally 3 Na^+:1 Ca^{2+} (Hilgemann, et al., 1991). Its activity is bi-directional and dependent on the concentration of cytosolic [Na^+], which is set by the activity of the sodium-potassium ATPase. There is evidence for a sodium-calcium exchanger in guinea-pig OHCs: 1) removal of extracellular sodium causes an increase in cytosolic calcium concentration and a decrease in sodium concentration, 2) BAPTA inhibits the decrease in sodium concentration due to removal of external sodium and 3) sodium cyanide, an inhibitor of ATP production, causes an increase in cytosolic calcium, but did not affect the rise due to removal of external sodium (Ikeda et al., 1992). The NCX type and the coupling ratio for Na^+ and Ca^{2+} through the NCX in hair cells are unknown, however.

RESULTS

Calcium noise in bullfrog saccular hair cells:

As described in Ch. III, Fig. 26, brief fluctuations in fluorescence intensity were observed in at least 8 bullfrog saccular hair cells. However, because of the brevity of the voltage steps applied, collection of sufficient data points to test the voltage effect on calcium noise was not possible. There were at least 2 saccular cells that exhibited fluctuations in fluorescence intensity and that were exposed to longer voltage steps, one of which is presented here. Further analysis of the effect of voltage on calcium noise was carried out in three ways: 1) sequential montage of an image stack to illustrate changes in fluorescence intensity throughout the footprint over time, 2) image subtraction to locate the sites of any differences in fluorescence intensity in response to a voltage step and, in one case, 3) variance analysis of small regions of interest (ROIs) drawn over the sites exhibiting a pronounced change in fluorescence intensity determined from the subtracted images.

Frame by frame illustration of the effect of membrane voltage on calcium noise:

The average of every two frames of a bullfrog saccular hair cell image stack is displayed as a sequential montage where each image represents 40 ms (Fig. 50 A). The timing of the voltage step from -60 to 0 mV is shown above the image montage. An increase in fluorescence intensity is seen at the dense body during the voltage step to 0 mV indicating the VGCC cluster there (Fig. 51 A, *arrow*). Arrowheads indicate sites of calcium noise before and after the voltage step. Note the diminished fluorescence intensity at these sites during the first 80 ms of the voltage step. One site slowly regained activity after 80 ms after the start of the voltage step, whereas, the other two sites remained diminished throughout the remainder of the voltage step and increased fluorescence intensity upon membrane repolarization. Calcium noise was observed in 8 out of 9 bullfrog saccular hair cells. Lowered frequency of calcium noise events due to a voltage step to 0 mV was measurable in 2 bullfrog saccular hair cells.

Identifying voltage-sensitive sites by image subtraction:

The image stack shown in Fig. 50 A was excised into three sets of 180 ms mini-stacks (9 frames per mini-stack) of the time before, during and after the voltage step. Each mini-stack was averaged and each average was likewise referred to as “before”, “during” or “after” images (Fig. 50 B). In order to highlight any local changes in footprint fluorescence as a function of voltage, either the “before” or “after” image was subtracted from the “during” image (Fig. 50 C, *left* and *right*, respectively). After image subtraction, a value of 1000 is added to every pixel to avoid negative pixel intensity values. Therefore, regions of the footprint that exhibit no change in fluorescence intensity with voltage appear grey and have pixel values similar to background glass fluorescence where there was no cell. Dark spots in the subtracted image would result if the average fluorescence intensity was higher prior to the voltage step than during, as would occur if calcium noise diminished during the voltage step. However, a dark spot in the subtracted image can also be generated if the fluorescence intensity of a defined region goes below background footprint fluorescence during the voltage step. This might occur if localized voltage-dependent calcium efflux or calcium sequestration happened there. On the other hand, bright spots in the subtracted image would indicate an increase in fluorescence intensity during the voltage step and would likely reflect calcium influx through VGCCs at the dense body present in these cells. Circular 5 x 5 pixel ROIs were drawn over two of the three dark spots that were away from the edge in the subtracted images (ROI 1 and ROI 2), over the one bright spot (ROI 3) and over a region of the footprint where there was no change in fluorescence (ROI 4). A rectangular 5 x 24 pixel region was also drawn over an area of glass where there was no cell (Fig. 50 D).

Measurement of fluorescence intensity at voltage-sensitive sites over time:

To determine whether the dark spots in the subtracted images are due either to calcium noise or removal of calcium in some way, the fluorescence intensity at various ROIs were measured in each frame of an image stack over time (Fig. 51). Fig. 51 A illustrates the regions for which the fluorescence intensity is measured in the image stack represented in Fig. 50. The fluorescence intensity within the rectangular glass region was subtracted from the values for each circular ROI in each frame and the glass-subtracted values are plotted in Fig. 51 C. As illustrated in Fig. 50, the fluorescence intensity at the dense body increased during the same voltage step when the fluorescence intensity at sites of calcium noise decreased. These changes in fluorescence intensity closely follow changes in voltage within the 20 ms time resolution of image acquisition. The fluorescence intensity at ROI 2 increased after the first 80 ms of the voltage step, but not at ROI 1 which exhibited no activity for the remainder of the voltage step. Note that at ROI 4, the fluorescence intensity remained constant throughout the recording.

Variance analysis of calcium noise:

To illustrate that the calcium noise seen as stochastic fluctuations in fluorescence intensity becomes less noisy during the voltage step, the coefficient of variance at each ROI over time was calculated for each “before”, “during” or “after” mini-stack (see Fig. 50 B). The variance was divided by the average fluorescence intensity at each ROI for each “before”, “during” or “after” mini-stack to yield the coefficient of variance (CV) (Fig. 51 D). The largest changes in the CV occurred at calcium noise sites ROI 1 and ROI 2; a decrease from 0.61 to 0.12 was observed at ROI 1 and an increase from 1.11 to 6.38 was observed at ROI 2 during the voltage step. The CV was elevated after the voltage step relative to before at both ROI 1 (3.09) and ROI 2 (4.01). In contrast, the CV increased only very slightly at the background ROI 4 and at the dense body ROI 3 throughout the recording (ROI 4: before = 0.20, during = 0.33, after = 0.50; ROI 3: before = 1.07, during = 1.28, after = 1.39). Despite a large increase in average fluorescence intensity during the voltage step at ROI 3, a constant CV correlates with the lack of significant frame by frame changes before, during or after the voltage step.

Calcium noise in chick cochlear hair cells:

If the full image recording of the chick cochlear hair cell shown in Ch. III, Fig. 47 is visualized with additional ROIs drawn within the footprint, the development of calcium noise at one ROI becomes apparent. Calcium noise was also observed in at least 2 other chick cochlear hair cells out of 57. Analysis similar to that used for the bullfrog saccular hair cell presented in Figs. 50 and 51 was used to observe the effect of membrane voltage on calcium noise in chick cochlear hair cells.

The appearance of calcium noise in a cell that responds to ACh:

Fig. 52 illustrates the full voltage-clamp recording trace that was, in part, presented in Ch. III, Fig. 47. Repeated 90 ms applications of ACh (every 3 sec starting at 1.2 sec) at various membrane voltages (changed every 3 sec) and the resulting currents are shown in Fig. 52 B. Fig. 52 A depicts the same regions shown in Ch. III, Fig. 47 (ROI 1 and ROI 2 and the glass region) as well as two other regions drawn within the footprint (ROI 3 and ROI 4). The non-glass-subtracted fluorescence intensities at each of these regions, including the rectangular glass region, are presented in Fig. 52 C. Note that the trace representing the "glass" fluorescence intensity reflects the auto-fluorescence of ACh and the timing of the passage of perfusion solution over this region towards the cell. It can be seen that the fluorescence intensity increases dramatically over time at one region (ROI 4) whereas the baselines of the other regions within the footprint (ROI 1 – 3) increase more slowly (Fig. 53 C). The fluorescence intensity at ROI 4 roughly doubles around the time the membrane voltage is stepped from -40 to -60 mV. However, the fluorescence intensity of ROI 4 remains elevated and continues to rise to the end of the recording even though the membrane voltage has been brought back to and maintained at -40 mV throughout this time. Small increases in fluorescence intensity are also visible at ROI 4 that roughly correlate with the timing of the ACh puff, but the fluorescence intensity at this site fluctuates too widely to determine whether or not the correlation is merely coincidental. Earlier in the recording, ROI 4 did not exhibit an increase in fluorescence intensity in response to the ACh puffs at 1.2 and 4.2 sec.

Image subtraction to determine whether calcium noise is voltage-sensitive:

To see whether a voltage step to 0 mV has the same effect on calcium noise in the chick cochlear hair cell as demonstrated in the bullfrog saccular hair cell in Fig. 51, a voltage step from -40 to 0 mV was applied following the recording shown in Fig. 52. Image subtractions of an image stack during which the voltage step was applied were made. Mini-stacks each comprised of 200 ms of the time before, during and after the voltage step were excised and averaged into three "before", "during" and "after" images (Fig. 53 A). Again, the "before" image was subtracted from the "during" image as was the "after" image (Fig. 53 B, *upper* and *lower*, respectively). As expected, a dark spot can be seen at the site where calcium noise is located and where ROI 4 is drawn (Fig. 53 C).

Measurement of fluorescence intensity at the site of calcium noise over time:

Figs. 53 D and E show the voltage step and the corresponding whole-cell current, respectively. The current is outward because the internal solution is free of potassium blockers such as TEA or cesium. The glass-subtracted fluorescence intensity at each ROI drawn within the footprint (Fig. 53 C) over time is shown in Fig. 53 F and time aligned with the traces in *D* and *E*. It can be seen that the fluorescence intensity at ROI 4 is the only region that diminishes during the voltage step and that the fluorescence intensity at the other three regions remains constant.

Voltage-sensitivity of multiple calcium noise events throughout a hair cell:

Another chick cochlear hair cell where calcium noise was observed is shown in Fig. 54 and 55. However, the calcium noise in this cell was not necessarily localized to specific sites and appeared to occur stochastically in various regions throughout the footprint. Fig. 54 A presents a montage of successive frames of an image stack each representing 40 ms starting from 120 to 680 ms of a recording. Frames following a gap in time are labeled in ***bold***. Frames indicated by an asterisk were acquired during a 300 ms voltage step from -40 to 0 mV. The fluctuation of calcium noise transients is not as obvious in this montage as was observed in the montage of Fig. 50 A and are therefore shown in pseudocolor. Fig. 54 B shows three image averages during the time "before", "during" and "after" the voltage step each representing 240 ms and scaled to the same intensity. Image subtractions of the "before" and "after" image averages from the "during" image average reveal that the locations of the dark spots are not found in the same regions of the footprint (Fig. 54 C, *left* and *right*). Indeed, the image stack observed in real time shows stochastic calcium noise events activity throughout the footprint. To measure fluctuations in fluorescence intensity over time, circular 10 x 10 pixel ROIs were drawn over four regions of the footprint. ROI 1 – 3 were drawn over the darkest regions that were observed. ROI 4 was drawn over a region where the least amount of change in fluorescence intensity was seen in the subtracted images in Fig. 54 C (Fig. 54 D).

Measurement of fluorescence intensity at multiple calcium noise sites over time: Fig. 55 A shows the DIC image of the cell with the recording pipette on the right side of the cell. The pipette used to perfuse ACh onto the hair cell is off the image on the left-hand side. Note that a 90 ms puff of 100 μM ACh was applied during the voltage step at 0.242 sec. However, measurement of ACh autofluorescence of ACh perfusion within the rectangular glass region (shown in 55 B) placed in the path of perfusion indicates that ACh did not reach the cell until after 0.443 sec (not shown). Perhaps, the solution within the microperfusion pipette was diluted by back flow of the bath saline into the tip. Regardless of whether ACh was perfused, the glass-subtracted fluorescence intensities at all regions measured (ROI 1 – 4) diminished to some extent (Fig. 55 E). ROI 1 exhibits a ~140 ms increase in fluorescence intensity during the voltage step starting at 0.302 sec. Since ACh autofluorescence was not detected until 0.443 sec, it is unlikely that this event is ACh related, unless the concentration needed for a cellular response is below the resolution of the camera. The fluorescence intensity at ROI 4 also diminished to a lesser extent by about 50 % of what was observed at the other three regions. The degree of diminishment of fluorescence intensity at each region in Fig. 55 E correlates with the degree of fluorescence change at the same sites depicted in the subtracted images shown in Fig. 54 C.

Non-voltage-gated calcium flux in chick cochlear hair cells:

In addition to calcium noise, it was also noticed that fluorescence intensity of the footprint followed membrane voltage in a manner that is suggestive of a non-voltage gated calcium flux at the plasma membrane. It was also noticed that this proposed non-voltage gated calcium flux develops slowly over time after 1 min of recording and can appear at different times at various regions within the same footprint. The relationship between footprint fluorescence within the evanescent field and membrane voltage was measured in two ways in order to characterize this non-voltage-gated calcium flux at the plasma membrane of chick cochlear hair cells. In one measurement, the fluorescence intensity within the whole footprint ROI was considered. In the second measurement, circular 10 x 10 pixel ROIs were drawn over local regions within the footprint that exhibited marked differences from the behavior of the whole footprint. It was observed that various regions exhibited differences in the amount of fluorescence intensity at a given membrane voltage and in the timing by which the non-voltage gated calcium flux appeared.

Whole footprint fluorescence intensity changes with membrane voltage: Initially, voltage steps to two voltages, 0 and -100 mV, from a holding potential of -40 mV were used for measuring changes in whole footprint fluorescence intensity. In addition, the voltage steps to these two voltages were applied within two different time ranges, <1 min and between 1 – 2 min, starting from the time the first image was acquired in a given cell. Cells were included in the data set if their holding current was less than 200 pA from 0 pA at -40 mV and if the footprint area was > 600 pixels^2. Multiple measurements were pooled whether or not they were from the same cell or not. However, only the first measurement for a voltage step to a given voltage for any time frame was used if another voltage step to the same voltage within the same time frame was applied in a given cell. The total number of different cells used for this experiment was 43.

Fig. 56 A is a DIC image of a typical SHC resting on the glass such that the hair bundle is pointing away from the glass towards the viewer. Fig. 56 B shows the corresponding footprint generated by the evanescent field for the cell shown in *A* at the same magnification. The footprint ROI drawn over the perimeter of the footprint is shown in blue and the rectangular 30 x 40 pixel region of glass with no cell is outlined in white. Fig. 56 C and D illustrates the combined electrophysiological and footprint fluorescence intensity recordings to the two voltage steps within two time ranges for the hair cell shown in *A* and *B*. The *top traces* in *C* and *D* show the timing of the membrane voltage step in each case. The *middle traces* show the corresponding whole-cell voltage clamp currents at two time ranges, <1 min (*black traces*) and between 1 – 2 min (*grey traces*). The *lower traces* show the corresponding glass-subtracted footprint F/F_0 in each frame during which the voltage step indicated above was applied within two different time ranges, again, <1 min (*black traces*) and between 1 – 2 min (*grey traces*). As in previous figures, the glass fluorescence within a rectangular 30 x 40 pixel region is first subtracted from the fluorescence intensity of the footprint in each frame in time. Secondly, the glass-subtracted values for the footprint fluorescence intensity in each frame are normalized to the average glass-subtracted fluorescence within the 10 frames (200 ms) immediately preceding a given voltage step yielding the F/F_0 for the footprint in each frame.

The corresponding image subtractions for the traces shown in Fig. 56 C and D, *bottom traces*, are shown in Fig. 57 A and B. These images were made, as in Fig. 50 C, 53 B and 54 C, by subtracting the 10 frame “before” mini-stack average from the 10-frame “during” mini-stack average only. All images in A, *left* and *right*, and B, *left* and *middle*, were scaled to the same intensity range. A voltage step to 0 mV within <1 min shows an increase in whole footprint fluorescence intensity that is likely due to VGCC activity (Fig. 57 A, *left*). Surprisingly, a voltage step to 0 mV applied later between 1 – 2 min generates a decrease in fluorescence intensity (Fig. 57 A, *right*). On the other hand, a voltage step to -100 mV generates a small increase, if any, in footprint fluorescence before 1 min (Fig. 57 B, *left*) which becomes much greater when the voltage step is applied between 1 – 2 min (Fig. 57 B, *middle*). Fig. 57 B, *right*, was scaled so that the image does not appear oversaturated.

Figs. 57 C and D show the pooled responses of a total of 42 different cells. Data represents the difference between the average glass-subtracted F/F_0 of the 10 frames preceding the voltage step from the average glass-subtracted F/F_0 of the middle 10 frames (200 ms) yielding the $\Delta F/F_0$ of the footprint to a given voltage step. Data values +/- SE (n = cells) are: 0.06 +/- 0.02 (0 mV, <1 min, n = 37); 0.01 +/- 0.01 (0 mV, 1 – 2 min, n = 13); 0.02 +/- 0.01 (-100 mV, <1 min, n = 15); 0.09 +/- 0.02 (-100 mV, 1 – 2 min, n = 7). Statistical analysis using the t-Test (assuming equal variances, α set to 0.05, two-tail) indicates that the p value is 0.123 for values following a voltage step to 0 mV and a p value of 0.003 following a voltage step to -100 mV for both time points. Fig. 57 E shows the average footprint fluorescence intensity at -40 mV within 200 ms immediately preceding the voltage step for most of the 43 cells represented in *C* and *D*. Data values +/- SE (n = traces) are: 144 +/- 22 (<1 min, n = 51) and 216 +/- 53 (1 – 2 min, n = 16). Fig. 57 F shows the average holding current (I_{hold}) at -40 mV within the same 200 ms evaluated in Fig. 57 E for most of the cells represented in *C* and *D*. Data values +/- SE (n = traces) are: -5 +/- 9 (<1 min, n = 47) and 8 +/- 18 (1 – 2 min). Statistical analysis using the t-Test (assuming unequal variances, α set to 0.05, two-tail) indicates that basal footprint fluorescence intensity values at <1 min and between 1 – 2 min has a p value = 0.022. Likewise, when the same statistical parameters were applied for the holding currents at the two time point, the p value = 0.520, indicating that the integrity of the electrophysiological recordings of the cells represented in Fig. 57 *C* and *D* do not change much within 2 min.

Whole footprint F/F_0 responses to voltage steps to various potentials:

A larger range of voltages was applied to chick cochlear hair cells to characterize the influence membrane voltage has on the footprint fluorescence intensity more fully. Data was acquired in the same way as the data shown in Figs. 56 and 57 except that test voltages to -100, -70, 0, +20 and +40 mV from -40 mV were all included. Voltage steps were applied within <1 min or between 1 – 2 min from the first image acquisition per cell. Data for test voltages to -100 and 0 mV in this experiment are the same data already shown in Fig. 56 and 57. Multiple data points collected from any given cell were pooled whether or not one cell provided data points for more than one time range. However, only data for the first recording within a given time range for a particular voltage step was used from any given cell. 43 different cells were used in this experiment.

An example of a 6 sec voltage step protocol applied to hair cells is shown in Fig. 58 A. The membrane voltage was moved through a succession of voltages from a holding potential of -40 to 0, -70, -100, 0, +20, +40, 0 and -40 mV each for a duration of 400 ms. Between each test voltage, the membrane voltage was brought back to -40 mV for 400 ms. Fig. 58 B shows an example of the corresponding whole-cell currents to the voltage step protocol applied within <1 min (*black trace*) and between 1 – 2 min (*grey trace*) of recording in one hair cell. Note that these traces do not represent isolated calcium currents since the internal pipette solution is free of potassium channel blockers such as TEA and cesium. The only major difference in the whole-cell current between the two time points occurs during the hyperpolarizing voltage steps to -70 and -100 mV where the inward current is more pronounced at <1 min than between 1 – 2 min. Fig. 58 C shows the corresponding whole footprint F/F_0 traces for the same cell and in the same time scale as for the current traces shown in *B*. Two striking differences are seen in the footprint F/F_0 traces acquired at the two time points. One is the drastic reduction of the F/F_0 increase during a voltage step to 0 mV at 1 – 2 min as compared with data acquired within <1 min. The second is the appearance of a large increase in footprint F/F_0 during the voltage step to -100 mV applied between 1 – 2 min that was not there previously when the same voltage step was applied within <1 min. Moreover, the second voltage step to 0 mV at 2.8 sec yielded a reduced increase in F/F_0 as compared with the first voltage step to 0 mV at 0.4 sec, even though the outward current was slightly larger. A reduction in the footprint F/F_0 was also seen at +20 and even more so at +40 mV, perhaps because the driving force for calcium goes down as the reversal potential for calcium is approached. However, the last voltage step to 0 mV is about the same amplitude to the voltage step to +40 mV applied just before it implying a run-down of F/F_0 response over time. This run-down of the response could be due either to an intrinsic change in ion permeability across the plasma membrane or a depletion of calcium store calcium concentration.

Pooled footprint $\Delta F/F_0$ responses to various membrane potentials:

Multiple footprint $\Delta F/F_0$ responses to a voltage step protocol such as that illustrated in Fig. 58 A, or to a shorter version with less voltage steps or individual voltage steps to a given voltage from -40 mV, were collected from 43 different chick cochlear SHCs and shown in Fig. 59. Since data from only the first footprint F/F_0 response per voltage, per time point from any given cell was included in the data set, F/F_0 responses from a second voltage step to 0 mV, such as would occur in the voltage protocol shown in Fig.

58 A, would be left out. $\Delta F/F_0$ was always calculated by subtracting the average glass-subtracted footprint F/F_0 within 200 ms immediately preceding each test voltage from the average glass-subtracted footprint F/F_0 within 200 ms of the middle of each test voltage step.

Within the first minute of whole-cell voltage clamp and image recording, the relationship between the footprint fluorescence intensity and voltage resembled what one would expect the current to voltage (IV) plot for a VGCC flux to look like (Fig. 59 A, *black diamonds* and see *arrows* above). The IV plot for VGCC channel activation would show minimal calcium currents due to closed channels at -50 mV or lower, and an increasing in calcium current as channels open at around -50 mV towards a peak current at 0 mV which diminishes as the voltage approaches the reversal potential for calcium ($E_{Ca^{2+}}$) close to +40 mV. Data values +/- SE for voltage steps (n = cells) applied <1 min are: 0.02 +/- 0.01 (-100 mV, n = 15); 0.01 +/- 0.00 (-70 mV, n = 14); 0.06 +/- 0.02 (0 mV, n = 37); 0.05 +/- 0.06 (+20 mV, n = 2); 0.03 +/- 0.03 (+40 mV, n = 2). This pattern changes, however, after 1 min of recording when the voltage dependence of footprint $\Delta F/F_0$ is lost and becomes linear, *grey squares*. Data values +/- SE for voltage steps (n = cells) applied between 1 - 2 min are: 0.09 +/- 0.02 (-100 mV, n = 7); 0.04 +/- 0.02 (-70 mV, n = 5); 0.01 +/- 0.01 (0 mV, n = 13); -0.01 +/- 0.03 (+20 mV, n = 2); -0.01 +/- 0.03 (+40 mV, n = 2). Statistical analysis using the t-Test (assuming equal variances, α set to 0.05, two-tail) indicates that $\Delta F/F_0$ responses to: -100 mV at <1 min and 1 – 2 min has a p value = 0.003; -70 mV at <1 min and 1 – 2 min has a p value = 0.002; 0 mV at <1 min and 1 – 2 min has a p value = 0.123; +20 mV at <1 min and 1 – 2 min has a p value = 0.483; +40 mV at <1 min and 1 – 2 min has a p value = 0.401.

Pooled footprint $\Delta F/F_0$ responses to +40 mV:

Fig. 60 shows pooled footprint $\Delta F/F_0$ responses to voltage steps to +40 mV from 7 different cells to illustrate that the footprint $\Delta F/F_0$ seems to diminish below the basal footprint fluorescence. This suggests that calcium efflux into the extracellular medium may occur and may be due to voltage-sensitive active transport. However, it may also reflect a voltage-dependent calcium sequestration into calcium store organelles such as the synaptic cisternae. Data values +/- SE (n = cells) are: 0.03 +/- 0.03 (<1 min, n = 2); -0.01 +/- 0.03 (1 – 2 min, n = 2); -0.03 +/- 0.03 (2 – 3 min, n = 2); -0.04 +/- 0.03, (3+ min, n = 3). The $\Delta F/F_0$ value at 3+ min includes data from 3 cells, however, 2 values were included from one cell since 1 data point was acquired between 3 – 4 min and the second was acquired between 4 – 5 min. Statistical analysis using the t-Test (assuming equal variances, α set to 0.05, two-tail) to compare values at <1 and 3+ min yields a p value = 0.52 and may not be significantly different.

Local $\Delta F/F_0$ responses within the same cell to reapplied voltage steps to 0 mV:

While many of the chick hair cells presented in Figs. 57 to 59 had a relatively uniform distribution of similar $\Delta F/F_0$ values in response to changes in membrane voltage, the $\Delta F/F_0$ response in other hair cells in the same data set were not uniform and were not to the same value. Fig. 61 A presents an example hair cell with non-uniform $\Delta F/F_0$ responses within the footprint to the same voltage step. Local changes in $\Delta F/F_0$ within three circular 10 x 10 pixel ROIs were measured and shown in Fig. 61 A, *left-most* *image*. ROI 1 was centered on a site of non-voltage-gated calcium flux determined by image subtraction similar to measurements of calcium noise described earlier. ROI 2 was centered on a site where a VGCC cluster was located and ROI 3 was centered on an area where there was no change in $\Delta F/F_0$ with voltage. A rectangular 30 x 40 pixel ROI representing glass fluorescence (no cell) was used in these cells, the same dimensions as was used for cells in the data sets for Ch. III, Figs. 48 and 49. To measure local differences in $\Delta F/F_0$ with voltage, cells were selected from the same data set used for whole footprint changes provided that multiple time points were taken in the same cell and footprint areas were >1000 pixels^2. The larger footprint area increased the likelihood of capturing varied responses in $\Delta F/F_0$ relative to voltage.

To illustrate local changes in $\Delta F/F_0$ when the membrane voltage was stepped from -40 to 0 mV, the image stacks were excised into two 10 frame mini-stacks, "before" and "during" the voltage step. The average fluorescence intensity of the "before" mini-stack was subtracted from the "during" average. The result is the difference in fluorescence intensity at 0 mV relative to the fluorescence before when the cell was held at -40 mV. A slight difference in how the subtracted images were used from previous figures is that the subtracted images for multiple voltage step applications to 0 mV over time were formed into a new stack. ROIs 1-3 were drawn over three areas within the footprint of this new stack of subtracted images as well as the rectangular glass ROI. The average glass fluorescence was subtracted from each ROI in each frame and the glass-subtracted fluorescence intensity values are shown in Fig. 62 B. Subtracted images of the “before” from the “during” image stack averages relative to the voltage step are shown above the corresponding glass-subtracted values in time. Note that, even though the fluorescence intensity at each ROI is different from each other at each time point, the changes in intensity occur roughly in parallel with each other over time. In other words, the fluorescence response to voltage at each ROI appears to ultimately result in a uniformity of the response across the footprint. It is as if the increase in fluorescence intensity due to VGCCs, if present, is eventually lost over time and the generation of a non-voltage-gated calcium current develops slowly at different rates from region to region within a given cell. In the cell shown in Fig. 61, the increase in fluorescence intensity with a voltage step from -40 to 0 mV becomes negative across most of the footprint after ~3 min.

DISCUSSION

The appearance of calcium noise resembling “spark”-like flickers in fluorescence intensity was observed in both bullfrog saccular and chick cochlear hair cells using TIRF microscopy and calcium-sensitive Fluo dye. Acutely isolated hair cells were plated onto glass coverslips and the cytosol was perfused with 200 μM Fluo dye through the voltage clamp recording pipette. Illumination of the cytosol within ~100 nm from the plasma membrane was achieved with an evanescent field of 488 nm laser light emanating from beneath the coverslip as described earlier. Durations for each calcium noise event ranged from ~60 to ~500 ms. Calcium noise flickers in fluorescence intensity were, in at least 3 cells, either directly or indirectly affected by membrane voltage; a voltage step from the holding potential of -40 to 0 mV temporarily halted calcium noise activity in those cells where calcium noise was present and measurable. In addition to having some effect on calcium noise, membrane voltage could also influence basal footprint fluorescence intensity in a manner that is distinct from VGCC activity. The relationship between basal footprint fluorescence intensity and membrane voltage resembled a non-voltage-gated calcium flux governed primarily by the driving force for calcium across the membrane. This non-voltage-gated calcium flux at the plasma membrane develops gradually over time and can be localized to distinct areas within the footprint.

Calcium noise in hair cells:

Sometimes calcium noise resembling “spark”-like fluctuations in Fluo dye fluorescence intensity was observed in either bullfrog saccular or chick cochlear hair cells that were voltage-clamped and imaged with TIRF microscopy. What mechanism underlies the generation of calcium noise in hair cells? Perhaps, the recording pipette has caused some physical distortion of the synaptic cistern, which closely apposes the plasma membrane. Alternatively, if the calcium noise observed here is not an artifact of membrane distortion, it may be the result of small inward calcium fluxes that serve to refill the calcium stores; the efferent synapse may utilize calcium-permeable channels in the plasma membrane to fulfill this purpose. In many cells, a steady increase in footprint fluorescence intensity over time was observed. Elevated cytosolic calcium during the recording could cause the release of calcium from stores, such as the synaptic cistern, by CICR.

It is possible that calcium noise observed in both bullfrog saccular and chicken cochlear hair cells is the result of calcium release through RyR channels (Fig. 62). Hair cells are sensitive to ryanodine (Kennedy and Meech, 2002; Marcotti et al., 2004) and may express RyRs on the synaptic cistern. To characterize calcium release events in hair cells with TIRF microscopy, one could test whether calcium noise is sensitive to calcium store depletion using thapsigargin, a SERCA blocker. Upon treatment with thapsigargin, an initial increase in calcium noise may be observed as the calcium store empties that diminishes once the store is depleted. One could also apply blockers of RyRs such as ruthenium red (Smith et al., 1988).

Another explanation for the appearance of calcium noise could involve the stochastic opening of calcium-permeable channels in the plasma membrane. Calcium fluxes into the cytosol either by calcium release from store organelles or calcium influx across the plasma membrane would both be visible within the evanescent field. It is known that VGCCs are expressed in the plasma membrane and, although clusters of VGCCs are infrequently found in SHCs, they sometimes are found at the efferent synapse (Fig. 38, *arrow*). Another possibility that has not yet been described in hair cells is that calcium release-activated calcium (CRAC) channels could be expressed in the post-synaptic plasma membrane at the efferent synapse (Fig. 63). CRAC currents have been described for various non-excitable cell types (Parekh and Putney, 2005, review). It is thought that CRAC channels are activated in response to calcium store calcium release for the purpose of refilling the emptying calcium store. This is a tempting explanation for the results here since the synaptic cistern in hair cells seems to play an integral part of the efferent synapse as a calcium store that would need constant refilling.

Calcium noise and membrane voltage:

It was also observed that calcium noise events are influenced by depolarizing membrane voltage steps to 0 mV. One way to illustrate this effect is by subtracting the average fluorescence before or after a voltage step from the average fluorescence during the voltage step. Image subtraction to look at the effect of membrane voltage on calcium noise was carried out in three hair cells: one bullfrog saccular hair cell and two chick cochlear hair cells. The results are shown in Figs. 50 C, 53 B and 54 C. The dark spots in the subtracted images indicate sites where the average fluorescence diminished during the voltage step relative to the average fluorescence either before or after. A voltage-sensitive reduction in calcium noise activity may reflect either: 1) a voltage-sensitive sequestration of cytosolic calcium into store organelles, such as the synaptic cisternae or mitochondria, or, 2) lessened or undetectable calcium influx through open calcium-permeable channels in the plasma membrane when the driving force for calcium approaches the reversal potential for calcium at depolarized potentials. Although the concentration gradient is favorable for calcium sequestration, it is unclear how voltage changes at the plasma membrane could influence organellar transporter activity without electrical continuity. On the other hand, a depolarizing membrane voltage could diminish the driving force for calcium influx through calcium-permeable channels in the plasma membrane (Fig. 59). Again, calcium influx through either VGCCs or another calcium-permeable channel, such as the CRAC channel, could be involved.

CRAC channels may be visualized in these experiments if the efferent synapse and the synaptic cistern are located where the footprint is. However, if the synaptic cistern is indeed located at the same sites where calcium noise occurs, it is unknown why an ACh response was not observed there too (Fig. 52 C, compare ROIs 1 and 4 traces). Likewise, it is unknown why only the site of calcium noise diminishes in fluorescence intensity during a voltage step and not the site that responded to ACh in an earlier recording (Fig. 53 F, compare ROIs 1 and 4 traces). It could be, however, that the cistern at the ACh responsive site is further away from the TIRF field for observation than the site where development of calcium noise was observed. Since there was no marker for the synaptic cistern, calcium noise could also reflect calcium release from mitochondria arising from an initial decrement in cell health. The cells, however, appear healthy since electrophysiological recordings show little, although statistically significant, change in the basal fluorescence (Fig. 57 E) and no change in the holding current (Fig. 57 F) at resting voltage over time. Rather, when membrane voltage steps were applied, the fluorescence intensity in one region, but not in others, changes in such a way that is suggestive of localized, non-voltage-gated calcium flux across the plasma membrane (Fig. 53 F).

Experiments to test whether calcium noise plays a direct role or is, at least, a by product of a CRAC channel-calcium store refilling mechanism are: 1) once calcium noise appears, bathe cell in calcium-free bath saline to see if the calcium noise events disappear and then re-appear when the bath is switched back to regular saline, 2) block voltage-sensitive potassium channels with TEA and cesium (cesium could also potentially block calcium release through RyRs from the synaptic cistern) and apply a series of voltage steps to see if an inwardly-rectifying calcium current is observed. To rule out stochastic opening of VGCCs, one could apply cadmium or nifedipine once calcium noise appears to see if the events are blocked. Now that there is a candidate CRAC channel subunit, orai1, one could scan the chicken genome to see if a homologue exists.

Non-voltage-gated calcium flux in chick cochlear hair cells:

What could be causing this anomalous fluorescence intensity change to follow the membrane voltage with tens of milliseconds temporal correlation? It is possible that open channels in the plasma membrane permit the flow of calcium ions according to the driving force dictated by membrane voltage. Indeed, when the $\Delta F/F_0$ of the footprint fluorescence intensity is plotted against voltage between 1 – 2 min of recording, the curve is linear as if calcium flux is un-gated (Fig. 59, *grey trace*). One possible explanation for this phenomenon is that calcium ions flow through open CRAC channels in the plasma membrane. If hair cells express CRAC channels, CRAC channels may play a part in SOCE to refill calcium store organelles.

Recent evidence in Jurkat T cells, proposes at least two molecules that may constitute a SOC channel, Stim (luminal ER calcium sensor) and Orai1 (putative pore subunit of the CRAC channel) (Luik et al., 2006). In fact, the behavior of CRAC activity observed in Jurkat T cells is strikingly similar to the observations in chick cochlear hair cells presented in this thesis. Using 10 mM EGTA introduced through the recording pipette to deplete calcium stores (we used 11 mM EGTA), inward rectifying calcium currents were generated at hyperpolarized membrane potentials. Using TIRF microscopy and Fluo-5F (we used TIRF and Fluo-4), the authors observed an increase in fluorescence during a hyperpolarizing voltage step (Fig. 63). The inwardly rectifying currents and increase in fluorescence during membrane hyperpolarization were attributed to CRAC channels activity. It is possible, then, that the use of 11 mM EGTA in chicken cochlear hair cells may have activated CRAC channel activity that was seen as an increase in footprint fluorescence when we applied hyperpolarized membrane potentials.

The idea that SOCE could occur in hair cells is further supported by the observation that it takes time for the non-voltage-gated calcium flux to develop. Fig. 61 illustrates the development of the non-voltage-gated current across the footprint of one chick hair cell over time. On average, cells exhibit a non-voltage-gated calcium flux after only 1 min (Figs. 56 - 59); however some cells, including the one shown in Fig. 61, exhibit a variability of the onset within the footprint. If the ER, or synaptic cistern, mobilizes toward the plasma membrane as the calcium store empties, as described in Luik et al. (2006) (Fig. 64), it is likely that this movement would take time. Movement of organelles, especially those that have a long shape such as the synaptic cistern, may move slowly toward the plasma membrane in a time scale similar to the development of the non-voltage-gated calcium flux we observe in chick hair cells. Once the synaptic cistern reaches the plasma membrane, SOC channels may form and the appearance of an increase in fluorescence intensity with hyperpolarizing membrane potentials might then be accounted by calcium influx through them.

At depolarizing membrane voltages, however, it is unclear whether the decrease in footprint fluorescence is due to calcium efflux through open CRAC channels (Figs. 58 - 60). Although open channels in the plasma membrane might explain the response to hyperpolarizing voltages, it is highly unlikely that the driving force for calcium at depolarizing voltages could override the large concentration gradient across the plasma membrane. On the other hand, since the traces in Fig. 60 are normalized to the average fluorescence intensity before each voltage step to +40 from -40 mV, the calculated $\Delta F/F_0$ value at each time point is relative to an increasingly higher cytosolic calcium concentration. Calcium transporters normally expressed in the hair cell plasma membrane to maintain homeostatic levels of cytosolic calcium could be sensitive to a voltage step to +40 mV. Voltage-sensitive calcium efflux, potentiated at depolarized membrane potentials, through calcium transporters would then result in negative $\Delta F/F_0$ values.

Along the same line, perhaps the changes in footprint fluorescence observed with changes in membrane voltage may instead reflect a voltage-sensitive active transport. Possible plasma membrane transporter candidates expressed in hair cells are the sodium-calcium exchanger (NCX) and the plasma membrane calcium ATPase (PMCA). A change in membrane voltage might then be able to actively drive calcium flux across the plasma membrane leading to changes in footprint fluorescence intensity. An indication that a transporter mediates the voltage-sensitive fluorescence intensity changes is the relatively slow onset of the change (for example, see Figs. 55 and 56) compared with a fluorescence change due to flux through VGCCs (Fig. 51). Although PMCA activity has been demonstrated in hair cells, it is less likely to be affected by changes in membrane voltage than the NCX would be. Hyperpolarized potentials could reverse the direction of ion flux through NCX such that sodium is transported out and, in turn, calcium is transported in (Fig. 65).

An experiment to test whether reversal of the NCX could account for the appearance of a non-voltage-gated calcium flux could be to repeat the experiment shown in Figs. 58 and 59 in the presence of elevated external sodium ion concentration. Since the driving force for sodium efflux would be lower than normal when the external sodium concentration is raised, one might expect that the amount of increase in footprint fluorescence intensity (calcium influx) would be lower as well at -100 mV. One could also eliminate external sodium ion concentration by replacing sodium with *N*-methyl-D-glucamine (NMG+) in the bath saline. One might expect that bathing the cell with bath saline lacking sodium would increase the driving force for sodium efflux leading to an increase in footprint fluorescence. Indeed, this has been shown in guinea pig cochlear OHCs (Ikeda et al., 1992). The plot shown in Fig. 59 then would show a steeper linear trace and higher $\Delta F/F_0$ value at -100 mV when the cells are bathed in sodium-free external saline. If the $\Delta F/F_0$ to voltage plot shown in Fig. 59 shows any changes due to changes in external sodium, then NCX could be implicated.

If, however, there is no change in the $\Delta F/F_0$ to voltage plot shown in Fig. 59 despite changes in external sodium concentration, then one could test whether PMCA activity by blocking its activity with vanadate (Goodno, 1979; Tucker and Fettiplace, 1995). If PMCA activity accounts for the increase in $\Delta F/F_0$ at hyperpolarized potentials, then vanadate should block that increase.

As pointed out earlier, it is possible that elevated EGTA calcium buffer concentration used in these experiments (11 mM EGTA) was enough to stimulate calcium release from calcium stores. To test this, one could then use a lower concentration, such as ~1 mM EGTA, to see whether the non-voltage-gated calcium flux appears at all or at a later time than what was observed in Fig. 59. If the non-voltage-gated calcium flux does not appear or appears at a later time, one could then block SERCA transporters normally found on sER membrane with thapsigargin, 2,5-di(tert-butyl) hydroquinone (t-BHQ) or cyclopiazonic acid (CPA) to see whether the increase in footprint fluorescence at -100 mV then causes the non-voltage-gated calcium flux to appear.

SUMMARY AND CONCLUSIONS

Afferent synapse:

Experiments were carried out to identify the afferent synapse and image exocytosis at the active zone in living hair cells. We dialysed the membrane-impermeable form of Fluo-3 dye into the cytosol from a patch pipette to see if dense bodies and calcium entry could be imaged with TIRF microscopy. We found that that the calcium-sensitive fluorescent dye, Fluo, could be used in living, isolated saccular hair cells to identify both the dense body and the L-type calcium-entry sites there. Next, we further demonstrated that the Fluo-3 labeled dense bodies are indeed ribbons, by immunofluorescent labeling of fixed saccular hair cells with antibody that recognizes ribeye, a component of ribbons. Voltage clamp and membrane capacitance recordings, without TIRF imaging, also demonstrated that the L-type VGCC is necessary for exocytosis in these cells. Indirect measurement of vesicular activity in hair cells could be monitored with membrane capacitance recordings and has revealed the presence of a pool of vesicles that fuses with the membrane at a fast rate within 20 ms of stimulation. A slower rate of exocytosis was observed with longer voltage step durations. The faster exocytic rate could reflect the readily-releasable pool of vesicles seen clustered around the dense body in electron micrograph images of hair cells. Lastly, TIRF microscopy could image exocytic FM1-43 dye release, but it is unclear whether these events are synaptic vesicles or another endosomal organelle.

Efferent synapse:

The goal of these experiments was to test whether the synaptic cistern, a presumed calcium store, activates SK channels in response to nAChR activation by CICR at the efferent synapse. We initially used either ionophoresis or microperfusion to locally apply ACh onto isolated bullfrog saccular or chick cochlear hair cells while recording with whole-cell voltage or current clamp to test SK channel activation. We found that not many bullfrog saccular hair cells respond to ACh puff. In cells that do respond, the current is always inward from -40mV to more hyperpolarized potentials, which suggests that the SK component is lacking. SK channels may have been partially damaged by the isolation procedure. However, it could also mean that the efferent terminals are too localized in these cells to detect them with ACh puff by chance, or not all efferent synapses are cholinergic in the cells since synaptic cisternae were not always found at presumed efferent terminals in electron micrographs. Unfortunately, it may also have been that the cells chosen for the recordings were of a subtype of bullfrog saccular cell that do not have an apamin-sensitive current.

Since the SHCs of the chick cochlea have a large efferent terminal at the base and a corresponding synaptic cistern directly opposite the length of the terminal, we used these cells for testing the ACh response. In chick SHCs, we found that most cells tested respond to ACh puff. We saw that the ACh-activated current is: 1) voltage-sensitive and reverses around the expected reversal potential for potassium, 2) that the fast calcium buffer, BAPTA, can shift the reversal potential of the ACh response towards the reversal potential for calcium, and 3) that the response is sensitive to both α-BTX and apamin. These data indicate the presence of both nAChR and SK channels in chick SHCs, as it has been well-described in the literature.

Next, we wanted to image calcium fluxes in response to ACh puff at the plasma membrane directly with TIRF microscopy, a method of illumination that effectively limits laser light to within 100 nm of the plasma membrane. This method could allow one to image the opening and closing of calcium-permeable channels at the plasma membrane as well as from synaptic cisternae. We found no Fluo dye fluorescence changes in response to ACh in any bullfrog saccular hair cell. However, there was one chick SHC that did exhibit a localized Fluo-4 fluorescence increase in response to a puff of ACh that was also detected in the whole-cell recording pipette at the same time. The fluorescence increase in response to ACh was not voltage-sensitive whereas the induced current was. Furthermore, the amplitude of the fluorescent response was unaltered by voltage as well. This indicates that the fluorescence intensity increase is an all-or-none response to ACh that possibly reflects either calcium influx through nAChR channels or calcium-release from the synaptic cisternae, or both. However, it was not determined for certain since not many SHCs had a large enough footprint, which limited our chances to image these small changes in fluorescence.

Calcium noise:

Unexpected fluorescence transients, called calcium noise, imaged with TIRF microscopy indicate another activity in both bullfrog saccular and chick cochlear hair cells. It is unknown from these experiments what calcium source accounts for the calcium noise events observed here. Possibilities include stochastic calcium release from calcium store organelles, such as the synaptic cisternae, or stochastic calcium influx through VGCCs or SOC channels, such as CRAC channels. In some cells, calcium noise appeared to be voltage-sensitive diminishing in frequency at depolarized potentials. Calcium release from store organelles is unlikely to be affected by changes in membrane voltage unless there was electrical continuity between store organelles and the plasma membrane, which has not been described for hair cells. However, a change in membrane voltage could conceivably affect the driving force for calcium flux across the plasma membrane through calcium-permeable channels, such as VGCCs or CRAC channels.

Non-voltage-gated calcium flux at the membrane:

In addition to stochastic fluorescence transients, the average fluorescence intensity of the footprint of chick cochlear hair cells appeared to exhibit steady-state voltage-sensitivity that was unlike VGCC activity. These steady-state voltage-sensitive footprint fluorescence intensity changes, termed non-voltage-gated calcium fluxes, developed only after ~1 min from initial recordings in a given cell. Despite a slowly increasing concentration of calcium over time, hair cells exhibited little or no change in the holding current, which suggests that the health of hair cells is maintained throughout these experiments. However, this slowly increasing footprint fluorescence could indicate the development of CICR in hair cells. The cytosol of hair cells was dialysed with a relatively high concentration of EGTA, a calcium buffer. It is possible that this amount of calcium buffer is sufficient to induce calcium release from calcium store organelles, such as the synaptic cistern, which could fit within the evanescent field.

When voltage steps from -100 to +40 mV are applied early in the recordings, the relationship between footprint fluorescence and voltage at first looks like VGCC activity where little change is seen when VGCCs are closed and an increase is seen when VGCCs are open. However, when the same voltage step protocol is applied to the same cell after 1 min of recording, the relationship between footprint fluorescence and voltage becomes linear where large increases are seen at hyperpolarized potentials and little change is seen at depolarized potentials. Similar observations were apparent in Jurkat T cells recorded in a similar manner to recordings presented in this thesis (Luik et al., 2006). The hypothesis for the observations in Jurkat T cells was that as the luminal concentration of calcium is depleted, the ER membrane mobilizes toward the plasma membrane where SOC channels form. SOCE through these channels was observed when the driving force for calcium was raised at hyperpolarized membrane potentials. Perhaps, a similar process was observed in chick cochlear hair cells. The synaptic cistern in chick SHCs such as those recorded from in this thesis is a large, flat organelle thought to directly appose the efferent terminal underneath the post-synaptic membrane. SOCE could conceivably be utilized by hair cells to refill a slowly depleting calcium store, possibly reflected by the slow increase in basal footprint fluorescence. The idea that the ER mobilizes toward the plasma membrane and SOC channels take time to develop is consistent with the observation that the non-voltage-gated calcium flux in chick hair cells develops after 1 min of recording. Furthermore, the non-voltage-gated calcium flux develops across the footprint in those cells where the non-voltage-gated calcium flux is initially localized to a smaller region. Although CRAC currents and SOCE have not previously been described in hair cells, it is possible that these activities exist to maintain a homeostatic calcium concentration in the lumen of the synaptic cistern at the efferent synapse.

Alternatively, non-voltage-gated calcium fluxes could reflect the activity of calcium transporters in the plasma membrane. One likely candidate is the NCX, through which calcium flux is normally outward to remove excess calcium from the cytosol. Hyperpolarizing changes in membrane voltage, however, could alter the driving force for sodium such that the normal direction of ion exchange is reversed and calcium influx occurs as a result. NCX activity could also account for the apparent decrease in footprint fluorescence at depolarized membrane potentials. Further experiments are needed to discern whether voltage-sensitive changes in footprint fluorescence are mediated by either SOC channels or reversal of NCX or another mechanism not covered here.

REFERENCES:

Armstrong, C. E., and Roberts, W. M. (1998). Electrical properties of frog saccular hair cells: distortion by enzymatic dissociation. J Neurosci *18*, 2962-2973.

Art, J. J., Crawford, A. C., Fettiplace, R., and Fuchs, P. A. (1985). Efferent modulation of hair cell tuning in the cochlea of the turtle. J Physiol *360*, 397-421.

Art, J. J., and Fettiplace, R. (1987). Variation of membrane properties in hair cells isolated from the turtle cochlea. J Physiol *385*, 207-242.

Art, J. J., Fettiplace, R., and Wu, Y. C. (1993). The effects of low calcium on the voltage-dependent conductances involved in tuning of turtle hair cells. J Physiol *470*, 109-126.

Art, J. J., Wu, Y. C., and Fettiplace, R. (1995). The calcium-activated potassium channels of turtle hair cells. J Gen Physiol *105*, 49-72.

Ashmore, J. F. (1983). Frequency tuning in a frog vestibular organ. Nature *304*, 536-538.

Ashmore, J. F., and Ohmori, H. (1990). Control of intracellular calcium by ATP in isolated outer hair cells of the guinea-pig cochlea. J Physiol *428*, 109-131.

Assad, J. A., and Corey, D. P. (1992). An active motor model for adaptation by vertebrate hair cells. J Neurosci *12*, 3291-3309.

Atkinson, N. S., Robertson, G. A., and Ganetzky, B. (1991). A component of calcium-activated potassium channels encoded by the Drosophila slo locus. Science *253*, 551-555.

Augustine, G. J., Adler, E. M., and Charlton, M. P. (1991). The calcium signal for transmitter secretion from presynaptic nerve terminals. Ann N Y Acad Sci *635*, 365-381.

Axelrod, D. (2001). Selective imaging of surface fluorescence with very high aperture microscope objectives. J Biomed Opt *6*, 6-13.

Berridge, M. J. (1988). Inositol trisphosphate-induced membrane potential oscillations in Xenopus oocytes. J Physiol *403*, 589-599.

Berridge, M. J. (1998). Neuronal calcium signaling. Neuron *21*, 13-26.

Blanchet, C., Erostegui, C., Sugasawa, M., and Dulon, D. (1996). Acetylcholine-induced potassium current of guinea pig outer hair cells: its dependence on a calcium influx through nicotinic-like receptors. J Neurosci *16*, 2574-2584.

Blaustein, M. P., and Lederer, W. J. (1999). Sodium/calcium exchange: its physiological implications. Physiol Rev *79*, 763-854.

Brandt, A., Khimich, D., and Moser, T. (2005). Few CaV1.3 channels regulate the exocytosis of a synaptic vesicle at the hair cell ribbon synapse. J Neurosci *25*, 11577-11585.

Brandt, A., Striessnig, J., and Moser, T. (2003). CaV1.3 channels are essential for development and presynaptic activity of cochlear inner hair cells. J Neurosci *23*, 10832-10840.

Bunt, A. H. (1971). Enzymatic digestion of synaptic ribbons in amphibian retinal photoreceptors. Brain Res *25*, 571-577.

Catterall, W. A. (2000). Structure and regulation of voltage-gated Ca2+ channels. Annu Rev Cell Dev Biol *16*, 521-555.

Chabbert, C. H. (1997). Heterogeneity of hair cells in the bullfrog sacculus. Pflugers Arch *435*, 82-90.

Cheng, H., Lederer, W. J., and Cannell, M. B. (1993). Calcium sparks: elementary events underlying excitation-contraction coupling in heart muscle. Science *262*, 740-744.

Crawford, A. C., and Fettiplace, R. (1980). The frequency selectivity of auditory nerve fibres and hair cells in the cochlea of the turtle. J Physiol *306*, 79-125.

Crawford, A. C., and Fettiplace, R. (1981). An electrical tuning mechanism in turtle cochlear hair cells. J Physiol *312*, 377-412.

Crawford, A. C., and Fettiplace, R. (1983). Auditory nerve responses to imposed displacements of the turtle basilar membrane. Hear Res *12*, 199-208.

Cunningham, C. D., 3rd, Weber, P. C., Spicer, S. S., and Schulte, B. A. (2000). Canalicular reticulum in vestibular hair cells. Hear Res *143*, 69-83.

Dallos, P., Hallworth, R., and Evans, B. N. (1993). Theory of electrically driven shape changes of cochlear outer hair cells. J Neurophysiol *70*, 299-323.

Dallos, P., Zheng, J., and Cheatham, M. A. (2006). Prestin and the cochlear amplifier. J Physiol *576*, 37-42.

DiPolo, R., and Beauge, L. (2006). Sodium/calcium exchanger: influence of metabolic regulation on ion carrier interactions. Physiol Rev *86*, 155-203.

Dulon, D., and Lenoir, M. (1996). Cholinergic responses in developing outer hair cells of the rat cochlea. Eur J Neurosci *8*, 1945-1952.

Edmonds, B. W., Gregory, F. D., and Schweizer, F. E. (2004). Evidence that fast exocytosis can be predominantly mediated by vesicles not docked at active zones in frog saccular hair cells. J Physiol *560*, 439-450.

Eisen, M. D., Spassova, M., and Parsons, T. D. (2004). Large releasable pool of synaptic vesicles in chick cochlear hair cells. J Neurophysiol *91*, 2422-2428.

Elgoyhen, A. B., Johnson, D. S., Boulter, J., Vetter, D. E., and Heinemann, S. (1994). Alpha 9: an acetylcholine receptor with novel pharmacological properties expressed in rat cochlear hair cells. Cell *79*, 705-715.

Elgoyhen, A. B., Vetter, D. E., Katz, E., Rothlin, C. V., Heinemann, S. F., and Boulter, J. (2001). alpha10: a determinant of nicotinic cholinergic receptor function in mammalian vestibular and cochlear mechanosensory hair cells. Proc Natl Acad Sci U S A *98*, 3501-3506.

Eybalin, M. (1993). Neurotransmitters and neuromodulators of the mammalian cochlea. Physiol Rev *73*, 309-373.

Fabiato, A. (1983). Calcium-induced release of calcium from the cardiac sarcoplasmic reticulum. Am J Physiol *245*, C1-14.

Felix, D., and Ehrenberger, K. (1992). The efferent modulation of mammalian inner hair cell afferents. Hear Res *64*, 1-5.

Feske, S., Giltnane, J., Dolmetsch, R., Staudt, L. M., and Rao, A. (2001). Gene regulation mediated by calcium signals in T lymphocytes. Nat Immunol *2*, 316-324.

Fettiplace, R., and Fuchs, P. A. (1999). Mechanisms of hair cell tuning. Annu Rev Physiol *61*, 809-834.

Fischer, F. P. (1992). Quantitative analysis of the innervation of the chicken basilar papilla. Hear Res *61*, 167-178.

Flock, A., and Lam, D. M. (1974). Neurotransmitter synthesis in inner ear and lateral line sense organs. Nature *249*, 142-144.

Fuchs, P. (2002). The synaptic physiology of cochlear hair cells. Audiol Neurootol *7*, 40-44.

Fuchs, P. A., and Evans, M. G. (1990). Potassium currents in hair cells isolated from the cochlea of the chick. J Physiol *429*, 529-551.

Fuchs, P. A., Evans, M. G., and Murrow, B. W. (1990). Calcium currents in hair cells isolated from the cochlea of the chick. J Physiol *429*, 553-568.

Fuchs, P. A., and Murrow, B. W. (1992) a. A novel cholinergic receptor mediates inhibition of chick cochlear hair cells. Proc Biol Sci *248*, 35-40.

Fuchs, P. A., and Murrow, B. W. (1992) b. Cholinergic inhibition of short (outer) hair cells of the chick's cochlea. J Neurosci *12*, 800-809.

Fuchs, P. A., Nagai, T., and Evans, M. G. (1988). Electrical tuning in hair cells isolated from the chick cochlea. J Neurosci *8*, 2460-2467.

Furukawa, T. (1981). Effects of efferent stimulation on the saccule of goldfish. J Physiol *315*, 203-215.

Furukawa, T., Kuno, M., and Matsuura, S. (1982). Quantal analysis of a decremental response at hair cell-afferent fibre synapses in the goldfish sacculus. J Physiol *322*, 181-195.

Glowatzki, E., and Fuchs, P. A. (2000). Cholinergic synaptic inhibition of inner hair cells in the neonatal mammalian cochlea. Science *288*, 2366-2368.

Glowatzki, E., and Fuchs, P. A. (2002). Transmitter release at the hair cell ribbon synapse. Nat Neurosci *5*, 147-154.

Goldberg, J. M., and Fernandez, C. (1980). Efferent vestibular system in the squirrel monkey: anatomical location and influence on afferent activity. J Neurophysiol *43*, 986-1025.

Goodman, M. B., and Art, J. J. (1996). Variations in the ensemble of potassium currents underlying resonance in turtle hair cells. J Physiol *497 (Pt 2)*, 395-412.

Goodno, C. C. (1979). Inhibition of myosin ATPase by vanadate ion. Proc Natl Acad Sci U S A *76*, 2620-2624.

Gray, E. G., and Pease, H. L. (1971). On understanding the organisation of the retinal receptor synapses. Brain Res *35*, 1-15.

Gray, L., and Rubel, E. W. (1985). Development of absolute thresholds in chickens. J Acoust Soc Am *77*, 1162-1172.

Gribenski, A., and Caston, J. (1976). Tonic influence of the efferent vestibular system on the spontaneous afferent activity from semicircular canals in the frog (Rana esculenta L.). Exp Brain Res *26*, 275-283.

Guerini, D., Coletto, L., and Carafoli, E. (2005). Exporting calcium from cells. Cell Calcium *38*, 281-289.

Guinan, J. J., Jr., and Stankovic, K. M. (1996). Medial efferent inhibition produces the largest equivalent attenuations at moderate to high sound levels in cat auditory-nerve fibers. J Acoust Soc Am *100*, 1680-1690.

Guth, P. S., Dunn, A., Kronomer, K., and Norris, C. H. (1994). The cholinergic pharmacology of the frog saccule. Hear Res *75*, 225-232.

Guth, P. S., Perin, P., Norris, C. H., and Valli, P. (1998). The vestibular hair cells: post-transductional signal processing. Prog Neurobiol *54*, 193-247.

Hama, K., and Saito, K. (1977). Fine structure of the afferent synapse of the hair cells in the saccular macula of the goldfish, with special reference to the anastomosing tubules. J Neurocytol *6*, 361-373.

Heidelberger, R., Heinemann, C., Neher, E., and Matthews, G. (1994). Calcium dependence of the rate of exocytosis in a synaptic terminal. Nature *371*, 513-515.

Heuser, J. E., and Reese, T. S. (1981). Structural changes after transmitter release at the frog neuromuscular junction. J Cell Biol *88*, 564-580.

Hilgemann, D. W., Nicoll, D. A., and Philipson, K. D. (1991). Charge movement during Na+ translocation by native and cloned cardiac Na+/Ca2+ exchanger. Nature *352*, 715-718.

Hillman, D. E. (1969). Light and electron microscopical study of the relationships between the cerebellum and the vestibular organ of the frog. Exp Brain Res *9*, 1-15.

Hillman DE. Morphology of peripheral and central vestibular systems. In: Llinas, R and Precht, W. editors. Frog Neurobiology. Berlin: Springer-Verlag; 1976. p. 452-79

Hirokawa, N. (1978). The ultrastructure of the basilar papilla of the chick. J Comp Neurol *181*, 361-374.

Holt, J. C., Lioudyno, M., Athas, G., Garcia, M. M., Perin, P., and Guth, P. S. (2001) The effect of proteolytic enzymes on the alpha9-nicotinic receptor-mediated response in isolated frog vestibular hair cells. Hear Res *152*, 25-42.

Hudspeth, A. (1997). Mechanical amplification of stimuli by hair cells. Curr Opin Neurobiol *7*, 480-486.

Hudspeth, A. J. (1989). How the ear's works work. Nature *341*, 397-404.

Hudspeth, A. J. (1997). How hearing happens. Neuron *19*, 947-950.

Hudspeth, A. J., and Issa, N. P. (1996). Confocal-microscopic visualization of membrane addition during synaptic exocytosis at presynaptic active zones of hair cells. Cold Spring Harb Symp Quant Biol *61*, 303-307.

Ikeda, K., Saito, Y., Nishiyama, A., and Takasaka, T. (1992). Na(+)-Ca2+ exchange in the isolated cochlear outer hair cells of the guinea-pig studied by fluorescence image microscopy. Pflugers Arch *420*, 493-499.

Issa, N. P., and Hudspeth, A. J. (1994). Clustering of Ca2+ channels and Ca(2+)-activated K+ channels at fluorescently labeled presynaptic active zones of hair cells. Proc Natl Acad Sci U S A *91*, 7578-7582.

Issa, N. P., and Hudspeth, A. J. (1996). Characterization of fluo-3 labelling of dense bodies at the hair cell's presynaptic active zone. J Neurocytol *25*, 257-266.

Issa, N. P., and Hudspeth, A. J. (1996). The entry and clearance of Ca2+ at individual presynaptic active zones of hair cells from the bullfrog's sacculus. Proc Natl Acad Sci U S A *93*, 9527-9532.

Jacobs, R. A., and Hudspeth, A. J. (1990). Ultrastructural correlates of mechanoelectrical transduction in hair cells of the bullfrog's internal ear. Cold Spring Harb Symp Quant Biol *55*, 547-561.

Jiang, G. J., Zidanic, M., Michaels, R. L., Michael, T. H., Griguer, C., and Fuchs, P. A. (1997). CSlo encodes calcium-activated potassium channels in the chick's cochlea. Proc Biol Sci *264*, 731-737.

Jones, E. M., Gray-Keller, M., and Fettiplace, R. (1999). The role of Ca2+-activated K+ channel spliced variants in the tonotopic organization of the turtle cochlea. J Physiol *518 (Pt 3)*, 653-665.

Jones, E. M., Laus, C., and Fettiplace, R. (1998). Identification of Ca(2+)-activated K+ channel splice variants and their distribution in the turtle cochlea. Proc Biol Sci *265*, 685-692.

Katz, E., Elgoyhen, A. B., Gomez-Casati, M. E., Knipper, M., Vetter, D. E., Fuchs, P. A., and Glowatzki, E. (2004). Developmental regulation of nicotinic synapses on cochlear inner hair cells. J Neurosci *24*, 7814-7820.

Keen, E. C., and Hudspeth, A. J. (2006). Transfer characteristics of the hair cell's afferent synapse. Proc Natl Acad Sci U S A *103*, 5537-5542.

Kennedy, H. J. (2002). Intracellular calcium regulation in inner hair cells from neonatal mice. Cell Calcium *31*, 127-136.

Kennedy, H. J., and Meech, R. W. (2002). Fast Ca2+ signals at mouse inner hair cell synapse: a role for Ca2+-induced Ca2+ release. J Physiol *539*, 15-23.

Khimich, D., Nouvian, R., Pujol, R., Tom Dieck, S., Egner, A., Gundelfinger, E. D., and Moser, T. (2005). Hair cell synaptic ribbons are essential for synchronous auditory signalling. Nature *434*, 889-894.

Kollmar, R., Montgomery, L. G., Fak, J., Henry, L. J., and Hudspeth, A. J. (1997). Predominance of the alpha1D subunit in L-type voltage-gated Ca2+ channels of hair cells in the chicken's cochlea. Proc Natl Acad Sci U S A *94*, 14883-14888.

Koyama, H., Lewis, E. R., Leverenz, E. L., and Baird, R. A. (1982). Acute seismic sensitivity in the bullfrog ear. Brain Res *250*, 168-172.

Kros, C. J., and Crawford, A. C. (1990). Potassium currents in inner hair cells isolated from the guinea-pig cochlea. J Physiol *421*, 263-291.

Lagnado, L., Gomis, A., and Job, C. (1996). Continuous vesicle cycling in the synaptic terminal of retinal bipolar cells. Neuron *17*, 957-967.

Leake, P. A., and Snyder, R. L. (1987). Uptake of horseradish peroxidase from perilymph by cochlear hair cells. Hear Res *25*, 153-171.

Lenzi, D., Crum, J., Ellisman, M. H., and Roberts, W. M. (2002). Depolarization redistributes synaptic membrane and creates a gradient of vesicles on the synaptic body at a ribbon synapse. Neuron *36*, 649-659.

Lenzi, D., and Roberts, W. M. (1994). Calcium signalling in hair cells: multiple roles in a compact cell. Curr Opin Neurobiol *4*, 496-502.

Lenzi, D., Runyeon, J. W., Crum, J., Ellisman, M. H., and Roberts, W. M. (1999). Synaptic vesicle populations in saccular hair cells reconstructed by electron tomography. J Neurosci *19*, 119-132.

Lenzi, D., and von Gersdorff, H. (2001). Structure suggests function: the case for synaptic ribbons as exocytotic nanomachines. Bioessays *23*, 831-840.

Lewis, E. R., Baird, R. A., Leverenz, E. L., and Koyama, H. (1982). Inner ear: dye injection reveals peripheral origins of specific sensitivities. Science *215*, 1641-1643.

Lewis E. R., Leverenz E. L., Bialek W. S. The vertebrate inner ear. Boca Raton (FL): CRC Press, Inc.; 1985.

Lewis, R. S. (2001). Calcium signaling mechanisms in T lymphocytes. Annu Rev Immunol *19*, 497-521.

Lewis, R. S., and Hudspeth, A. J. (1983). Voltage- and ion-dependent conductances in solitary vertebrate hair cells. Nature *304*, 538-541.

Lioudyno, M., Hiel, H., Kong, J. H., Katz, E., Waldman, E., Parameshwaran-Iyer, S., Glowatzki, E., and Fuchs, P. A. (2004). A "synaptoplasmic cistern" mediates rapid inhibition of cochlear hair cells. J Neurosci *24*, 11160-11164.

Llinas, R., and Precht, W. (1969). The inhibitory vestibular efferent system and its relation to the cerebellum in the frog. Exp Brain Res *9*, 16-29.

Luik, R. M., Wu, M. M., Buchanan, J., and Lewis, R. S. (2006). The elementary unit of store-operated Ca2+ entry: local activation of CRAC channels by STIM1 at ER-plasma membrane junctions. J Cell Biol *174*, 815-825.

Manley, G. A., Brix, J., and Kaiser, A. (1987). Developmental stability of the tonotopic organization of the chick's basilar papilla. Science *237*, 655-656.

Manley, G. A., Gleich, O., Kaiser, A. and Brix, J. (1989) Functional differentiation of sensory cells in the avian auditory periphery. J Comp Physiol A *164*, 289-296.

Manley, G. A., Meyer, B., Fischer, F. P., Schwabedissen, G., and Gleich, O. (1996). Surface morphology of basilar papilla of the tufted duck Aythya fuligula, and domestic chicken Gallus gallus domesticus. J Morphol *227*, 197-212.

Marcotti, W., Johnson, S. L., and Kros, C. J. (2004). Effects of intracellular stores and extracellular Ca(2+) on Ca(2+)-activated K(+) currents in mature mouse inner hair cells. J Physiol *557*, 613-633

Martin, A. R., and Fuchs, P. A. (1992). The dependence of calcium-activated potassium currents on membrane potential. Proc Biol Sci *250*, 71-76.

Martin, P., Bozovic, D., Choe, Y., and Hudspeth, A. J. (2003). Spontaneous oscillation by hair bundles of the bullfrog's sacculus. J Neurosci *23*, 4533-4548.

Martinez-Dunst, C., Michaels, R. L., and Fuchs, P. A. (1997). Release sites and calcium channels in hair cells of the chick's cochlea. J Neurosci *17*, 9133-9144.

Mathers, D. A., and Barker, J. L. (1981). Spontaneous hyperpolarizations at the membrane of cultured mouse dorsal root ganglion cells. Brain Res *211*, 451-455.

Mennerick, S., and Matthews, G. (1996). Ultrafast exocytosis elicited by calcium current in synaptic terminals of retinal bipolar neurons. Neuron *17*, 1241-1249.

Montero, M., Alonso, M. T., Carnicero, E., Cuchillo-Ibanez, I., Albillos, A., Garcia, A. G., Garcia-Sancho, J., and Alvarez, J. (2000). Chromaffin-cell stimulation triggers fast millimolar mitochondrial Ca2+ transients that modulate secretion. Nat Cell Biol *2*, 57-61.

Moser, T., and Beutner, D. (2000). Kinetics of exocytosis and endocytosis at the cochlear inner hair cell afferent synapse of the mouse. Proc Natl Acad Sci U S A *97*, 883-888.

Muresan, V., Lyass, A., and Schnapp, B. J. (1999). The kinesin motor KIF3A is a component of the presynaptic ribbon in vertebrate photoreceptors. J Neurosci *19*, 1027-1037.

Navaratnam, D. S., Bell, T. J., Tu, T. D., Cohen, E. L., and Oberholtzer, J. C. (1997). Differential distribution of Ca2+-activated K+ channel splice variants among hair cells along the tonotopic axis of the chick cochlea. Neuron *19*, 1077-1085.

Neher, E., and Marty, A. (1982). Discrete changes of cell membrane capacitance observed under conditions of enhanced secretion in bovine adrenal chromaffin cells. Proc Natl Acad Sci U S A *79*, 6712-6716.

Nelson, M. T., Cheng, H., Rubart, M., Santana, L. F., Bonev, A. D., Knot, H. J., and Lederer, W. J. (1995). Relaxation of arterial smooth muscle by calcium sparks. Science *270*, 633-637.

Nowycky, M. C., Fox, A. P., and Tsien, R. W. (1985). Three types of neuronal calcium channel with different calcium agonist sensitivity. Nature *316*, 440-443.

Ohtani, M., Devau, G., Lehouelleur, J., and Sans, A. (1994). Cholinergic agonists increase intracellular calcium concentration in frog vestibular hair cells. Hear Res *80*, 167-173.

Paillart, C., Li, J., Matthews, G., and Sterling, P. (2003). Endocytosis and vesicle recycling at a ribbon synapse. J Neurosci *23*, 4092-4099.
Parekh, A. B. (2006). Cell biology: cracking the calcium entry code. Nature *441*, 163-165.

Parekh, A. B., and Putney, J. W., Jr. (2005). Store-operated calcium channels. Physiol Rev *85*, 757-810.

Parsons, T. D., Lenzi, D., Almers, W., and Roberts, W. M. (1994). Calcium-triggered exocytosis and endocytosis in an isolated presynaptic cell: capacitance measurements in saccular hair cells. Neuron *13*, 875-883.

Plazas, P. V., Katz, E., Gomez-Casati, M. E., Bouzat, C., and Elgoyhen, A. B. (2005). Stoichiometry of the alpha9alpha10 nicotinic cholinergic receptor. J Neurosci *25*, 10905-10912.

Prakriya, M., Feske, S., Gwack, Y., Srikanth, S., Rao, A., and Hogan, P. G. (2006). Orai1 is an essential pore subunit of the CRAC channel. Nature *443*, 230-233.

Precht, W., Richter, A., Ozawa, S., and Shimazu, H. (1974). Intracellular study of frog's vestibular neurons in relation to the labyrinth and spinal cord. Exp Brain Res *19*, 377-393.

Purves D., Augustine G. J., Fitzpatrick D., Katz L. C., LaMantia A-S., McNamara J. O., Williams S.M., editors. Neuroscience. 2nd ed. Sunderland (MA): Sinauer Associates, Inc.; c2001.

Putney, J. W., Jr. (1986). A model for receptor-regulated calcium entry. Cell Calcium *7*, 1-12.

Rajan, R. (2001). Cochlear outer-hair-cell efferents and complex-sound-induced hearing loss: protective and opposing effects. J Neurophysiol *86*, 3073-3076.

Ramanathan, K., Michael, T. H., Jiang, G. J., Hiel, H., and Fuchs, P. A. (1999). A molecular mechanism for electrical tuning of cochlear hair cells. Science *283*, 215-217.

Rebillard, M., and Pujol, R. (1983). Innervation of the chicken basilar papilla during its development. Acta Otolaryngol *96*, 379-388.

Reiter, E. R., and Liberman, M. C. (1995). Efferent-mediated protection from acoustic overexposure: relation to slow effects of olivocochlear stimulation. J Neurophysiol *73*, 506-514.

Roberts, W. M. (1993). Spatial calcium buffering in saccular hair cells. Nature *363*, 74-76.

Roberts, W. M., Jacobs, R. A., and Hudspeth, A. J. (1990). Colocalization of ion channels involved in frequency selectivity and synaptic transmission at presynaptic active zones of hair cells. J Neurosci *10*, 3664-3684.

Roberts, W. M., Jacobs, R. A., and Hudspeth, A. J. (1991). The hair cell as a presynaptic terminal. Ann N Y Acad Sci *635*, 221-233.

Rodriguez-Contreras, A., and Yamoah, E. N. (2001). Direct measurement of single-channel Ca(2+) currents in bullfrog hair cells reveals two distinct channel subtypes. J Physiol *534*, 669-689.

Roos, J., DiGregorio, P. J., Yeromin, A. V., Ohlsen, K., Lioudyno, M., Zhang, S., Safrina, O., Kozak, J. A., Wagner, S. L., Cahalan, M. D., *et al.* (2005). STIM1, an essential and conserved component of store-operated Ca2+ channel function. J Cell Biol *169*, 435-445.

Rose, C. R., and Konnerth, A. (2001). Stores not just for storage. intracellular calcium release and synaptic plasticity. Neuron *31*, 519-522.

Rosenblatt, K. P., Sun, Z. P., Heller, S., and Hudspeth, A. J. (1997). Distribution of Ca2+-activated K+ channel isoforms along the tonotopic gradient of the chicken's cochlea. Neuron *19*, 1061-1075.

Ross, M. D. (1997). Morphological evidence for local microcircuits in rat vestibular maculae. J Comp Neurol *379*, 333-346.

Rossi, M. L., and Martini, M. (1988). The effect of barium and some channel blockers on sensory discharge of the frog labyrinth posterior canal recorded at rest and during rotation. Brain Res *452*, 312-322.

Rothlin, C. V., Katz, E., Verbitsky, M., and Elgoyhen, A. B. (1999). The alpha9 nicotinic acetylcholine receptor shares pharmacological properties with type A gamma-aminobutyric acid, glycine, and type 3 serotonin receptors. Mol Pharmacol *55*, 248-254.

Rutherford, M. A., and Roberts, W. M. (2006). Frequency selectivity of synaptic exocytosis in frog saccular hair cells. Proc Natl Acad Sci U S A *103*, 2898-2903.

Samaranayake, H., Saunders, J. C., Greene, M. I., and Navaratnam, D. S. (2004). Ca(2+) and K(+) (BK) channels in chick hair cells are clustered and colocalized with apical-basal and tonotopic gradients. J Physiol *560*, 13-20.

Schmitz, F., Konigstorfer, A., and Sudhof, T. C. (2000). RIBEYE, a component of synaptic ribbons: a protein's journey through evolution provides insight into synaptic ribbon function. Neuron *28*, 857-872.

Schulte, B. A. (1993). Immunohistochemical localization of intracellular Ca-ATPase in outer hair cells, neurons and fibrocytes in the adult and developing inner ear. Hear Res *65*, 262-273.

Shigemoto, T., and Ohmori, H. (1990). Muscarinic agonists and ATP increase the intracellular Ca2+ concentration in chick cochlear hair cells. J Physiol *420*, 127-148.

Shigemoto, T., and Ohmori, H. (1991). Muscarinic receptor hyperpolarizes cochlear hair cells of chick by activating Ca(2+)-activated K+ channels. J Physiol *442*, 669-690.

Smith, C. A. (1961). Innervation pattern of the cochlea. The internal hair cell. Trans Am Otol Soc *49*, 35-60.

Smith, C. A. (1968)a. Electron microscopy of the inner ear. Ann Otol Rhinol Laryngol *77*, 629-643.

Smith, C. A. (1968)b. Ultrastructure of the organ of Corti. Adv Sci *24*, 419-433.

Smith, G. L., Valdeolmillos, M., Eisner, D. A., and Allen, D. G. (1988). Effects of rapid application of caffeine on intracellular calcium concentration in ferret papillary muscles. J Gen Physiol *92*, 351-368.

Spicer, S. S., Thomopoulos, G. N., and Schulte, B. A. (1999). Novel membranous structures in apical and basal compartments of inner hair cells. J Comp Neurol *409*, 424-437.

Spoendlin, H. (1972). Innervation densities of the cochlea. Acta Otolaryngol *73*, 235-248.

Sridhar, T. S., Brown, M. C., and Sewell, W. F. (1997). Unique postsynaptic signaling at the hair cell efferent synapse permits calcium to evoke changes on two time scales. J Neurosci *17*, 428-437.

Steinacker, A., and Rojas, L. (1988). Acetylcholine modulated potassium channel in the hair cell of the toadfish saccule. Hear Res *35*, 265-269.

Steyer, J. A., and Almers, W. (2001). A real-time view of life within 100 nm of the plasma membrane. Nat Rev Mol Cell Biol *2*, 268-275.

Su, Z. L., Jiang, S. C., Gu, R., and Yang, W. P. (1995). Two types of calcium channels in bullfrog saccular hair cells. Hear Res *87*, 62-68.

Sugai, T., Yano, J., Sugitani, M., and Ooyama, H. (1992). Actions of cholinergic agonists and antagonists on the efferent synapse in the frog sacculus. Hear Res *61*, 56-64.

Sugihara, I. (2001). Efferent innervation in the goldfish saccule examined by acetylcholinesterase histochemistry. Hear Res *153*, 91-99.

Sugihara, I., and Furukawa, T. (1989). Morphological and functional aspects of two different types of hair cells in the goldfish sacculus. J Neurophysiol *62*, 1330-1343.

Takasaka, T., and Smith, C. A. (1971). The structure and innervation of the pigeon's basilar papilla. J Ultrastruct Res *35*, 20-65.

Tanaka, K., and Smith, C. A. (1978). Structure of the chicken's inner ear: SEM and TEM study. Am J Anat *153*, 251-271.

tom Dieck, S., Altrock, W. D., Kessels, M. M., Qualmann, B., Regus, H., Brauner, D., Fejtova, A., Bracko, O., Gundelfinger, E. D., and Brandstatter, J. H. (2005). Molecular dissection of the photoreceptor ribbon synapse: physical interaction of Bassoon and RIBEYE is essential for the assembly of the ribbon complex. J Cell Biol *168*, 825-836.

Tomchik, S. M., and Lu, Z. (2006). Modulation of auditory signal-to-noise ratios by efferent stimulation. J Neurophysiol *95*, 3562-3570.

Tsien, R. W., and Tsien, R. Y. (1990). Calcium channels, stores, and oscillations. Annu Rev Cell Biol *6*, 715-760.

Tsugorka, A., Rios, E., and Blatter, L. A. (1995). Imaging elementary events of calcium release in skeletal muscle cells. Science *269*, 1723-1726.

Tucker, T., Art, J. J., and Fettiplace, R. (1996). Routes of calcium entry and extrusion in turtle hair cells. Ann N Y Acad Sci *781*, 123-137.

Tucker, T., and Fettiplace, R. (1995). Confocal imaging of calcium microdomains and calcium extrusion in turtle hair cells. Neuron *15*, 1323-1335.

Tucker, T. R., and Fettiplace, R. (1996). Monitoring calcium in turtle hair cells with a calcium-activated potassium channel. J Physiol *494 (Pt 3)*, 613-626.

Uziel, A., Romand, R., and Marot, M. (1981). Development of cochlear potentials in rats. Audiology *20*, 89-100.

Valli, P., Botta, L., Zucca, G., and Casella, C. (1986). Functional organization of the peripheral efferent vestibular system in the frog. Brain Res *362*, 92-97.

Verbitsky, M., Rothlin, C. V., Katz, E., and Elgoyhen, A. B. (2000). Mixed nicotinic-muscarinic properties of the alpha9 nicotinic cholinergic receptor. Neuropharmacology *39*, 2515-2524.

Vergara, C., Latorre, R., Marrion, N. V., and Adelman, J. P. (1998). Calcium-activated potassium channels. Curr Opin Neurobiol *8*, 321-329.

von Bekesy, G. Experiments in Hearing, McGraw-Hill, NY; 1960.

von Gersdorff, H., and Matthews, G. (1994). Dynamics of synaptic vesicle fusion and membrane retrieval in synaptic terminals. Nature *367*, 735-739.

von Gersdorff, H., Vardi, E., Matthews, G., and Sterling, P. (1996). Evidence that vesicles on the synaptic ribbon of retinal bipolar neurons can be rapidly released. Neuron *16*, 1221-1227.

Warr, W. B. (1975). Olivocochlear and vestibular efferent neurons of the feline brain stem: their location, morphology and number determined by retrograde axonal transport and acetylcholinesterase histochemistry. J Comp Neurol *161*, 159-181.

Wiederhold, M. L. (1970). Variations in the effects of electric stimulation of the crossed olivocochlear bundle on cat single auditory-nerve-fiber responses to tone bursts. J Acoust Soc Am *48*, 966-977.

Wu, Y. C., Tucker, T., and Fettiplace, R. (1996). A theoretical study of calcium microdomains in turtle hair cells. Biophys J *71*, 2256-2275.

Yamashita, T., Ohnishi, S., Ohtani, M., and Kumazawa, T. (1993). Effects of efferent neurotransmitters on intracellular Ca2+ concentration in vestibular hair cells of the guinea pig. Acta Otolaryngol Suppl *500*, 26-30.

Yoshida, N., Shigemoto, T., Sugai, T., and Ohmori, H. (1994). The role of inositol trisphosphate on ACh-induced outward currents in bullfrog saccular hair cells. Brain Res *644*, 90-100.

Zenisek, D., Davila, V., Wan, L., and Almers, W. (2003). Imaging calcium entry sites and ribbon structures in two presynaptic cells. J Neurosci *23*, 2538-2548.

Zenisek, D., Steyer, J. A., and Almers, W. (2000). Transport, capture and exocytosis of single synaptic vesicles at active zones. Nature *406*, 849-854.

Zenisek, D., Steyer, J. A., Feldman, M. E., and Almers, W. (2002). A membrane marker leaves synaptic vesicles in milliseconds after exocytosis in retinal bipolar cells. Neuron *35*, 1085-1097.

Zidanic, M. (2002). Cholinergic innervation of the chick basilar papilla. J Comp Neurol *445*, 159-175.

Zidanic, M., and Fuchs, P. A. (1995). Kinetic analysis of barium currents in chick cochlear hair cells. Biophys J *68*, 1323-1336.

MATERIALS AND METHODS

All methods for animal handling were approved by the Institutional Animal Care and Use Committee (IACUC) at Oregon Health & Science University. All chemicals were acquired from Sigma, St. Louis, MO unless otherwise indicated.

Hair cell preparation:

Bullfrog:

Bullfrogs (*Rana catesbeiana*) 3 to 4 inches were obtained from West Jersey Bio, Ted Niles or Rana Ranch, chilled in ice water, pithed and decapitated. Hair cells were isolated from the sacculi as described previously (Assad and Corey, 1992). Briefly, inner ears were removed into low calcium solution (LCS) containing (in mM): 110 NaCl, 2 KCl, 2 $MgCl_2 \cdot 6\ H_2O$, 3 D-glucose, 10 HEPES, and 0.1 $CaCl_2$. A small tear in the membrane above the sacculus was made, and tight junctions were disrupted with 15 min incubation at room temperature (RT) in 1 mM EGTA in LCS. The saccular macula was then excised in LCS and otoconia were removed. For FM1-43 labeling experiments, isolated sacculi were then placed in papain solution (~30 U/ml papain - Fluka BioChemika, Ronkonkoma, NY) in double-distilled water containing 8.3 mM L-cysteine for 5 min at room temperature. For experiments testing ACh-induced currents, isolated sacculi were then placed in 50 μg/ml subtilisin (protease type XXIV) in LCS and incubated for 20 min at RT. For experiments looking at voltage-sensitive calcium noise, isolated sacculi were either treated as those used for ACh experiments with subtilisin or were placed in 0.5 mg/ml thermolysin at room temperature for 20 min. Enzyme-treated sacculi were then transferred to deoxyribonucleic acid I (DNase I) solution (2 mg/ml LCS) for removal of otolithic membranes to expose hair cells. Cells were teased with an eyelash into a 60 µl droplet of LCS on either a high-refractive (afferent synapse) or low-refractive (efferent synapse, calcium noise and non-voltage-gated calcium flux) index coverslip coated with concanavalin A (1 mg/ml LCS). After allowing several minutes for hair cells to settle, isolated cells were superfused with bath solution (Parsons et al., 1994) containing (in mM): 110 NaCl, 4 $CaCl_2$, 2 KOH, 5 HEPES, and 3 D-glucose.

Chicken:

Fertile eggs (SPAFAS SPF) were obtained from Charles River Laboratories, Inc. and set in a humidified incubator at 37.5 °C and kept for either 18 to 21 days before hatch for embryonic hair cell isolation, or, were hatched and kept in an IACUC maintained facility up to two weeks for hair cell isolation from chickens. Embryos or hatchlings were first decapitated and heads were cut down the midline into two halves and buried in ice. For cochlea isolation, with the flat side of one half-head down (medial side), a cut was made halfway across the ear opening towards the back of the head tangential to the eardrum. The columella was removed and surrounding tissue and bones were removed to expose the cochlea. The cochlea was then removed by picking up the basal end with blunt forceps and then placed into oxygenated standard chicken saline containing (in mM): 154 NaCl, 6 KCl, 2.3 $MgCl_2 \cdot 6\ H_2O$, 5.6mM $CaCl_2 \cdot 2H_2O$, 5 HEPES and 8 D-glucose, pH 7.35-7.4, ~332-341 mOsm. Cochleas were transferred to 0.1 mg/ml protease solution in 0.5 mg/ml bovine serum albumin (BSA) in oxygenated standard chicken saline for 5 min at RT. Cochleas were then transferred to 0.5 mg/ml BSA in saline for <1 min and then transferred again to standard chicken saline to remove the tegmentum vasculosum and otoconia. Cochleas were transferred and pinned onto a Sylgard-filled dish at the base and apex for removal of the tectorial membrane leaving the apical ends of the hair cells exposed. A recording pipette with a slightly cracked tip was attached to tubing and used to aspirate the short hair cells in the region most likely to receive a predominantly efferent input. Cells were then gently blown out onto a concanavalin A (1 mg/ml in standard chicken saline) coated glass coverslip (22 mm diameter, 1.45 refractive index, Assistant, Germany). The 1.45 refractive index glass coverslips were first cleaned by sonication in 70 % ethanol (EtOH) in dH_2O for 5 min then rinsed 3 times in 100 % EtOH and then finally flame-dried and stored until use. Low refractive index coverslips were used only once for recordings and then discarded unlike the high refractive index coverslips used in most experiments with bullfrog saccular hair cells which were cleaned and reused several times for experiments. After allowing ~10 min for cells to settle, the well was gently filled with ~500 μl oxygenated saline using a 1 ml syringe (melted and pulled to a ~1 mm diameter tip) and allowed to further settle for ~15-20 min. This method helped increase the likelihood that hair cells adhered to the glass basal end (efferent synapse) down would remain adhered following perfusion of the well with a constant flow (1-2 ml/min) of oxygenated standard chicken saline.

Electrophysiology

Recording solutions:

For electrical recordings, the pipette solution for bullfrog saccular hair cells, adapted from Parsons et al. (1994), contained (in mM): 107.5 CsOH, 106 aspartate, 5 HEPES, 2 $MgCl_2$, 0.078 $CaCl_2$, 1 EGTA, and CsOH to bring pH to ~7.4. Additional ingredients were added freshly before use (in mM): 10 EGTA, 10 TEA-Cl, 1.8 Na_2ATP, and a 0.2 mM concentration of the calcium indicator Fluo-3 pentaammonium salt or Fluo-4 pentapotassium salt (Molecular Probes, Eugene, OR). The osmolarity was adjusted to 240-250 mOsm. The external recording solution, adapted from Parsons et al. (1994), for bullfrog saccular hair cells was composed of (in mM): 110 NaCl, 0, 4 or 17 $CaCl_2$, 2 KOH, 5 HEPES, 3 D-glucose, and NaOH to bring pH to ~7.4.

Some experiments looking at the effects of acetylcholine required the use of K^+ instead of Cs^+ in the internal solution without the addition of TEA-Cl. Experiments looking at the effect of voltage on calcium noise were filled with either a K^+ or Cs^+ based internal solution with or without 1 mM TEA.

The standard pipette solution for chicken cochlear hair cells, adapted from a protocol kindly provided by Fuchs, PA, contained (in mM): 112 KCl, 2 $MgCl_2$, 1.5 $CaCl_2$, 10 HEPES, 11 EGTA or no EGTA, 5 Na_2ATP and 0.3 NaGTP, pH 7.24, 302 mOsm. Some experiments substituted EGTA with either 1 or 10 BAPTA. Additional KOH and KCl was added to bring pH to 7.35-7.4 and the osmolarity to 298-300, respectively. The final $[K^+]_i$ ranged from 149 to 173 mM. On the day of recording, 200 μM of either Fluo-3 pentaammonium or Fluo-4 pentapotassium or Fluo-4FF pentapotassium salt (Molecular Probes) was added to the pipette solution. Standard chicken saline was used in the bath during recordings (see Hair Cell Preparation above).

Isolated hair cells were voltage-clamped using an EPC-9 amplifier with Pulse acquisition software.

Solution changes or pharmacological agent application

General or local perfusion:

Experimental solutions or certain pharmacological agents were applied either by slow perfusion in the general bath of the whole well or applied directly onto individual cells either by microperfusion with positive pressure using a patch electrode or by ionophoresis. Experimental solutions or pharmacological agents were sometimes applied in the general bath flow. Local application of pharmacological agents onto single cells were applied by microperfusion through either a 100 μm tip or a patch pipette (3-5 MΩ) and released by the opening of an electromagnetic valve with a TTL pulse and 3-5 psi N_2 gas pressure. Application of 1 M ACh in dH_2O by ionophoresis was done with a +100 nA release current from a 2-3 nA backing current through a ~100 MΩ pipette tip placed ~1-2 μm from the cell surface. Ionophoresis was tested with 1 M $CaCl_2$ in dH_2O in the pipette and 200 μM Fluo4 pentapotassium salt in saline.

Fluorescence imaging and data acquisition

TIRF field setup and camera:

Cells were viewed through an inverted microscope (Axiovert 135; Zeiss, Oberkochen, Germany) and modified for through-the-lens evanescent field illumination (Axelrod, 2001; Steyer and Almers, 2001) as described previously (Zenisek et al., 2002). A 488 nm wavelength beam from either an argon or krypton-argon laser (both Coherent Inc., Santa Clara, CA) was applied either by opening and closing a shutter or activation of an acoustic optical tunable filter (AOTF) with a TTL pulse. The expanded beam was focused off-axis onto the back focal plane of either a 1.65 NA objective (Apo ×100 O HR; Olympus Optical, Tokyo, Japan) or a 1.45 NA objective (100X oil αPlan-FLUAR

Zeiss, Germany). It underwent total internal reflection at the interface between the coverglass and the cell and generated in the cell an evanescent field declining exponentially with distance from the interface depending on the angle the beam strikes the interface. For experiments using the bullfrog saccular hair cell preparation, an angle of 54° was used as measured with a hemicylinder (Zenisek et al., 2002). With this angle and the higher refractive index coverglass, oil and objective, the evanescent field is predicted to decline *e*-fold within 78.2 nm of the interface. For all chicken embryo and some hatchling hair cell preparations, a 1.5X refractive index coverglass (Assistent (Hecht) 22 mm diameter, 0.17 +/- 0.01 mm thickness, Germany), oil and 1.45 NA objective was used with an angle that resulted in an effective evanescent field of 112 nm. For experiments using the bullfrog saccular and embryonic chicken cochlear hair cell preparation and some chicken hatchling (p0-p1) preparations, images were acquired with a fiber-coupled intensified frame-transfer CCD camera (I-Pentamax; Roper Scientific, Tucson, AZ) and a 2.5X optivar resulting in 250X magnification with a pixel size of 104 nm^2. The pixel size for bullfrog saccular hair cell images shown in Fig. 50 was 161 nm^2. For experiments using chicken hatchling (p0-p14) preparations, a Cascade camera was used. The pixel size for chick cochlear hair cell images represented in this chapter is 96 nm^2, except for the chick cochlear hair cell in Figs. 54 and 55 (67 nm^2). All images were acquired at frame rates between 20 and 50 Hz and analyzed using Metamorph software (Universal Imaging Corporation, West Chester, PA).

FM1-43 labeling:

After bullfrog saccular hair cells had adhered to the high refractive index glass, the isolated cells were superfused with bath saline containing 12 mM external calcium. Two pipettes were placed opposite each other towards the basal portion of a selected cell. One was an FM dye-loading pipette filled with 5 μM FM1-43 in high potassium saline (in mM: 42 NaCl, 4 $CaCl_2$, 2 KOH, 68 KCl, 5 HEPES, pH to 7.42 with NaOH, 228 mOsm). The tip of the FM dye-loading pipette was pulled like a standard recording pipette and the tip was fire-polished to a small diameter before filling to limit leakage of the dye; this pipette was placed ~2-3 μm from the cell surface. The second pipette was filled with bath solution with no added calcium and had a tip diameter of ~3-4 μm; this pipette was placed ~5-7 μm from the cell on the opposite side and was used to blow away dye solution with gentle pressure before and after dye application. To stimulate FM1-43 uptake, the calcium free solution was turned off and the FM dye-loading solution was applied with positive pressure for ~15 sec without general bath perfusion. To stop FM dye labeling, the flow of calcium-free solution in the opposite pipette was resumed to blow away the dye solution for some amount of time, the FM dye-loading pipette was raised up and the general bath solution was turned on again. Image streams of dye release events from the two cells presented here were taken while the calcium-free solution was flowing over the cell possibly within 30 minutes of dye loading.

Electron microscopy

Bullfrog sacculus was excised as above and incubated in 1mM EGTA in LCS for 15 min at RT to disrupt tight junctions and aid in the permeation of fixative. Surrounding tissue to the region of hair cells was then further trimmed in the EGTA solution to aid in sectioning. Trimmed sacculus was then transferred to 500 μL fixative comprised of 1 mM EGTA in LCS saline made up with 4 % EM grade paraformaldehyde (Electron Microscopy Sciences, Hatfield, PA) in dH_2O plus a few grains of potassium ferricyanide ($K_3Fe(Cn)_6$) to stain organelle membrane. Fixation was carried out in the dark for 1 hour at RT and then at 4 °C overnight. Fixed sacculus was then rinsed in 0.2 M sodium cacodylate buffer for 15 min at RT then post-fixed in osmium tetroxide for 1 hour at RT then rinsed once in water for 5 min at RT. Post-fixed sacculus was then stained with 4% uranyl acetate for 30 min at RT then rinsed three times in water for 5 min each at RT. Stained sacculus was then dehydrated in a graded series of acetone concentrations, (50, 70, 95, 100 %), for 15 min at RT each concentration. Dehydrated sacculus was then embedded in 50/50 acetone/EPON 812 by slow rotation overnight at RT. Embedded sacculus was then transferred to straight EPON 812 in mold and cured at 60 °C overnight. Cured samples were then epoxied onto blanks for sectioning. The sacculus was oriented in the mold in such a way that sections would be carried out perpendicular to the surface of the sacculus allowing for vertical cross-sections of hair cells for visualization of the afferent and efferent synapses. Sections were obtained at a thickness of 80-100 nm using either a glass or diamond blade and placed on either nickel or gold grids and further processed with uranyl acetate for 30 min at RT in the dark, rinsed four times in dH_2O, then followed by incubation in lead citrate for 10 min and rinsed four times in dH_2O before imaging on the electron microscope.

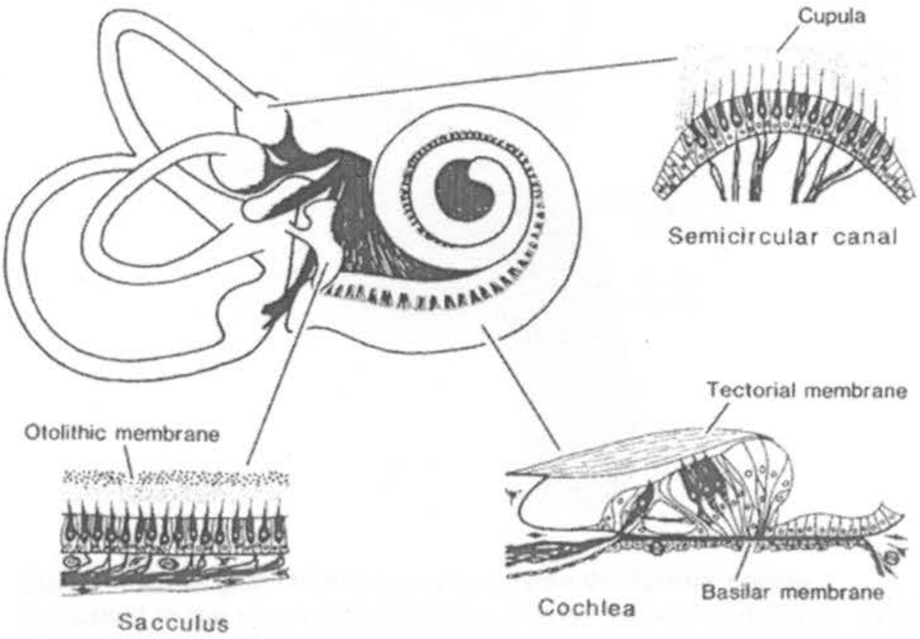

Fig. 1. The mammalian inner ear. The auditory organ is the cochlea and the five vestibular organs are the three semi-circular canals, the utriculus and the sacculus. The sensory epithelia of auditory and vestibular organs is where hair cells reside *(From Hudspeth, 1989).*

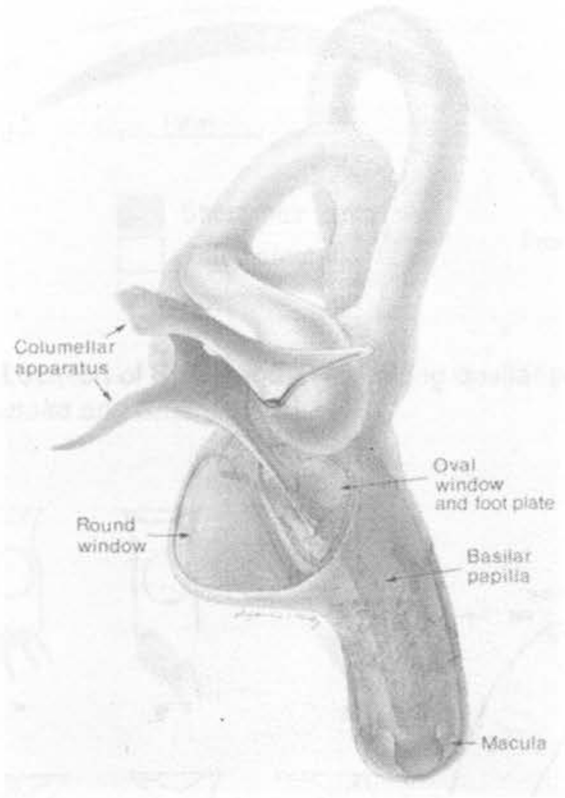

Fig. 2a. Drawing of chicken inner ear. Note the basilar papilla, equivalent to the mammalian cochlea. *(From Tanaka and Smith, 1978)*

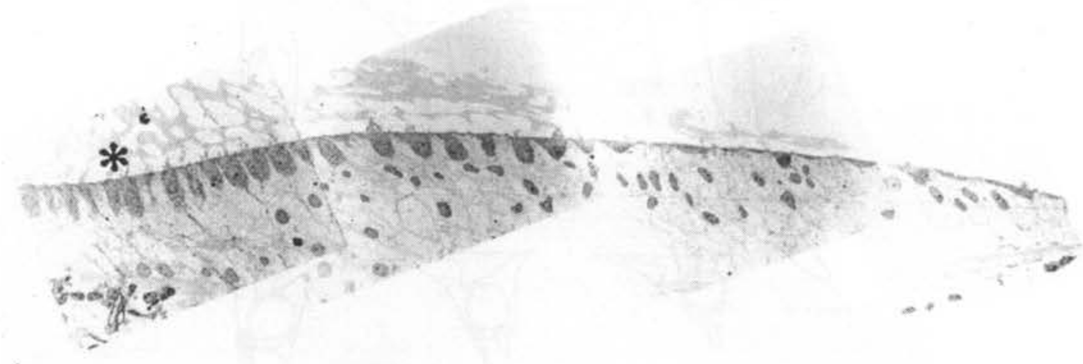

Fig. 2b. Electron micrograph illustrating the cross-section through the chicken basilar papilla. Note the gradation of cell shape and size of THCs to SHCs from left to right. *Scale bar* = 57 μm *(From Martinez-Dunst et al., 1997).*

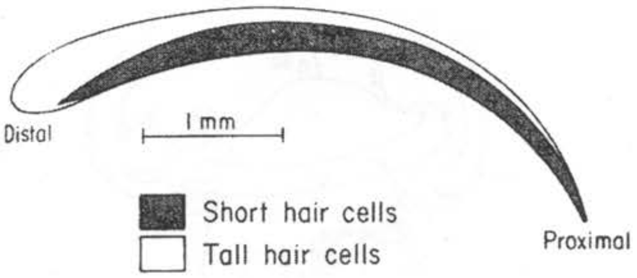

Fig. 3a. Location of SHCs and THCs along basilar papilla *(From Tanaka and Smith, 1978).*

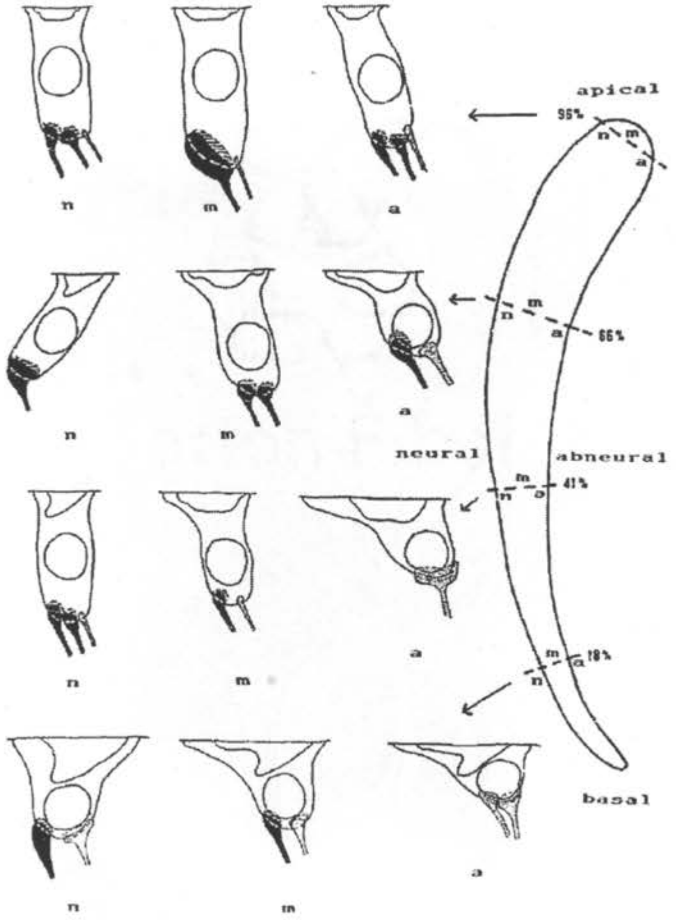

Fig. 3b. Afferent and efferent contacts on SHCs and THCs along the basilar papilla. Note that the THCs are contacted primarily by afferent terminals, whereas, SHCs are contacted primarily by efferent fibers *(From Fischer, 1992).*

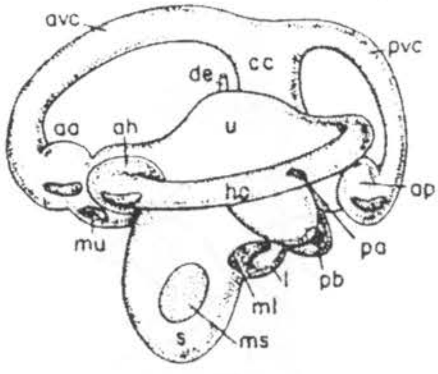

Fig. 4a. Bullfrog inner ear. s = sacculus, ms = macula of the sacculus where hair cells reside *(From Lewis et al., The Vertebrate Inner Ear, 1985).*

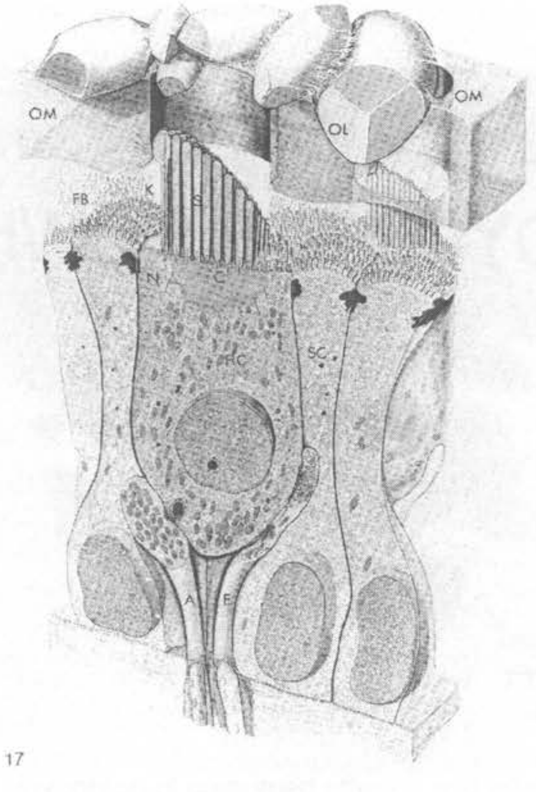

Fig. 4b. Drawing of bullfrog saccular hair cell within the macula. Hair cell (HC), supporting cell (SC), otolithic membrane (OM), afferent fiber (A) and efferent fiber (E) *(Hillman DE. Morphology of peripheral and central vestibular systems. In: Llinas, R and Precht, W. editors. Frog Neurobiology. Berlin: Springer-Verlag; 1976. p. 452-79).*

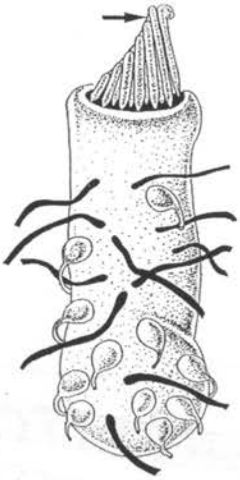

Fig. 5a. Afferent and efferent contacts on bullfrog saccular hair cell. Afferents are black and efferent boutons are shaded white *(From Lenzi and Roberts, 1994).*

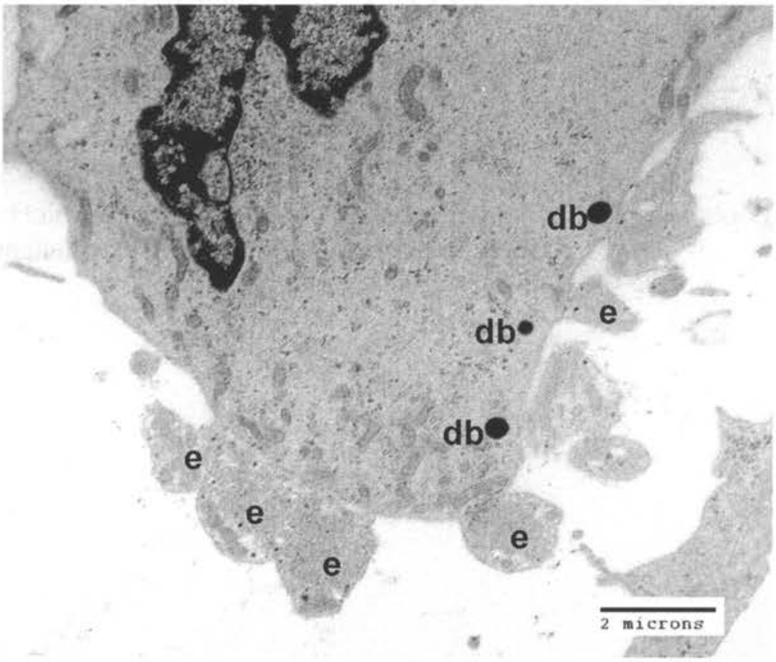

Fig. 5b. Electron micrograph of presumed efferent and afferent terminals at the base of a bullfrog saccular hair cell. Afferent synapses are identified by osmiophilic dense bodies (db). Efferent synapses are identified by synaptic vesicle-filled termini (e).

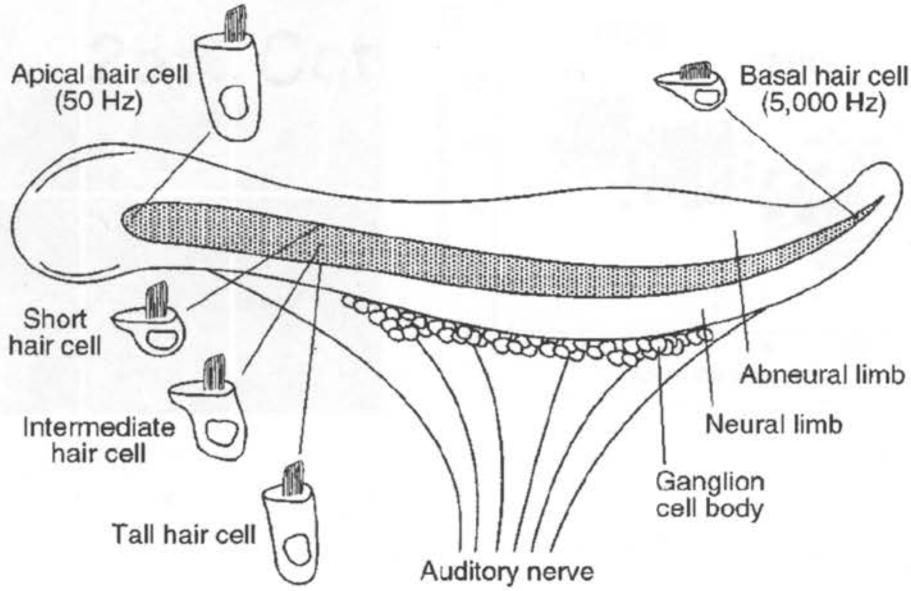

Fig. 6. Hair cell shape and tonotopic distribution of hair cells along the chick basilar papilla *(From Rosenblatt et al., 1997).*

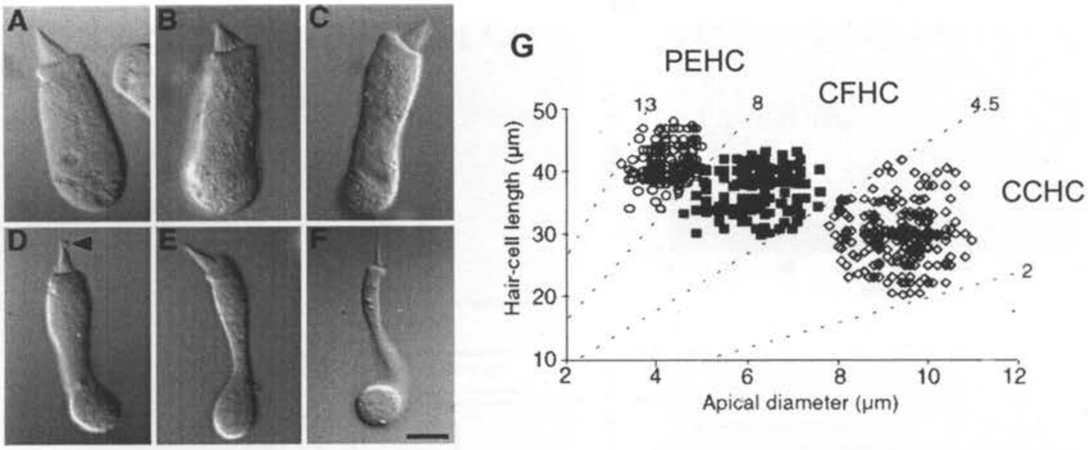

Fig. 7. Three hair cell types found in bullfrog saccular macula. A-C, CCHCs. D-E, CCFCs. F, PEHC. G, Plot demonstrates three populations of bullfrog saccular hair cells based on shape defined by the ratio of length to apical diameter *(From Chabbert, 1997).*

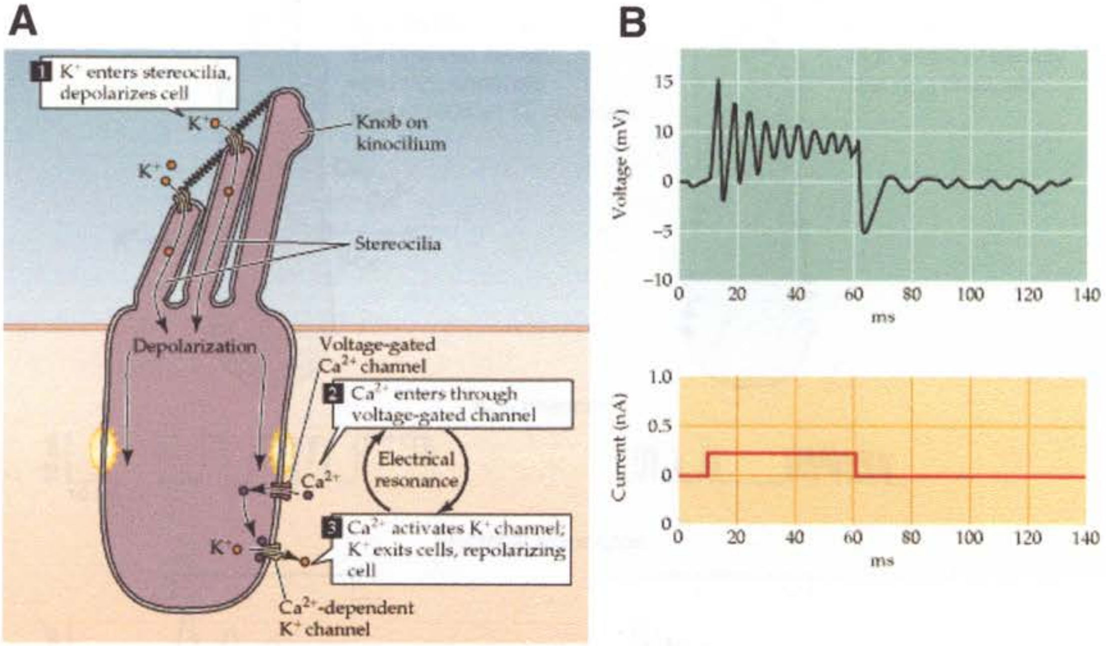

Fig. 8. Electrical resonance generated by current injection or bundle deflection. A. Diagram of the generation of electrical resonance by VGCC and BK channels following bundle deflection. B. A resonating membrane voltage can also be generated by a depolarizing current step *(From Purves D, Augustine GJ, Fitzpatrick D, Katz LC, LaMantia A-S, McNamara JO, Williams SM, editors. Neuroscience. 2nd ed. Sunderland (MA): Sinauer Associates, Inc.; c2001).*

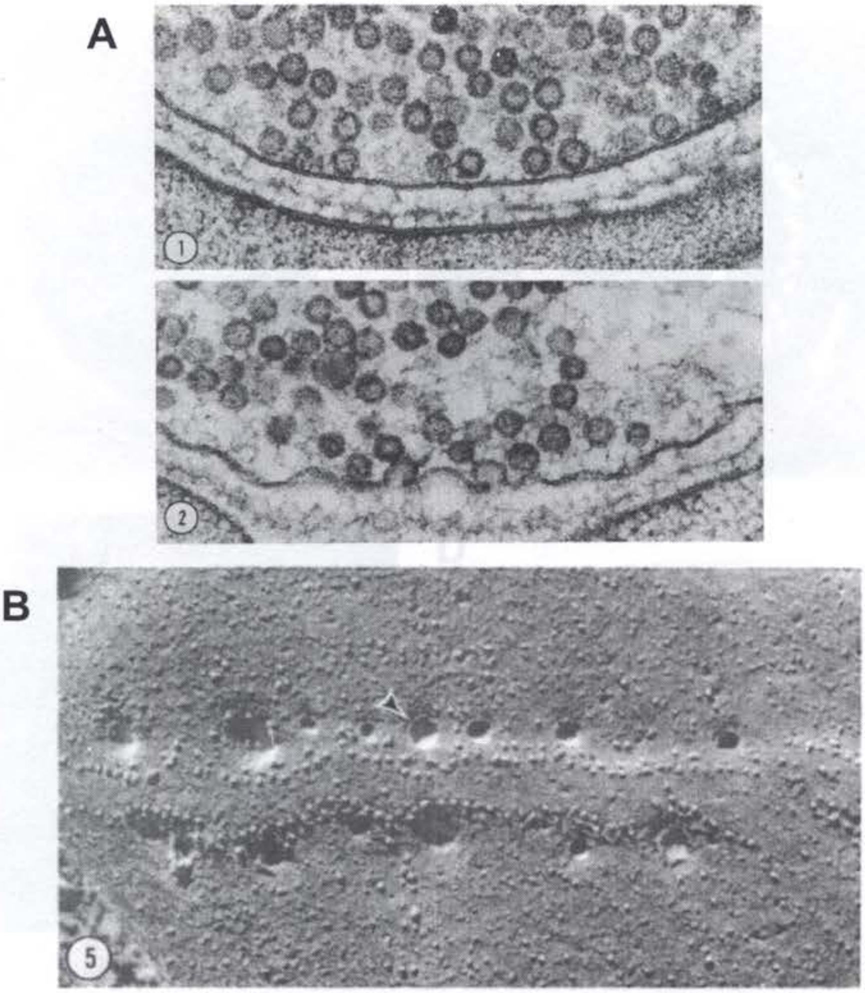

Fig. 10. Evidence for vesicle fusion at the synapse. A, EM of synaptic vesicles at frog neuromuscular junction, 1) before stimulus, 2) after stimulus. B, Freeze-fracture EM of rows of ion channel clusters and presumed vesicle fusion in mid-action, *arrowhead* (*From Heuser and Reese, 1981)*.

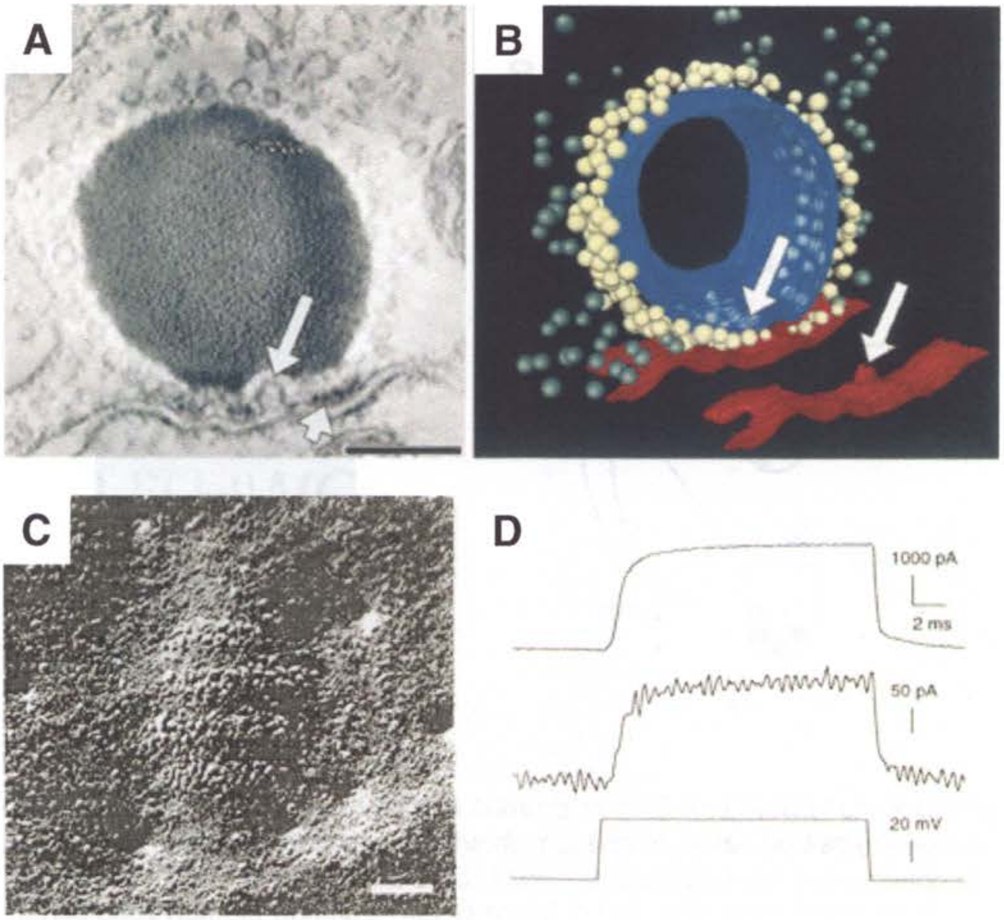

Fig. 11. Evidence for vesicle fusion at the dense body. A-B, EM and rendition of synaptic vesicles and dense body from electron tomography. C, Freeze-fracture EM of ion channel clusters in the plasma membrane beneath the dense body. D, Whole cell voltage clamp recording, *top*, vs. membrane patch voltage clamp recording of one channel cluster, *middle*, in hair cells in response to a voltage step, *bottom* (*From Lenzi et al., 1999 for A and B; Roberts et al., 1990 for C; Issa and Hudspeth, 1994 for D).*

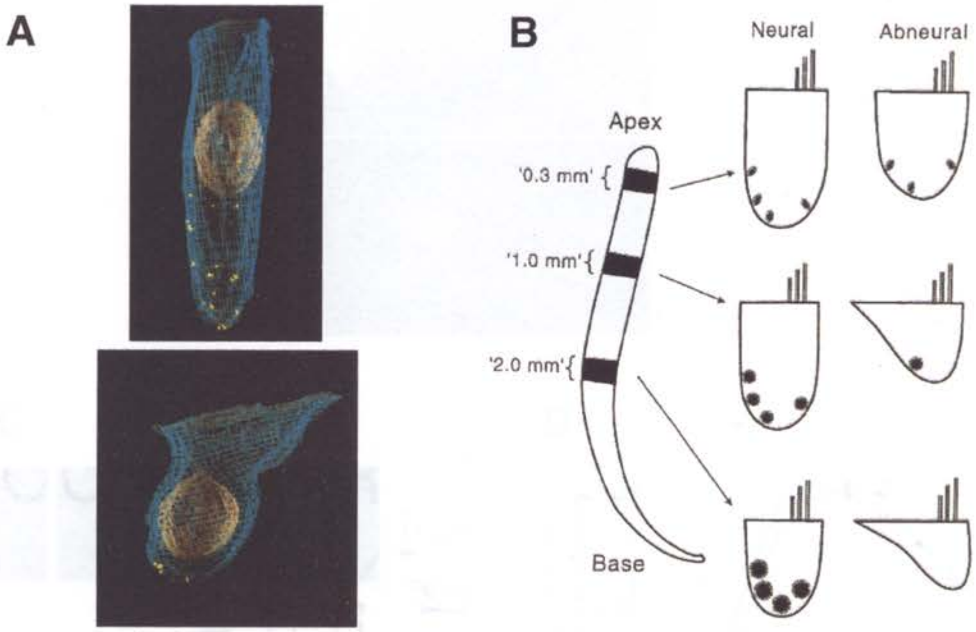

Fig. 12. Dense bodies and barium currents in THC and SHC of chick basilar papilla. A, 3-D reconstructions of the distribution of dense bodies (shown in yellow) in a THC, *upper,* and a SHC, *lower.* B, Illustration of the variation in dense body number and size (*not to scale*) in hair cells along the basilar papilla (*From Martinez-Dunst et al., 1997).*

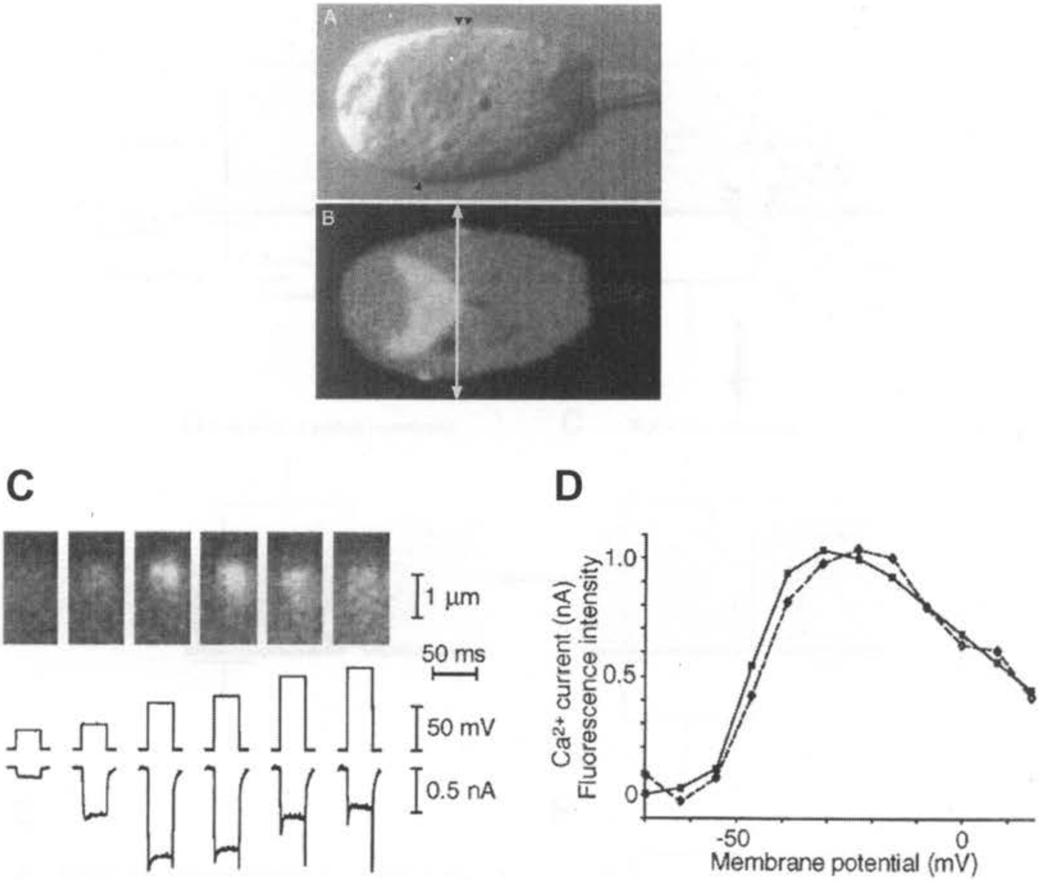

Fig. 13. Calcium influx at the dense body. A, DIC image of a hair cell. B, Confocal imaging of calcium-sensitive Fluo-3 dye in the same hair cell shown in *A*. C, *top*, Line-scan images at one dense body at *white double-pointed arrow* in *B*, *bottom*, calcium currents in response to voltage steps, *middle*. D, Correlation of fluorescence intensity changes with calcium current amplitudes in response to changes in membrane voltage (*From Issa and Hudspeth, 1996).*

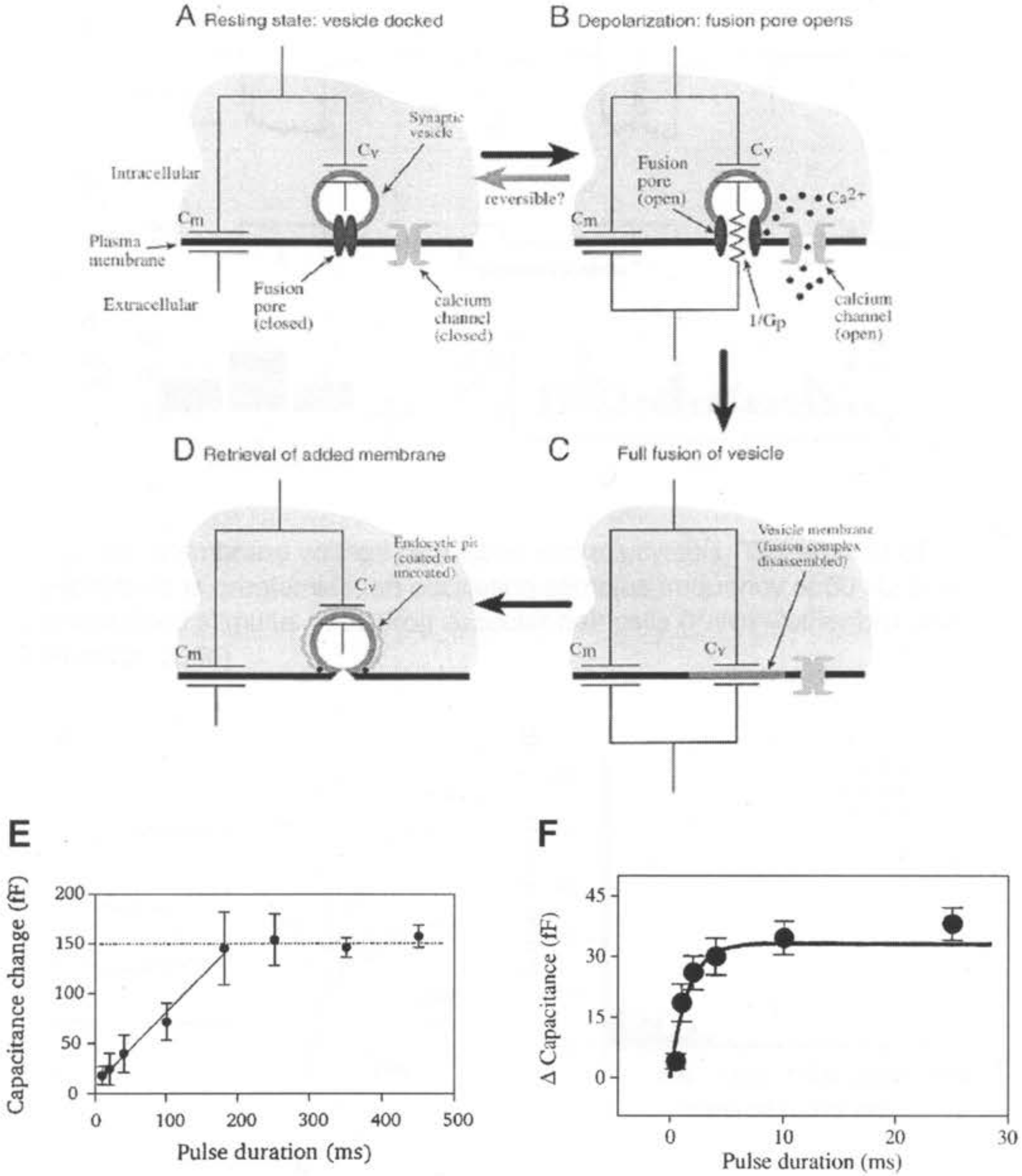

Fig. 14. Membrane capacitance measurements and the readily-releasable pool. A-D, Cartoon depicting the measurement of vesicle membrane addition by membrane capacitance recording (*From Matthews, 1996*). E and F, RRP and ultra-fast RRP, respectively, revealed in membrane capacitance recordings of retinal bipolar cell terminals (From *von Gersdorff and Matthews, 1994 and Mennerick and Matthews, 1996, respectively)*.

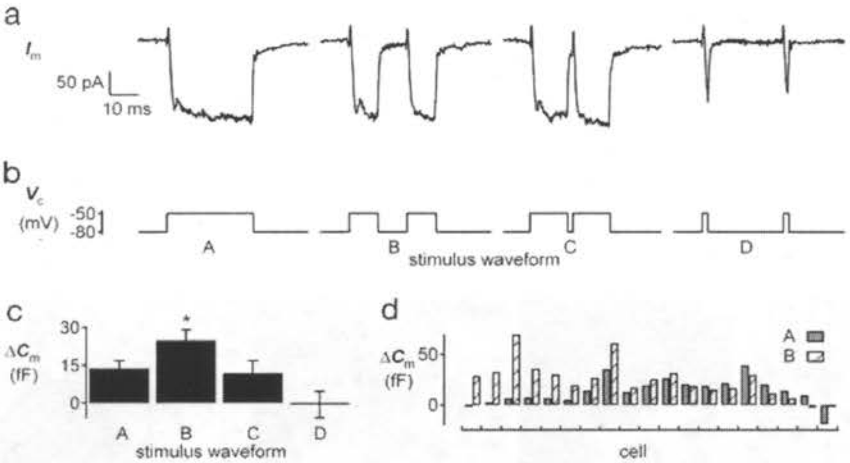

Fig. 15. Membrane voltage oscillation and exocytosis. The amount of exocytosis is greater with an oscillating stimulus frequency of 50 Hz than a sustained stimulus in bullfrog saccular hair cells (*From Rutherford and Roberts, 2006*).

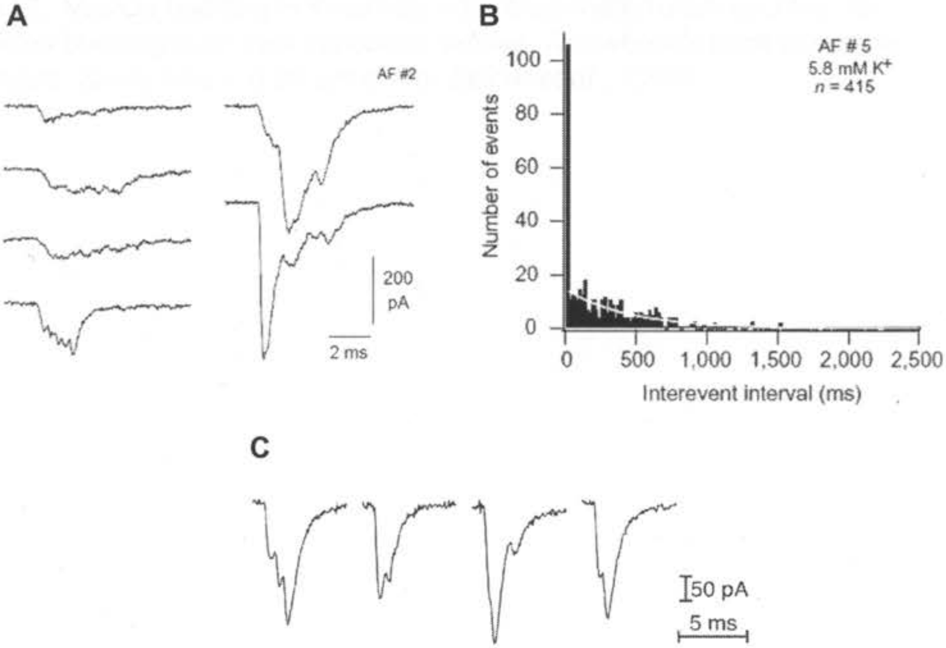

Fig. 16. Evidence for multi-vesicular exocytosis in hair cells. A, 'Multiphasic' spontaneous release events recorded at the afferent terminal in an intact mouse preparation and B, Histogram demonstrating coordinate release (*From Glowatzki and Fuchs, 2002)*. C, Multi-vesicular events were also observed in afferent recordings of the intact bullfrog amphibian papilla *(From Keen and Hudspeth, 2006)*.

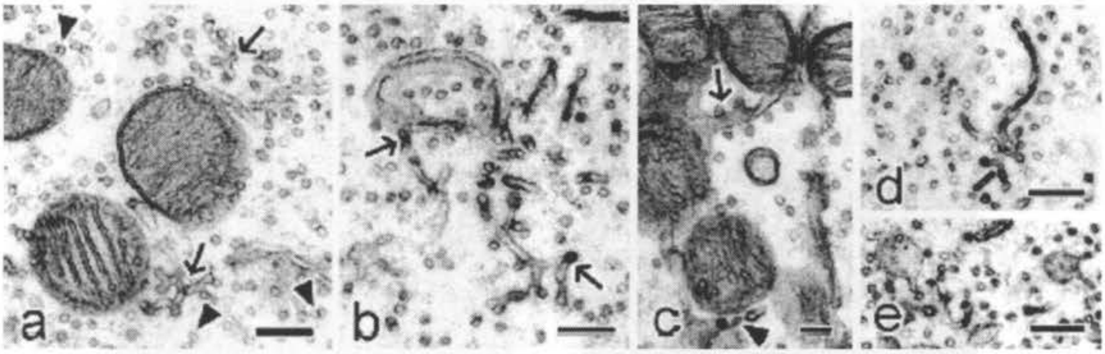

Fig. 17. Vesicle budding in inner hair cells from mammalian cochlea. Note vesicles budding from mini-canaliculi, *arrows*. *Arrowheads* point to vesicle doublets. *Scale bars = 0.25 μm (From Spicer et al., 1999)*

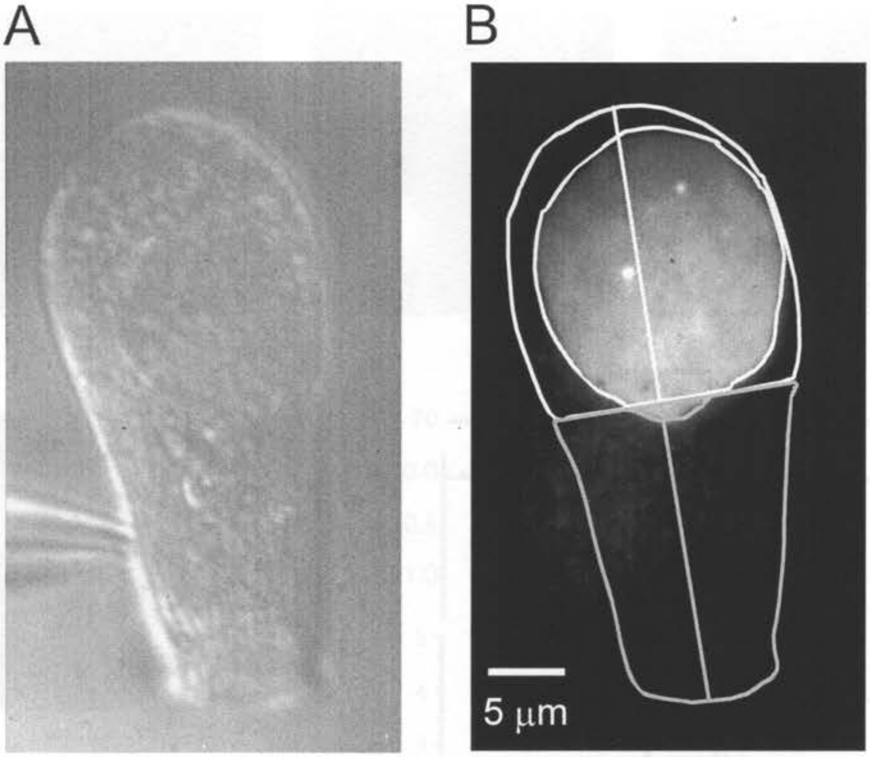

Fig. 18. Fluo-3 labels dense bodies in frog saccular hair cells. A, Differential interference contrast image of a frog vestibular hair cell loaded with Fluo-3 and 10 mM EGTA via a patch pipette contacting the cell from the left. B, Evanescent field fluorescence image with outline of the cell under differential interference contrast (*A*). To define apical and basal regions, a line was drawn down the long axis of the cell and bisected in the middle. The apical half is enclosed by the *gray outline*; it was not used in additional analyses. The *white outline* surrounds the basal half. A second *near-circular outline* within indicates the area of the footprint. Two bright spots in the cell are readily seen; they mark the locations of two dense bodies as previously demonstrated by Issa and Hudspeth (1996).

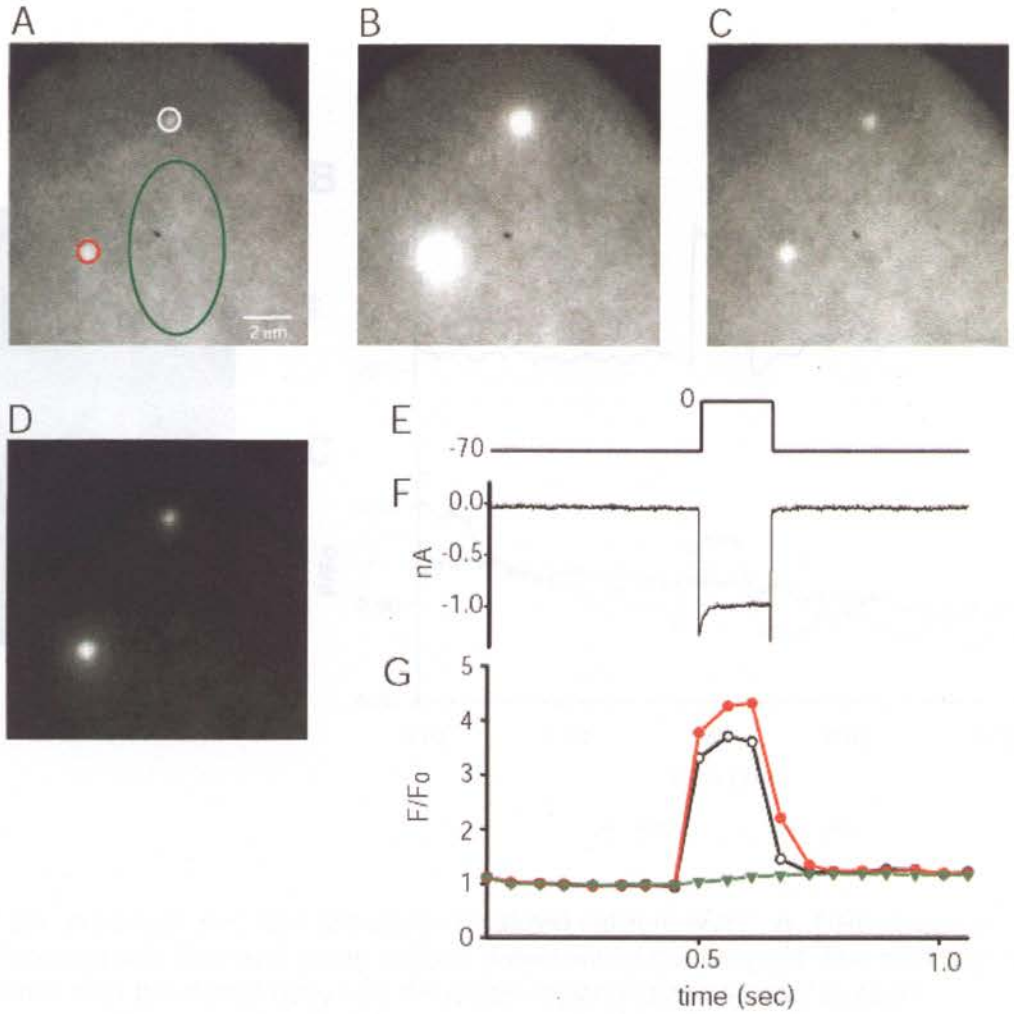

Fig. 19. Localized calcium entry in frog hair cells. A–C, Basal portion of a hair cell before, during, and after a voltage pulse from -70 to 0 mV. Exposures are for 150 ms in *A* - *C*. In hair cells, fluorescent spots are clearly visible even in the absence of a depolarizing stimulus, and they brighten dramatically when Ca^{2+} channels open and seem to broaden; this is caused by contrast saturation. D, When *B* is printed at diminished brightness, fluorescence is tightly localized to the two bright spots. E, Voltage (in mV). F, Calcium current. G, Fluorescence in the three regions outlined in *A*, plotted against time. *Traces* are color-coded to indicate the regions to which they apply. Fluorescence for each region is normalized by the average value during 350 ms before the voltage pulse.

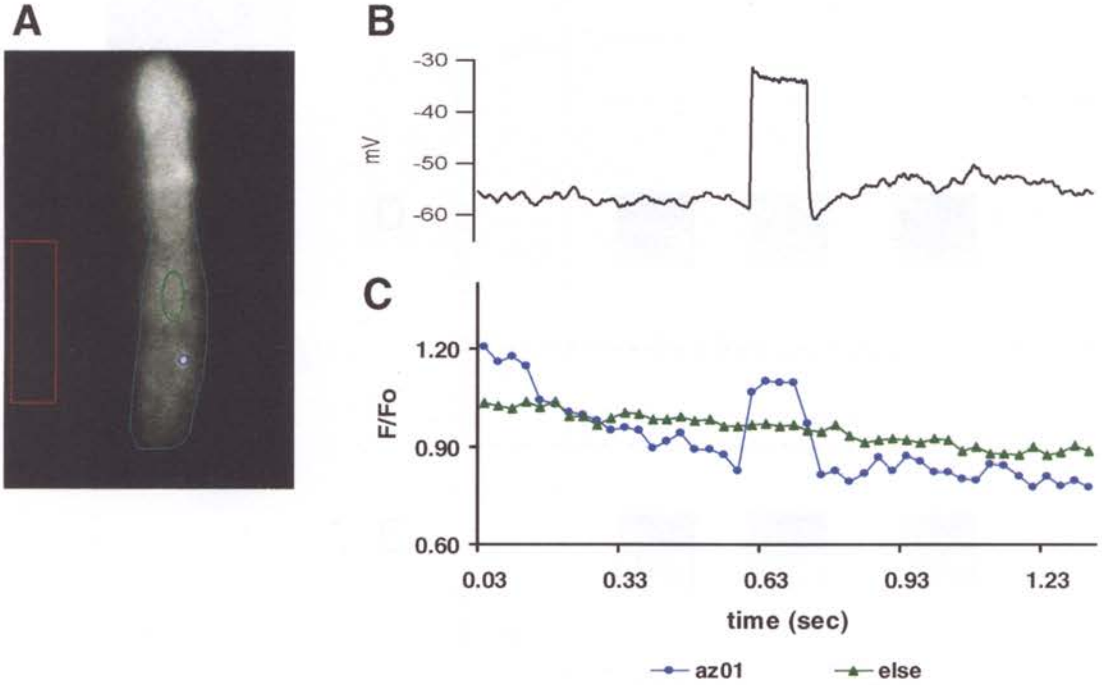

Fig. 20. A current step also stimulates localized calcium entry. A, TIRF image of the footprint with blue and green regions drawn within the footprint. The blue region is drawn over the dense body and the green region indicates basal footprint background fluorescence. B, Voltage response to 250 pA current step. Current is outward since the internal solution lacks both cesium and TEA. C, Fluorescence intensity traces over time for the blue and the green regions indicated in *A*. Fluorescence intensity is normalized to the time before the current step.

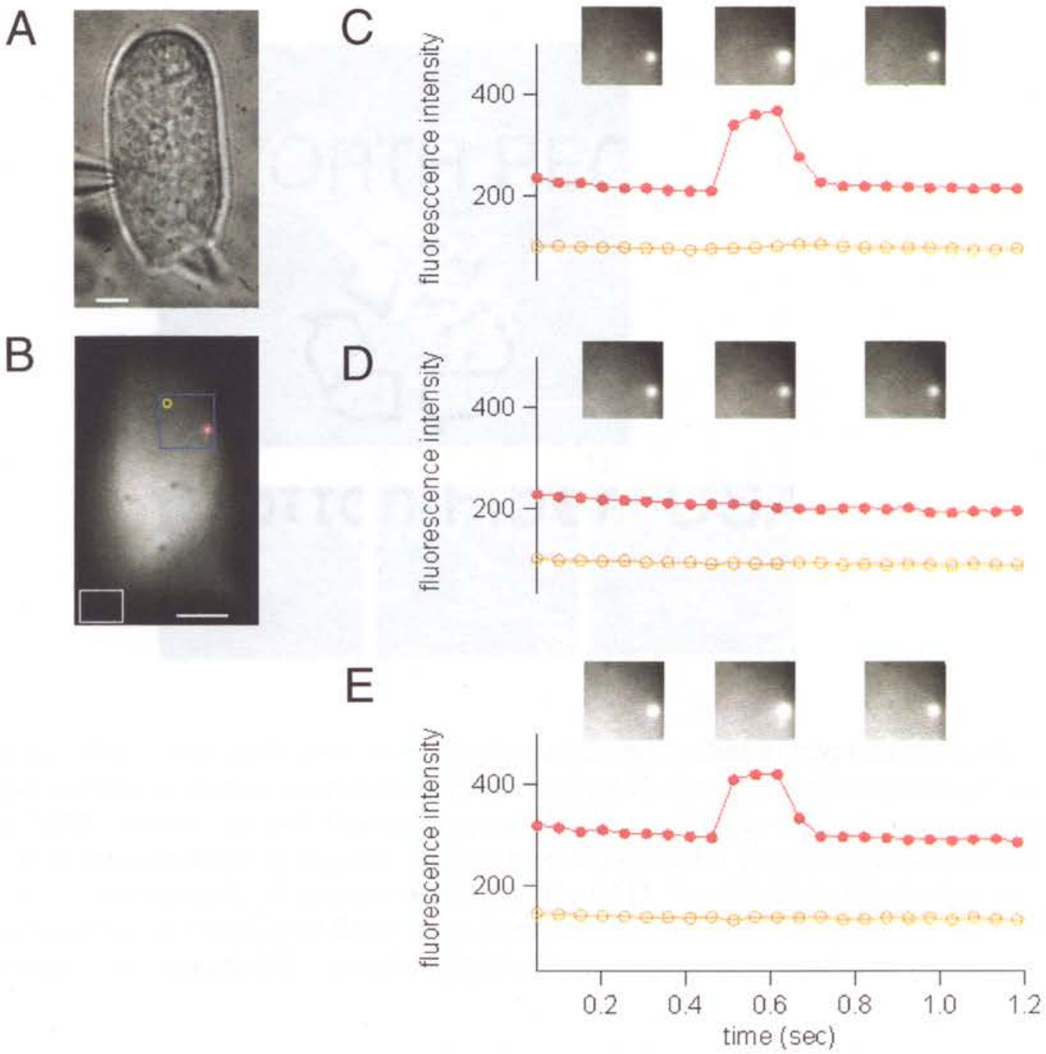

Fig. 21. Localized calcium entry is dependent on external calcium. Removal of extracellular calcium does not alter the basal fluorescence of the dense bodies, whereas the increase in fluorescence intensity at the dense body due to VGCC activation is lost. A, DIC image of an isolated bullfrog saccular hair cell with the recording pipette on the left. B, Corresponding footprint imaged with TIRF microsocopy. *Scale bars* = 5 µm. Three voltage steps were applied to the hair cell and the results are shown in C (4 mM external Ca^{2+}), D (0 mM external Ca^{2+}) and E (return to 4 mM external calcium). Cropped images (see *blue* square ROI drawn over the dense body in *B)* are averages of three frames before, during and after a given voltage step and are shown above the corresponding frames. Fluorescence intensity traces in *C - E* correspond to the two circular 8 pixel diameter ROIs depicted in *B*. As can be seen in both the images and the fluorescence intensity traces, bathing the cell in 0 mM $[Ca^{2+}]_o$ abolishes the increase in fluorescence during the voltage step, whereas, the fluorescence of the dense body is maintained even when VGCCs are open.

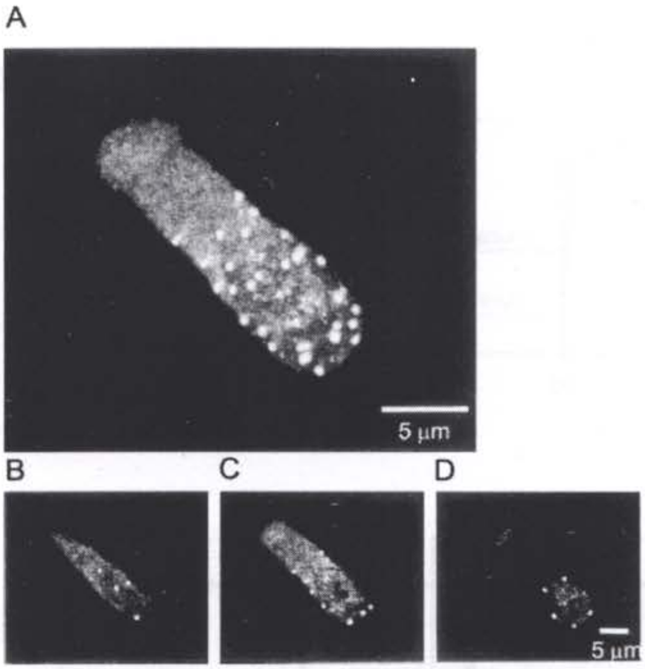

Fig. 22. CtBP-immunofluorescence labeling of dense bodies in frog hair cells. A, Maximum fluorescence at each pixel location in all 25 confocal sections through an anti-CtBP-labeled hair cell. Fluorescent spots representing dense bodies are mostly found in the basal half of the cell. The nucleus did not stain prominently in hair cells. B, Bottom-most confocal section of the cell. C and D, Two sections taken near the middle of the cell. Note that CtBP spots in middle sections are found on the cell periphery, as expected for synaptic ribbons.

	Density (μm^{-2})	SE	Cells
Hair cells			
Calcium spots	0.034	0.008	7
Dense bodies	0.048	0.008	8

Table 1. Abundance of calcium spots and dense bodies in bullfrog saccular hair cells. Calcium spots, as shown in Fig. 19, and CtBP-positive spots, as shown in Fig. 22, were counted within the footprint of the basal half of the cell.

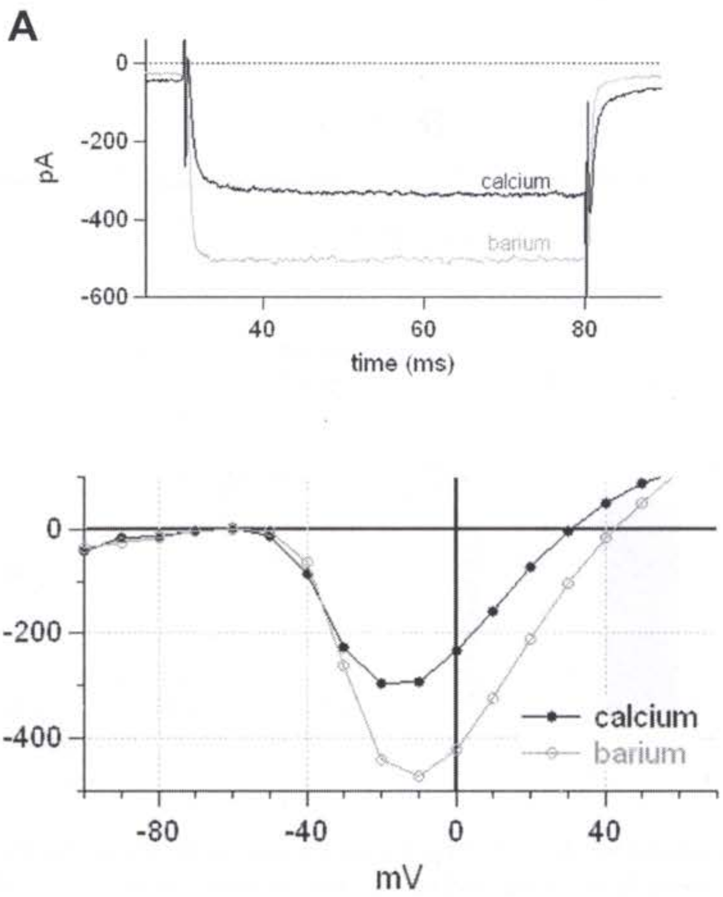

Fig. 23. Enhancement of inward current with barium. Replacement of 4 mM calcium with equimolar concentration of barium enhances the voltage-sensitive current in a bullfrog saccular hair cell. A, Voltage steps (50 ms) were applied while the cell was bathed in either calcium or barium bath saline. Traces show current responses to voltage steps from -60 to -10 mV in the same cell. B, IV plot of the current responses to a series of voltage steps in the same cell shown in *A*. Data values are the average current between 30 and 40 ms during the voltage step when the current was stable minus baseline current before the stimulus.

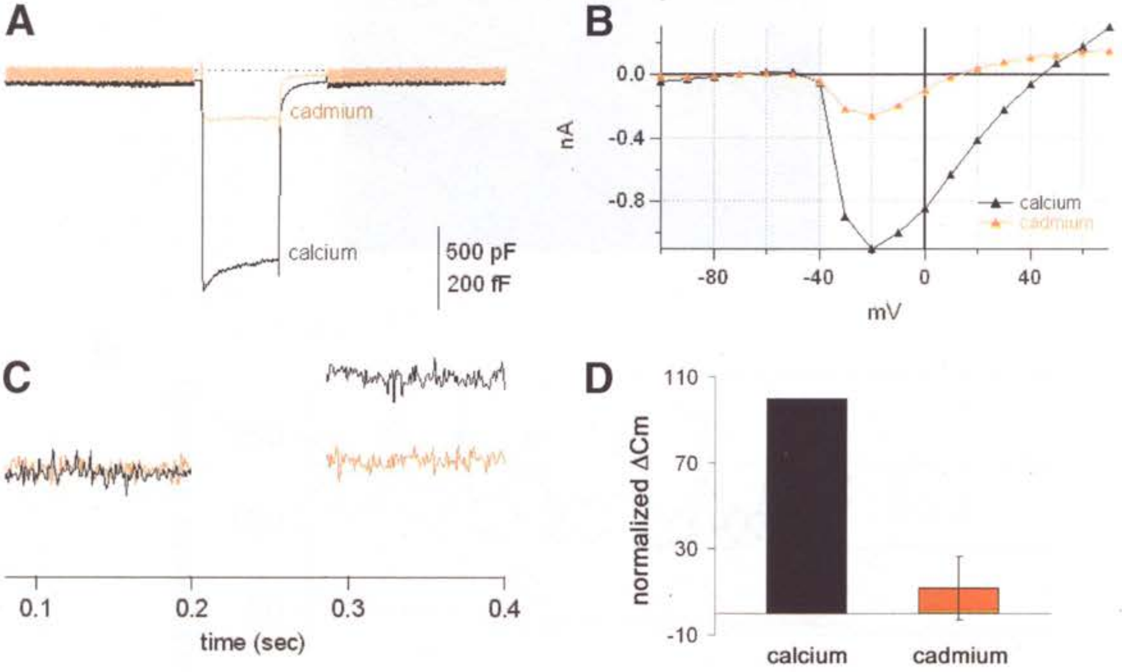

Fig. 24. Cadmium blocks the inward current and ΔC_m. A, Example voltage clamp recordings from a bullfrog saccular hair cell bathed either in standard bath saline or saline plus 100 µM cadmium. Current traces shown are when membrane was stepped to -20 from -70 mV. B, IV plot of the responses for the same cell shown in *A*. Cadmium block of inward currents was seen in 4 out of 4 cells. C, Membrane capacitance traces for the same cell and current recordings shown in *A*. D, Pooled ΔC_m responses to a voltage step from -70 to -10 mV in three bullfrog saccular hair cells bathed in either standard saline (calcium) or standard saline plus cadmium. Values normalized to the ΔC_m response in standard bath. Cadmium blocked 88.4 % of the ΔC_m response. *Error bars = +/- SE.*

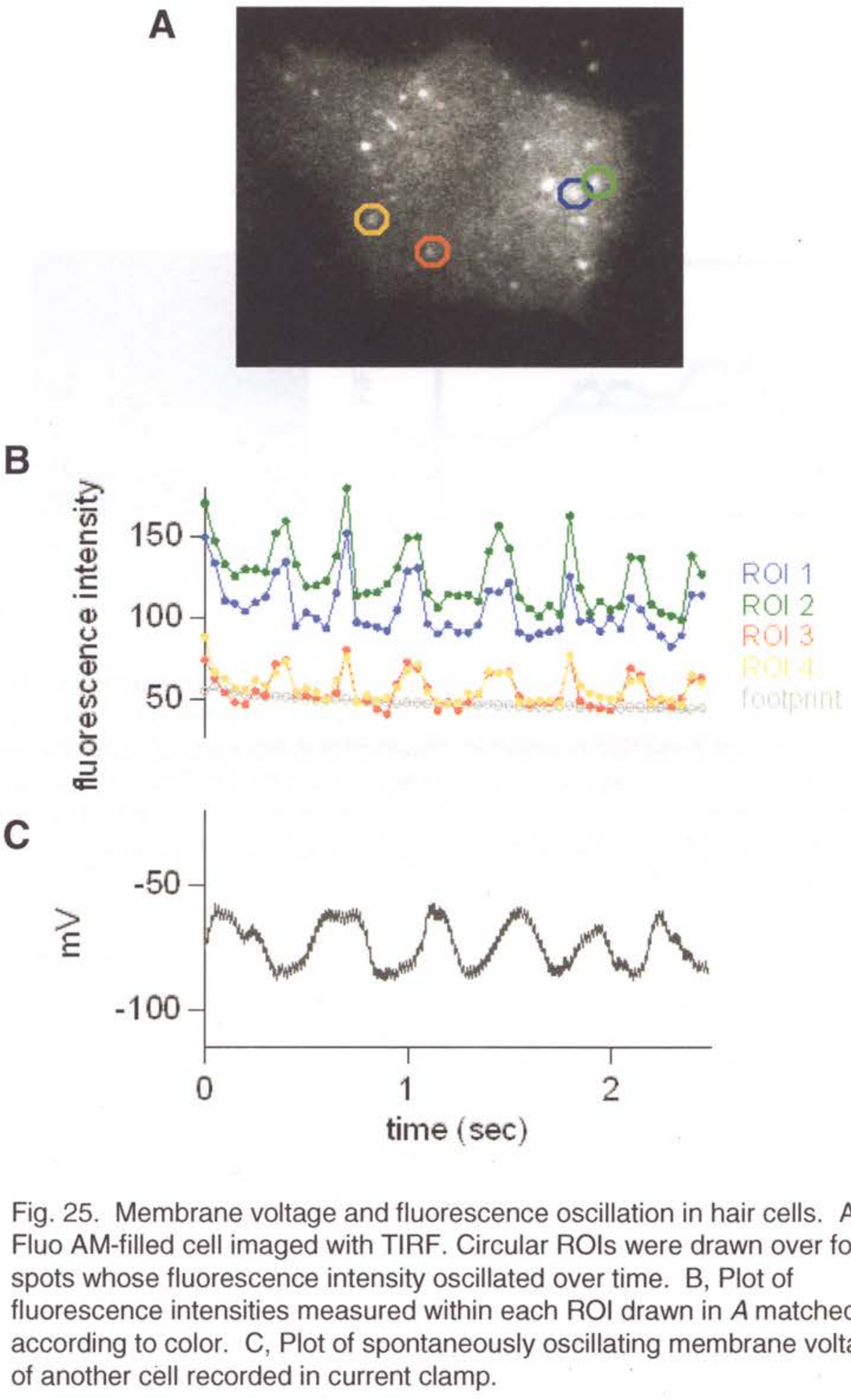

Fig. 25. Membrane voltage and fluorescence oscillation in hair cells. A, Fluo AM-filled cell imaged with TIRF. Circular ROIs were drawn over four spots whose fluorescence intensity oscillated over time. B, Plot of fluorescence intensities measured within each ROI drawn in *A* matched according to color. C, Plot of spontaneously oscillating membrane voltage of another cell recorded in current clamp.

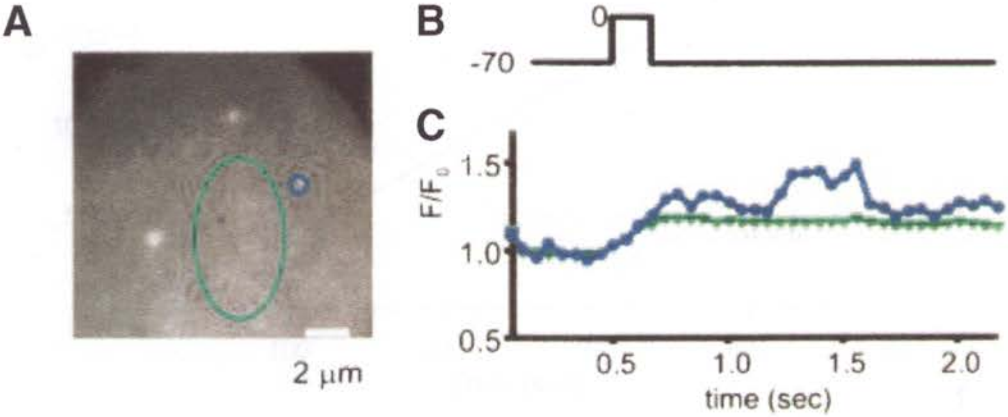

Fig. 26. Spontaneous fluctuations in fluorescence. A, Average of three 50 ms frames taken 1 sec after the voltage pulse. *Green region* is the same as in *Fig 19 A, blue region* shows a local and transient increase in calcium concentration. B, Voltage step (in mV). C, Fluorescence in *green* and *blue regions* plotted against time. Note that the *blue trace* shows a fluorescence increase occurring after calcium channels were shut by returning the membrane potential to -70 mV.

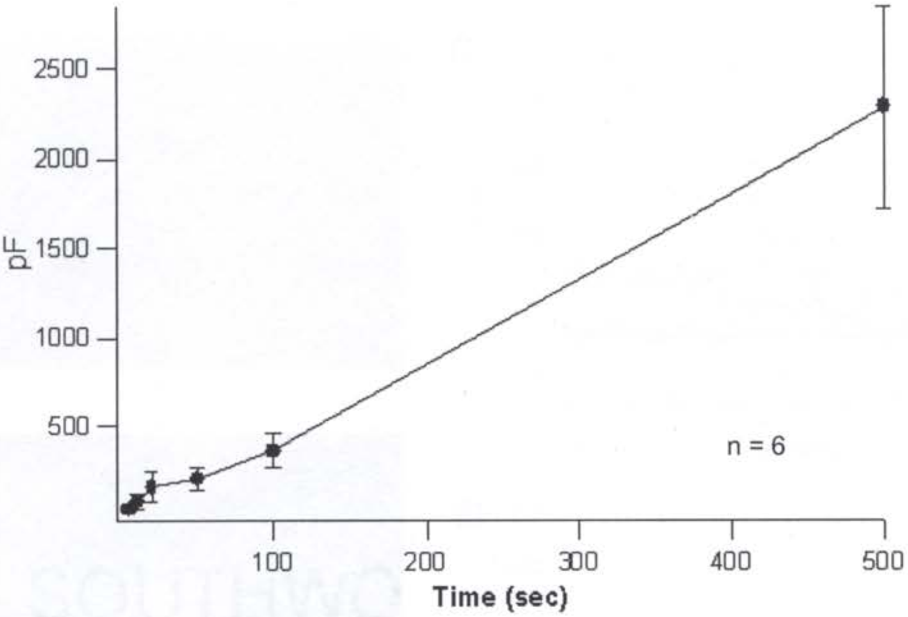

Fig. 27. Varied stimulus duration reveals two rates of exocytosis. Plot of ΔC_m jumps following increasing voltage step duration to 0 mV in six bullfrog saccular hair cells.

Pulse duration (ms)	delta cap (fF)	sterr	vesicles/sec
5	42	10	227027
10	84	40	227027
20	161	85	217568
50	208	68	112432
100	363	95	98108
500	2289	560	123730

Table 2. ΔC_m in response to varied stimulus durations. Size of the ΔC_m jumps and calculated exocytic rate from the data in *Fig. 27* reveals two rates of exocytosis. The capacitance of one synaptic vesicle is assumed to equal 37 aF and the capacitance of membrane is 1 μF/cm^2.

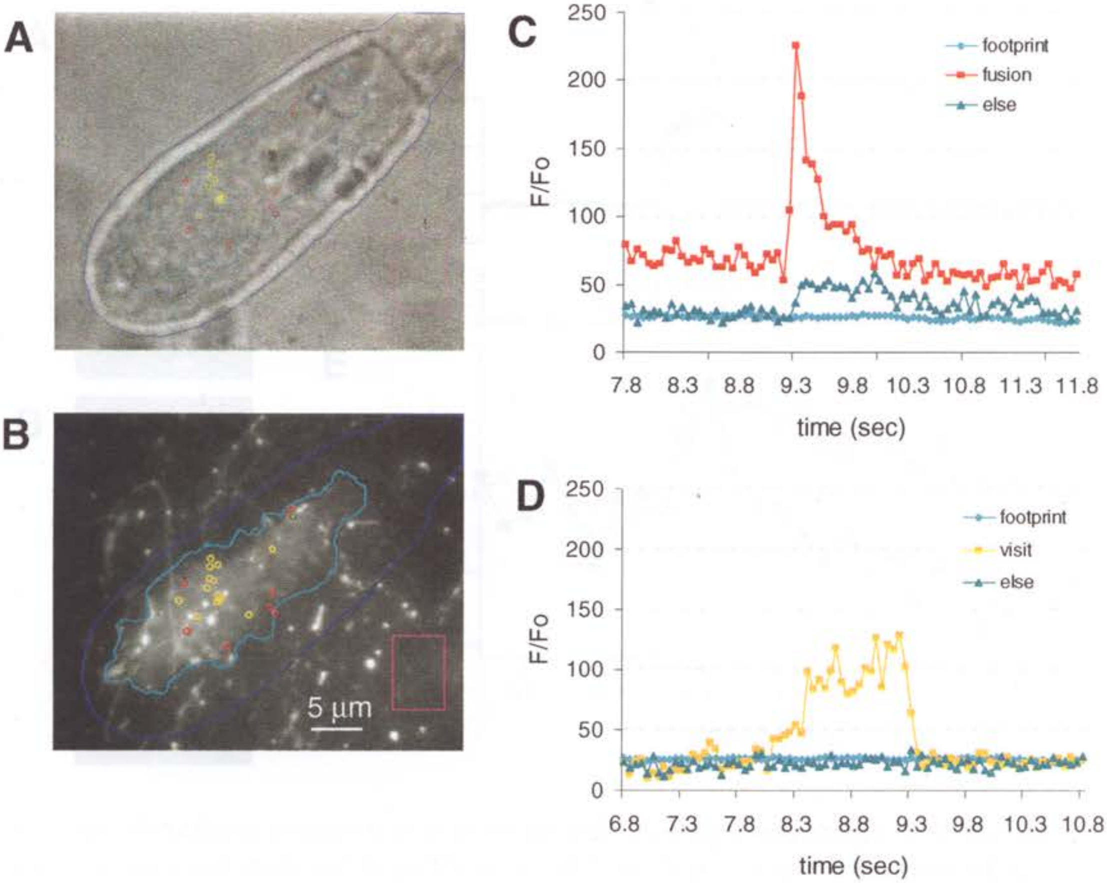

Fig. 28. Spontaneous vesicle fusion and visits imaged in hair cells. A, Brightfield image of an isolated saccular hair cell. B, TIRF image of the same cell in *A* that has been stimulated and labeled with 5 µM FM1-43 in 70 mM K^+ saline. Image is an average of a 500-frame stream acquired at 20 Hz. Regions depict events throughout the stream, *red circles* are fusion events, *yellow circles* are visits, *aqua* is the footprint, *purple* is the glass with no cell. C, example of a fusion event (*red*), footprint region near fusion event (*blue-green*) and footprint (*aqua*). D, example of a visit (*yellow*), footprint region near visit (*blue-green*) and footprint (*aqua*). All values in *C* and *D* have been background subtracted with the glass region (*purple*, in *A* and *B*) in each frame.

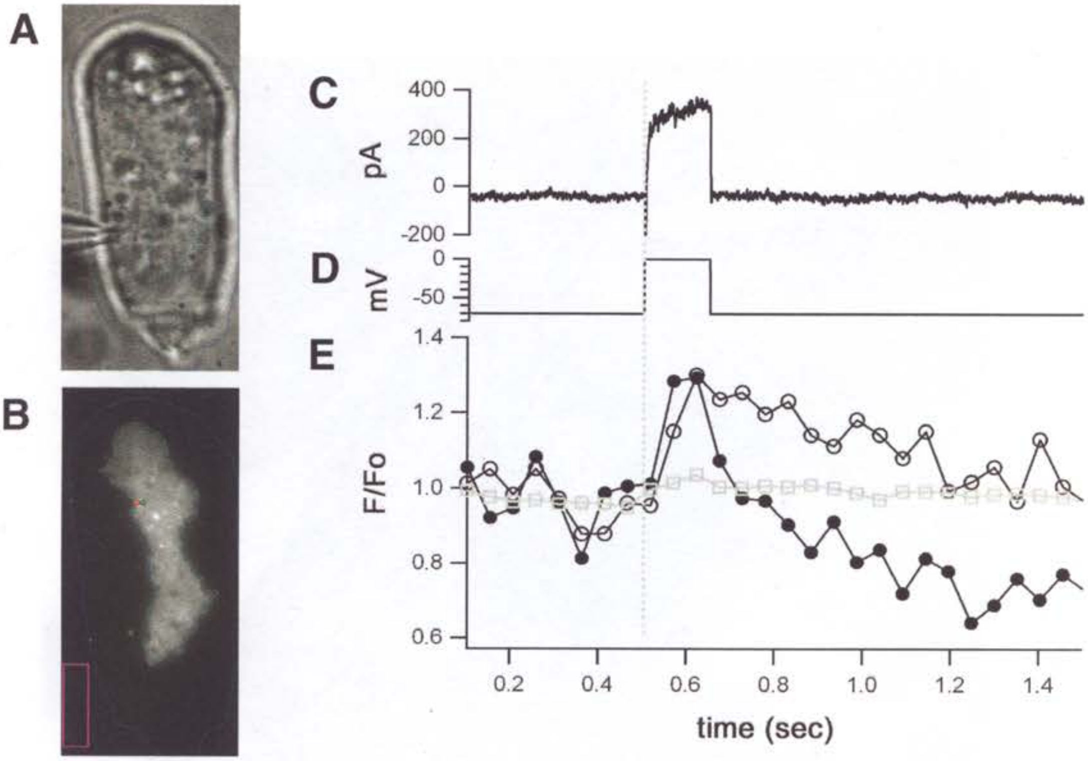

Fig. 29. Stimulated vesicle fusion in a hair cell. A, Brightfield image of an isolated saccular hair cell recorded in perforated-patch, voltage-clamp mode. Recording pipette at left. B, TIRF image of the same cell in *A* that has been stimulated and labeled with 5 μM FM1-43 in 70 mM K^+ saline. Image is an average of a 500-frame stream acquired at 20 Hz. C, Outward current in response to voltage step in *D*. Current is outward since the perforations in the membrane, which allow electrical continuity, are not big enough to permit dialysis of the cytosol recording pipette solution containing cesium and TEA. E, glass-subtracted and normalized fluorescence intensity traces of a presumed vesicle fusion event (*black dots* = *red* ROI in *B*), background footprint region adjacent to the presumed fusion site (*black circles* = *green* ROI in *B*) and of the whole footprint region (*grey squares* = *light blue ROI in B*). Glass region is shown in *purple* ROI in *B*. Traces in *C* – *E* are in the same time-scale. Onset of the voltage step is indicated by the grey dashed line.

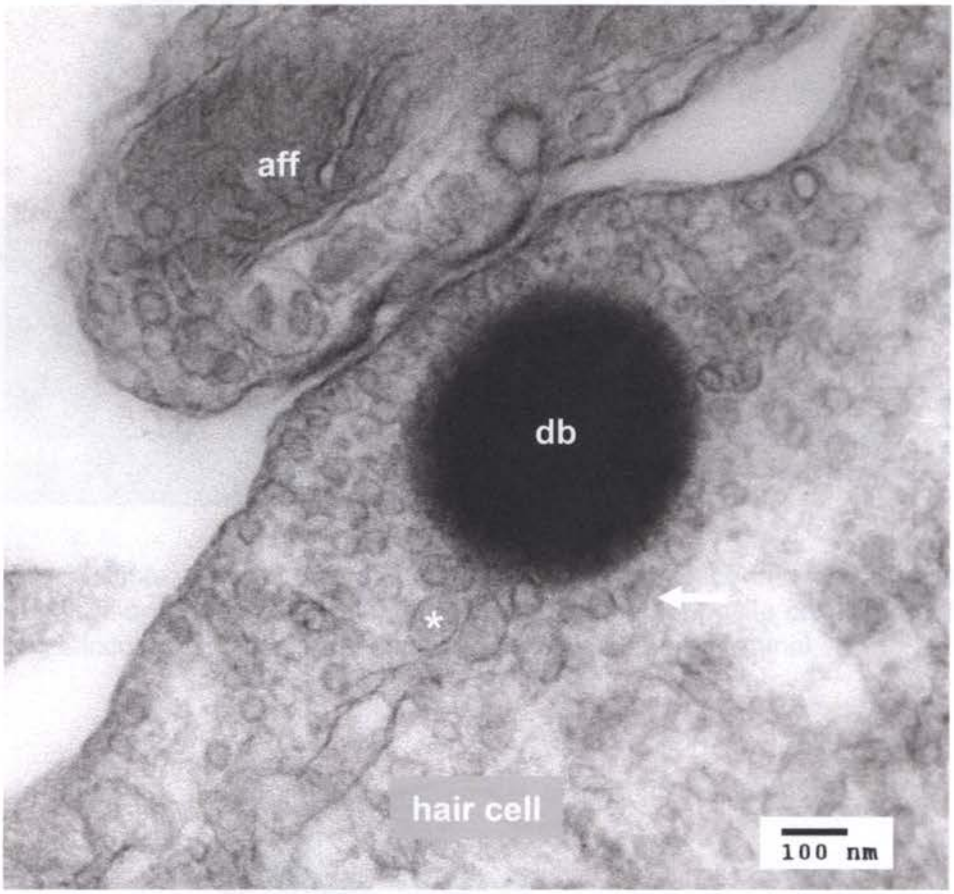

Fig. 30. Electron micrograph image of the afferent synapse. The osmiophilic dense body (db) in a bullfrog saccular hair cell (*hair cell*) is associated with small, clear synaptic vesicles (~30-50 nm diameter, *arrow*) as well as vesicles, of ~80 nm diameter or larger, *asterisk*. The afferent terminal (*aff*) is found opposite the dense body and vesicles.

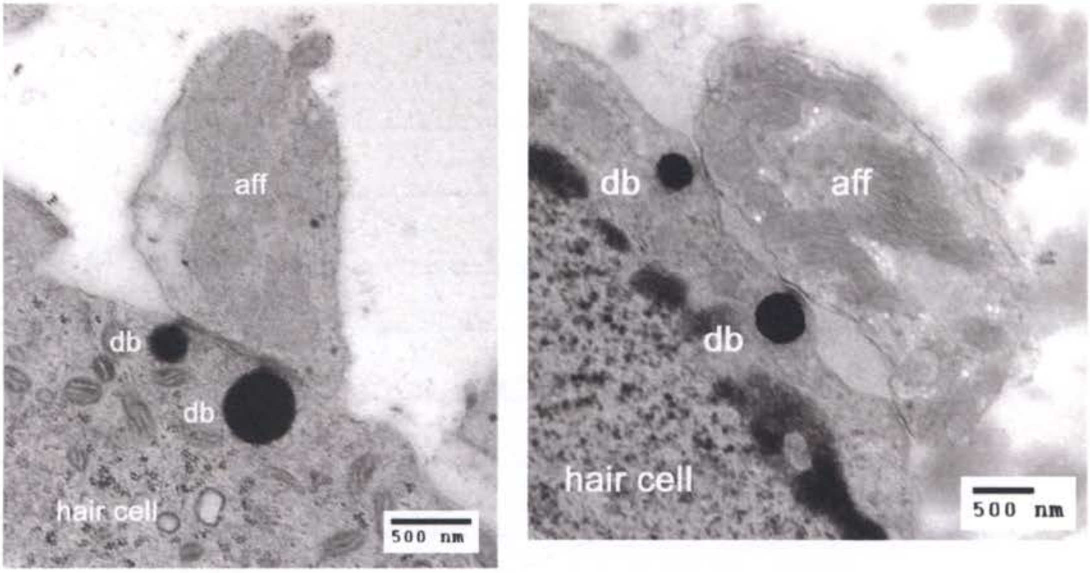

Fig. 31. Multiple dense bodies at the afferent synapse. Electron micrograph images of more than one dense body are sometimes observed opposite one afferent fiber in bullfrog saccular hair cells. *db* = dense body, *aff* = afferent terminal.

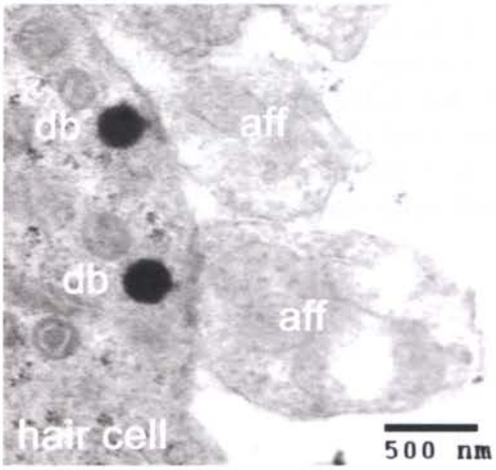

Fig. 32. Single dense bodies each opposite one afferent fiber. Electron micrograph images of one dense body per afferent fiber in a bullfrog saccular hair cell.

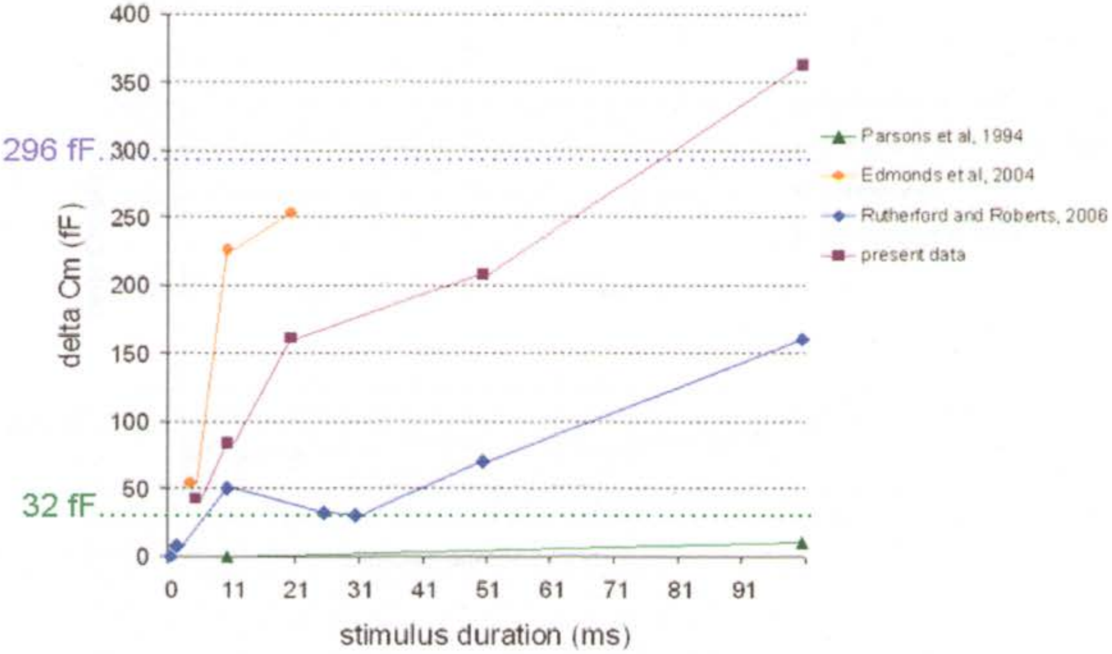

Fig. 33. Comparison of the RRP observed in ΔC_m recordings reported in the literature. The plot of ΔC_m vs. stimulus duration from the data presented in this thesis is compared with previously published data from similar experiments. All data from published work were recordings in hair cells from R. *pipiens*, whereas the new data here was carried out in hair cells from R. *catesbeiana*. 32 fF and 296 fF are the values for the estimated docked vesicle pool size and docked plus undocked pool size, respectively *(after Rutherford and Roberts, 2006).*

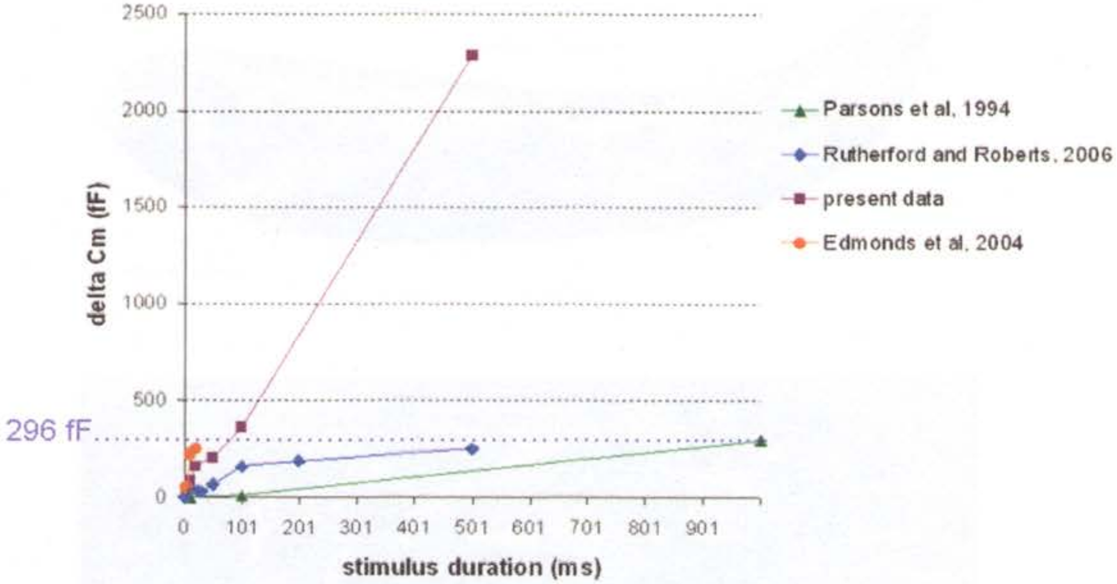

Fig. 34. Comparison of the slower exocytic rate following long voltage step durations. Same plot as Fig. 33 to compare results for longer stimulus durations *(after Rutherford and Roberts, 2006).*

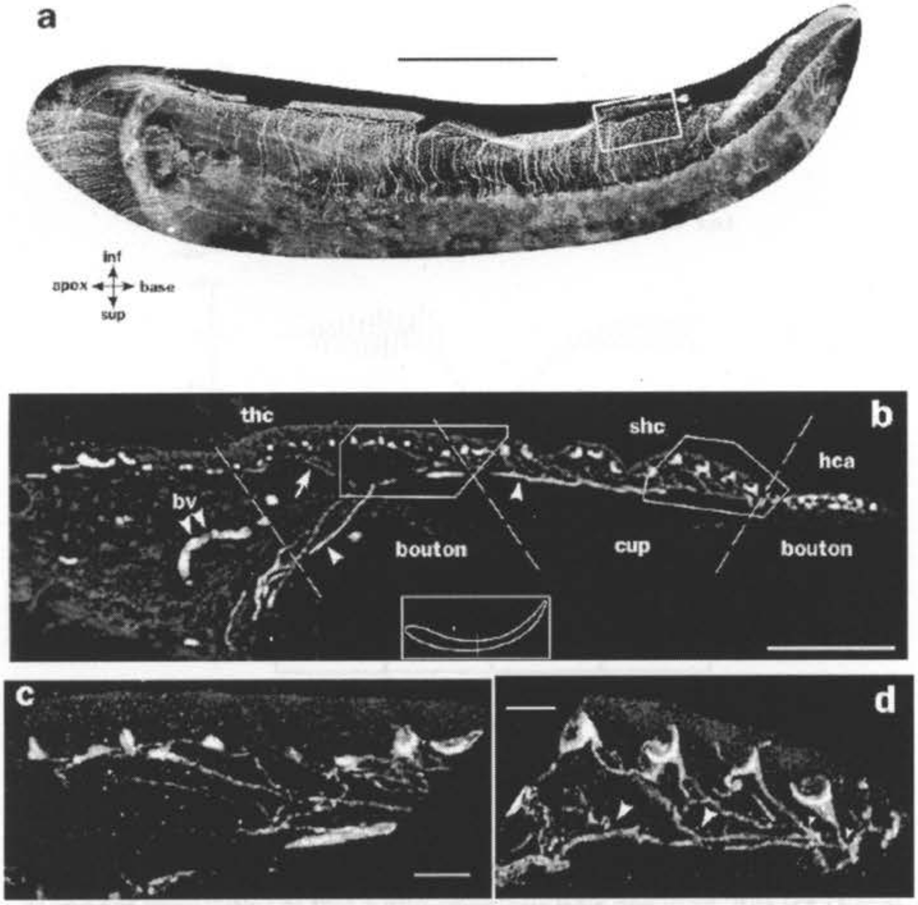

Fig 35. ChAT immunoreactivity in the basilar papilla of the chick. Note immunoreactivity in the calyx-type efferent terminals at the base of SHCs (*From Zidanic, 2002). Scale bars = 500 μm in a, 75 μm in b, 10 μm in c and d.*

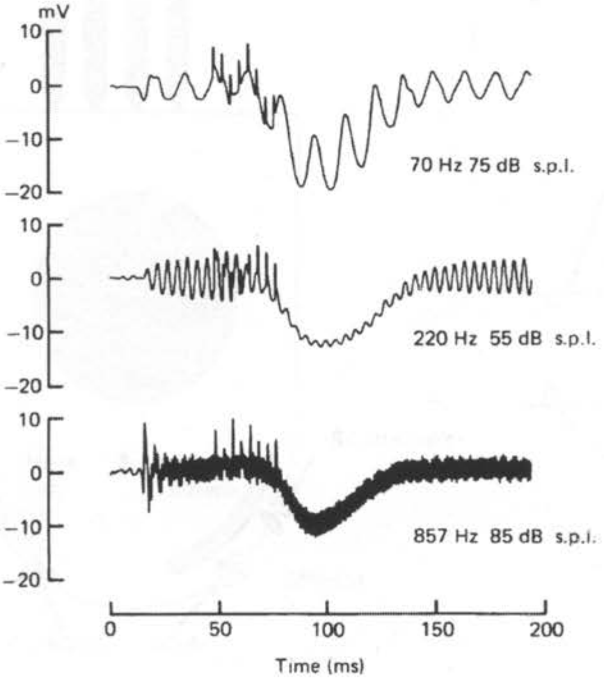

Fig. 36. Efferent inhibition is greatest at the resonant frequency. The resonant frequency of this turtle cochlear hair cell was 200 Hz (*From Art et al., 1985*).

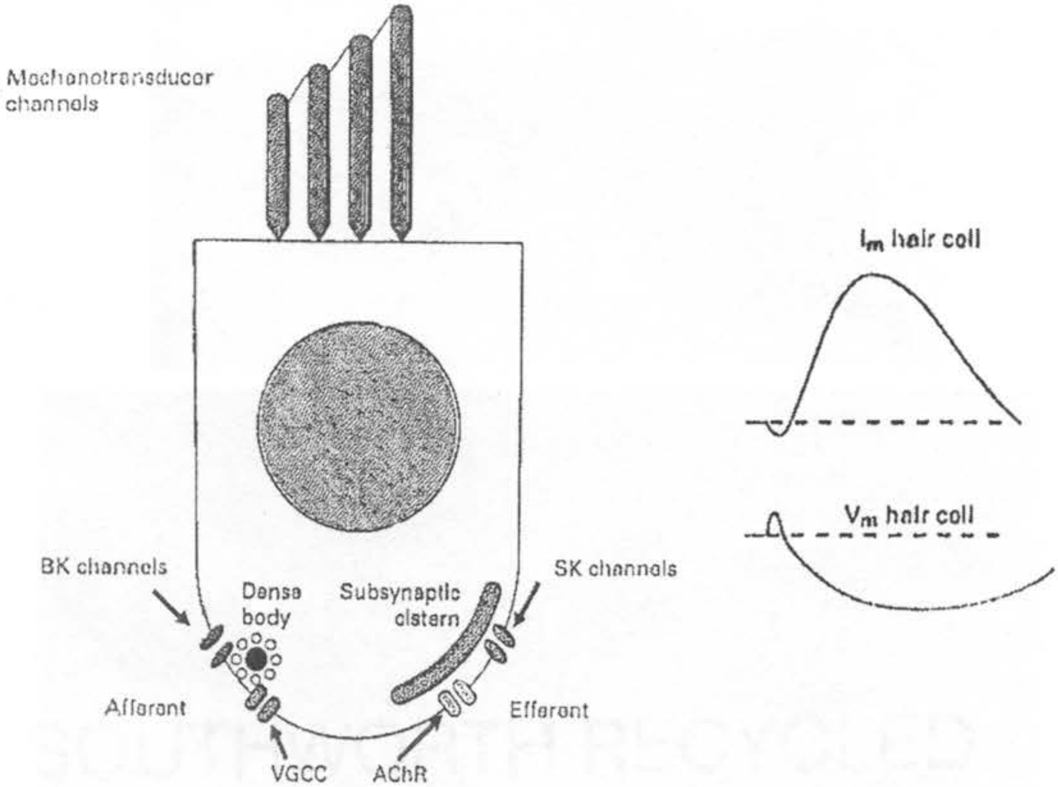

Fig. 37. Features of the efferent synapse and ionic currents there. *Left*, Cartoon of hair cell depicting the ion channels at the afferent and efferent synapses. *Right*, Typical membrane voltage and current responses to ACh. A brief initial inward current and membrane depolarization is attributed to calcium influx through nAChRs and a larger outward current and membrane hyperpolarization is due to SK channel activation by diffusion of calcium from the nAChRs *(From Fuchs, 2000).*

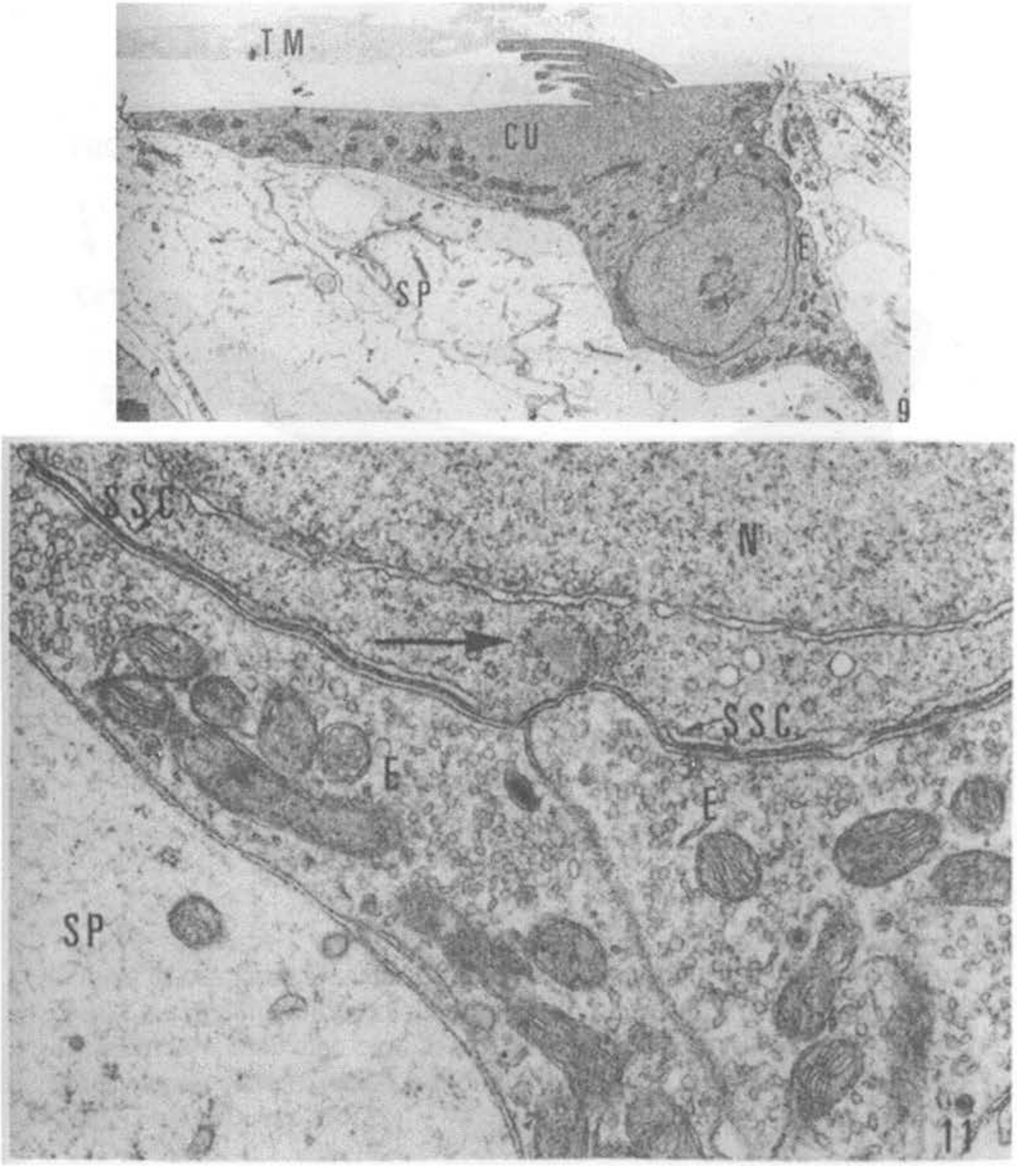

Fig. 38. Electron micrographs of chicken SHC. *Upper*, Typical SHC and large calyx-type efferent terminals. *Lower*, Enlargement of the efferent synapses. SSC = sub-synaptic cisternae, *Arrow* points to a dense body in a region where the SSC are absent. *(From Tanaka and Smith, 1978)*

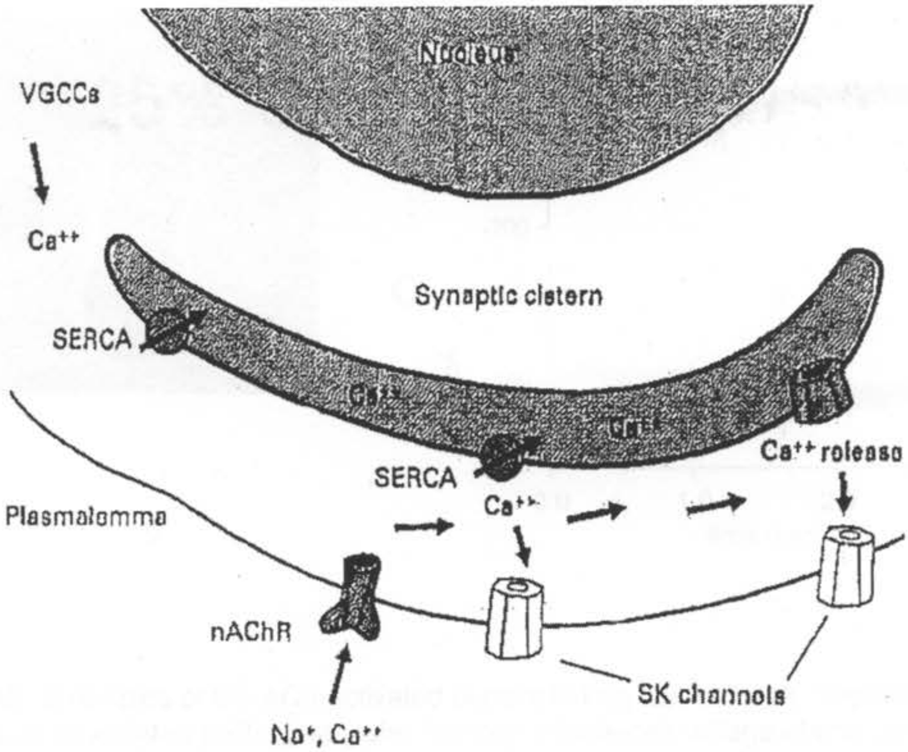

Fig. 39. Cartoon of the efferent synapse and proposed downstream effects of calcium diffusion. Calcium entering through either nAChRs or VGCCs can diffuse to and activate calcium-sensitive SK channels. Calcium ions may also bind to and activate calcium-release channels on the synaptic cistern, which is thought to act as a calcium store in hair cells *(From Fuchs, 2000)*.

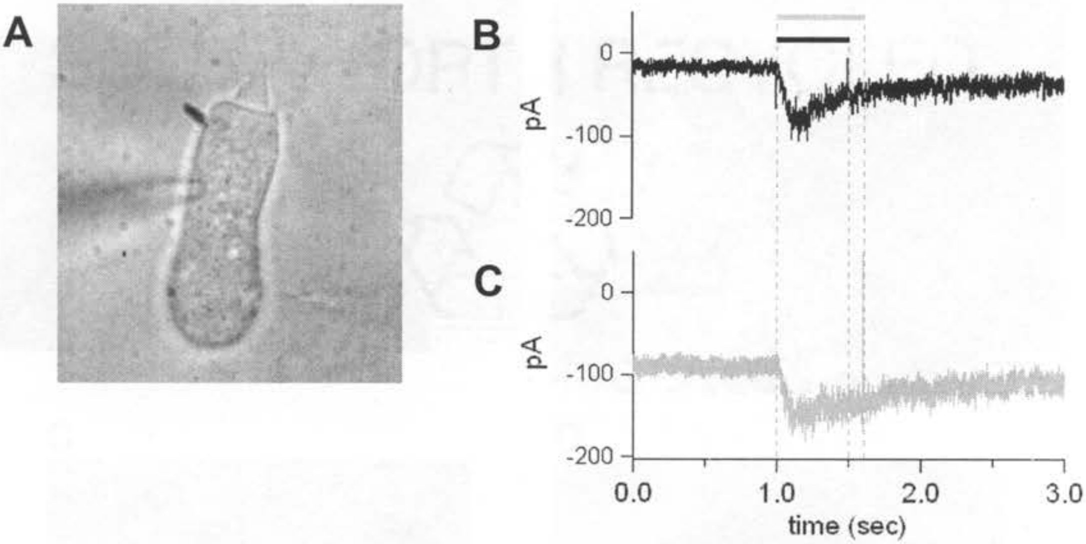

Fig. 40. Examples of the ACh-activated current in frog hair cells. A, Brightfield image of an isolated bullfrog saccular hair cell. Whole-cell voltage-clamp pipette is on the left, the ionophoretic pipette is on the bottom, right ~1 micron away from the cell surface. B, Current response to 500 ms ionophoretic application to 1 M ACh (in water). *Black bar* above the trace indicates the timing of the ionophoretic pulse. C, Current response from a different bullfrog saccular hair cell to a 600 ms application of 100 μM ACh by microperfusion through a 1 μm tip perfusion pipette. *Grey bar* above the current trace in *B* indicates the timing of the microperfusion of ACh in *C*. Both current traces in *B* and *C* have been smoothed 3x. Both cells represented in *B* and *C* were acutely isolated on different days using subtilisin and EGTA and were dialysed with internal solution that contained 0.1 mM EGTA but not cesium or TEA to avoid blockade of potassium channels.

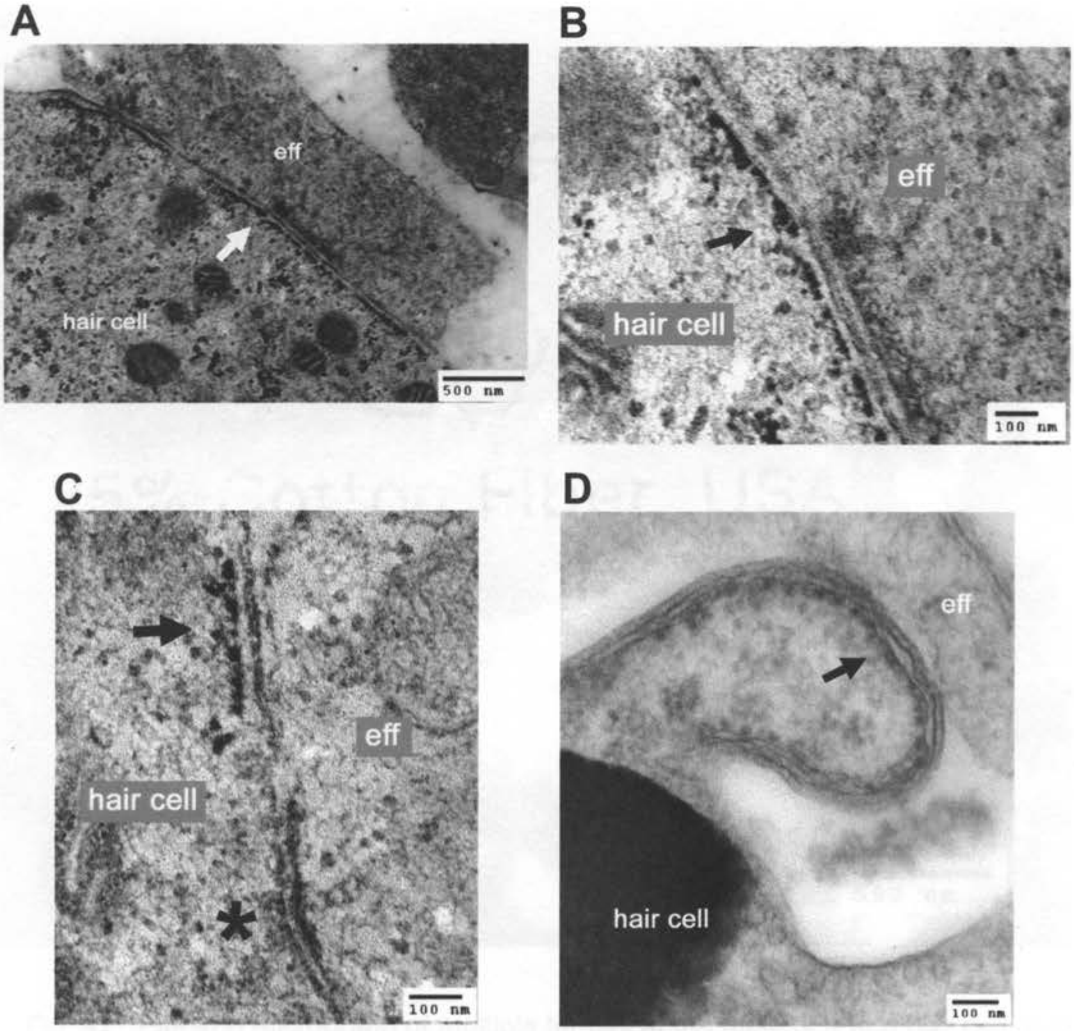

Fig. 41. Electron micrographs of subsurface structures opposite presumed efferent terminals in frog hair cells. A, Subsurface structure beneath the hair cell membrane, *arrow*, opposite the length of a presumed efferent terminal is likened to rough ER. B, Image is a smaller region in *A* at a higher magnification. The *black arrow* in *B* points to the same structure that the *white arrow* in *A* points to. C, Another example in a different cell. Note that the rough ER-like structure is present at only one region, *arrow*, and not another region at the interface between the hair cell and the presumed efferent terminal, *asterisk*. D, A third example from a third cell. Note the presence of a membranous structure associated with the electron-dense rough ER-like structures that is not apparent in the other cells, *arrow*. The large electron-dense structure at the lower left corner appears to be a dense body.

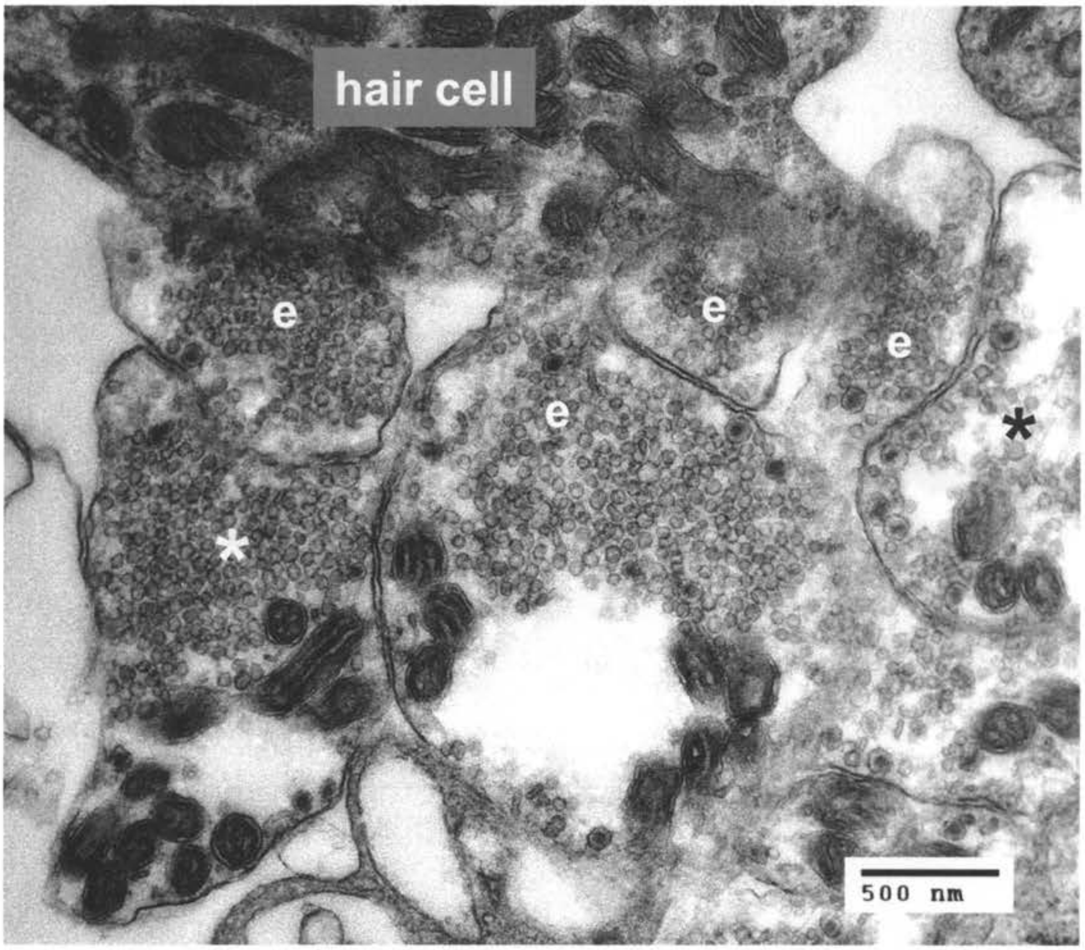

Fig. 42. Electron micrograph of multiple termini at the base of a frog hair cell. Hair cell base (*hair cell*) is contacted by multiple vesicle-filled termini. It is unclear whether there are any synaptic cisternae underneath the postsynaptic membrane opposite vesicle-filled termini, presumably efferent, appearing to contact the base of the hair cell (*e*). Some vesicle-filled termini appear to form synapses with presumed efferent termini (*asterisks*).

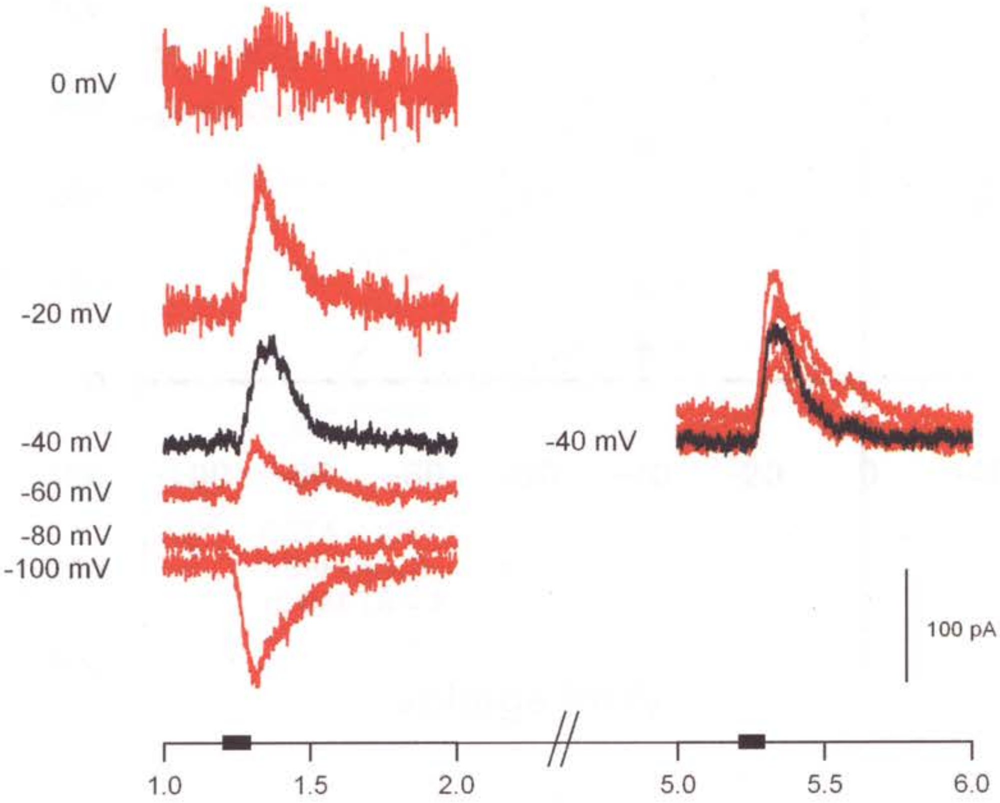

Fig. 43. Example of a typical voltage-sensitive current response to ACh in an isolated chicken cochlear hair cell. Traces on the *left* are the responses to microperfusion of ACh at various test voltages and traces on the *right* are the responses following each trace shown on the *left* at -40 mV. The black traces on the *left* and *right* are the first two responses to ACh in this figure, both at a holding potential of -40 mV. 100 μM ACh was applied with 3-5 psi pressure through a 3-5 MΩ pipette, indicated by *bars* on the x-axis.

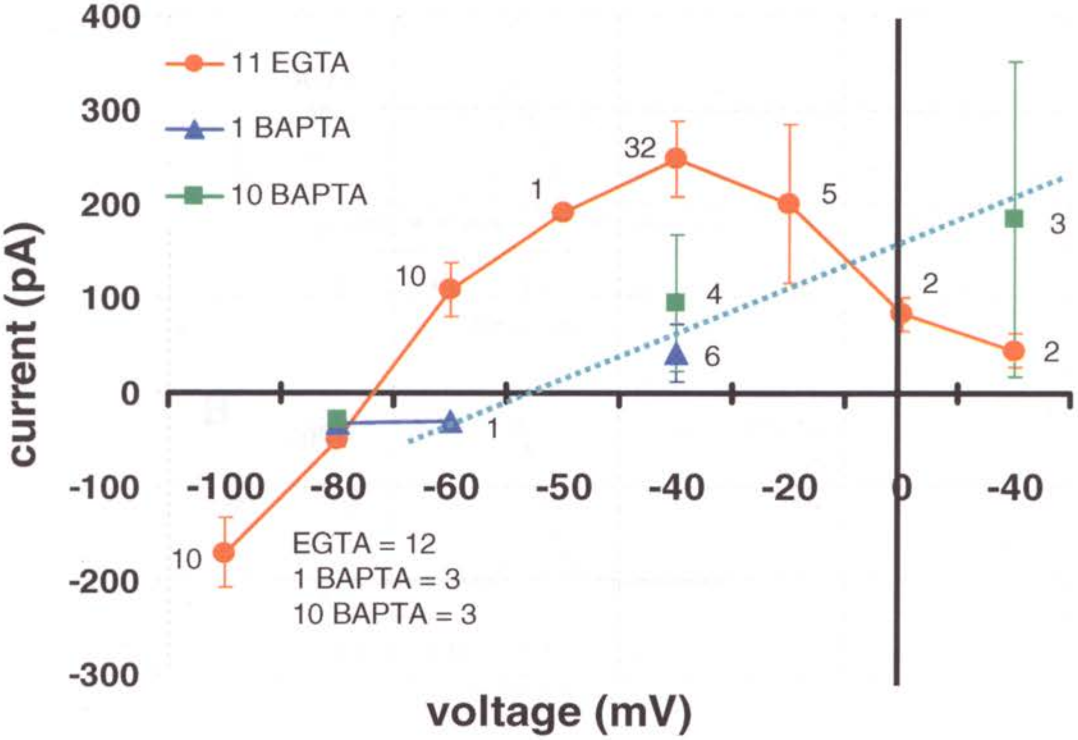

Fig. 44. The effect of calcium buffer on ACh-induced currents in chick hair cells. IV plot of the ACh response in chick cochlear hair cells dialysed with either 11 mM EGTA, *orange squares*, 1 mM BAPTA, *blue triangles*, or 10 mM BAPTA, *green squares* are shown. Numbers next to each data point indicate the number of cells that contributed one measurement. Only one current response to a given voltage step per cell was included in the data set. Some cells, however, may have contributed more than one current response if each response was to a different voltage step. If a cell was brought to the same voltage more than once, only the first response to that voltage was included in the data set. No cell was filled or re-filled with more than one type of calcium buffer. Total number of cells used for this plot was 43. *Error bars = +/- SE.*

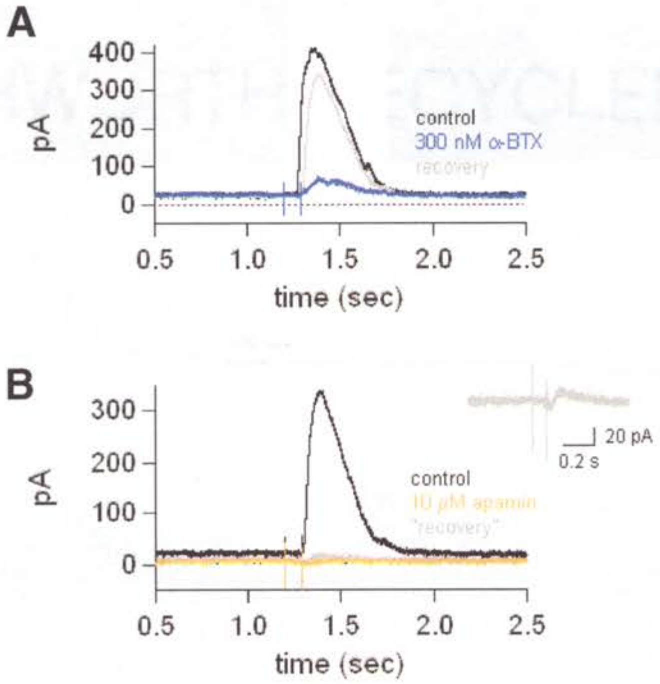

Fig. 45. ACh response is sensitive to α-BTX and apamin. Recordings shown were made in an isolated chick SHC. Blockade of nAChRs was tested with 300 nM α-BTX and blockade of SK channels was tested with 10 μM apamin. A, *black*, control; *blue*, α-BTX; *grey*, recovery from α-BTX. B, *black*, control (same trace as shown in *A, grey*); *yellow*, apamin; *grey*, minimal recovery from apamin. *Inset*, Expanded "recovery" trace. Note slight inward current, possibly the remaining nAChR current.

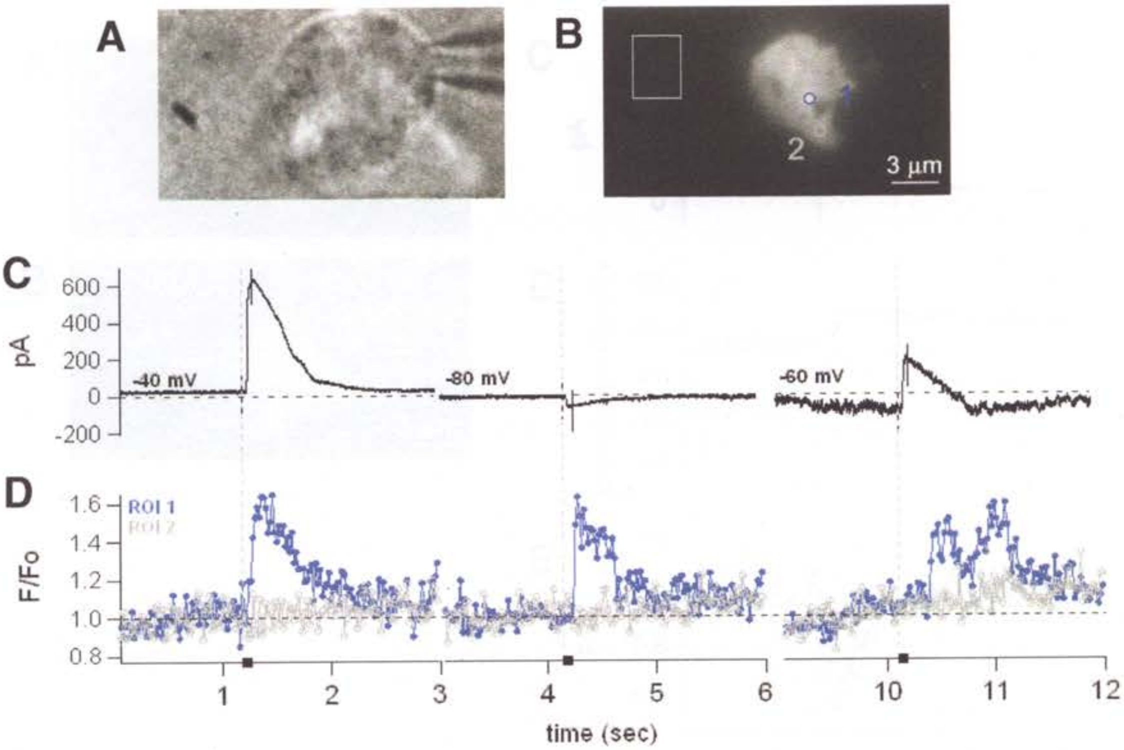

Fig. 46. TIRF imaging and voltage clamp recordings of responses to ACh in an isolated chick hair cell. ACh-induced increases in Fluo-4 fluorescence intensity measured with TIRF and voltage-sensitive current responses to ACh in an isolated chick SHC. A, bright-field image of SHC, base of cell is on the glass and the hair bundle is out of focus pointing up from the glass toward the viewer. B, footprint of the cell with regions at the same magnification scale as *A. Scale bar = 3 µm.* C, corresponding current responses to multiple 90 ms ACh puffs applied at different holding potentials. D, *Blue trace* shows the glass-subtracted and normalized ACh-sensitive Fluo dye fluorescence intensity increase measured in ROI 1. Note the lack of voltage sensitivity of the ACh response. Measurement of a non-responding area of the footprint within ROI 2, *grey trace*, does not exhibit a change in fluorescence intensity with ACh. *Black bars* in the x-axis indicate the timing of each 90 ms ACh microperfusion.

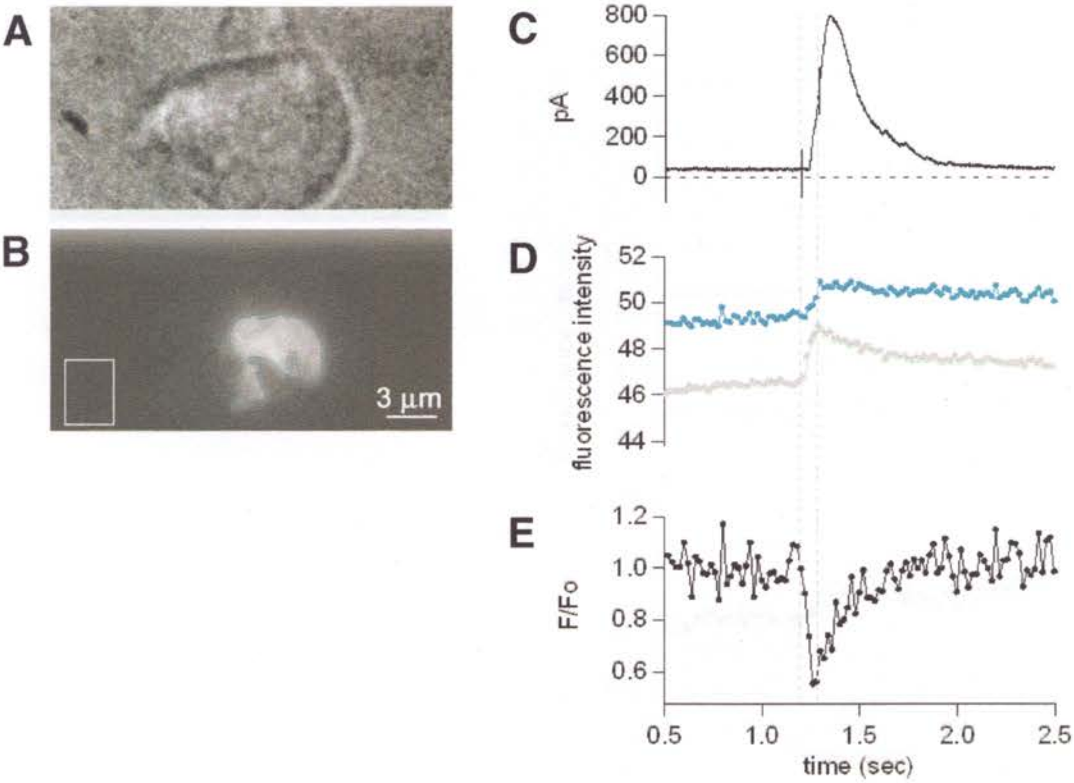

Fig. 47. An increase in whole-footprint fluorescence is not detected in most ACh-responsive hair cells. Glass fluorescence subtraction from the footprint fluorescence in a cell that is electrophysiologically responsive to ACh but does not exhibit an ACh-dependent increase in intensity. A, Brightfield image of SHC, cell is resting on its side on the glass and the hair bundle is pointing upwards in the image. B, Footprint of the same cell in *A* with the footprint region (blue) and glass region (white) drawn. C, Corresponding current response to a 90 ms 100 µM ACh puff at 1.2 sec. D, Traces show the non-glass-subtracted fluorescence traces of the footprint (blue) and of the glass (grey) regions in time. E, The F/F_0 trace following subtraction of the *grey* trace from the *blue* trace in *D.*

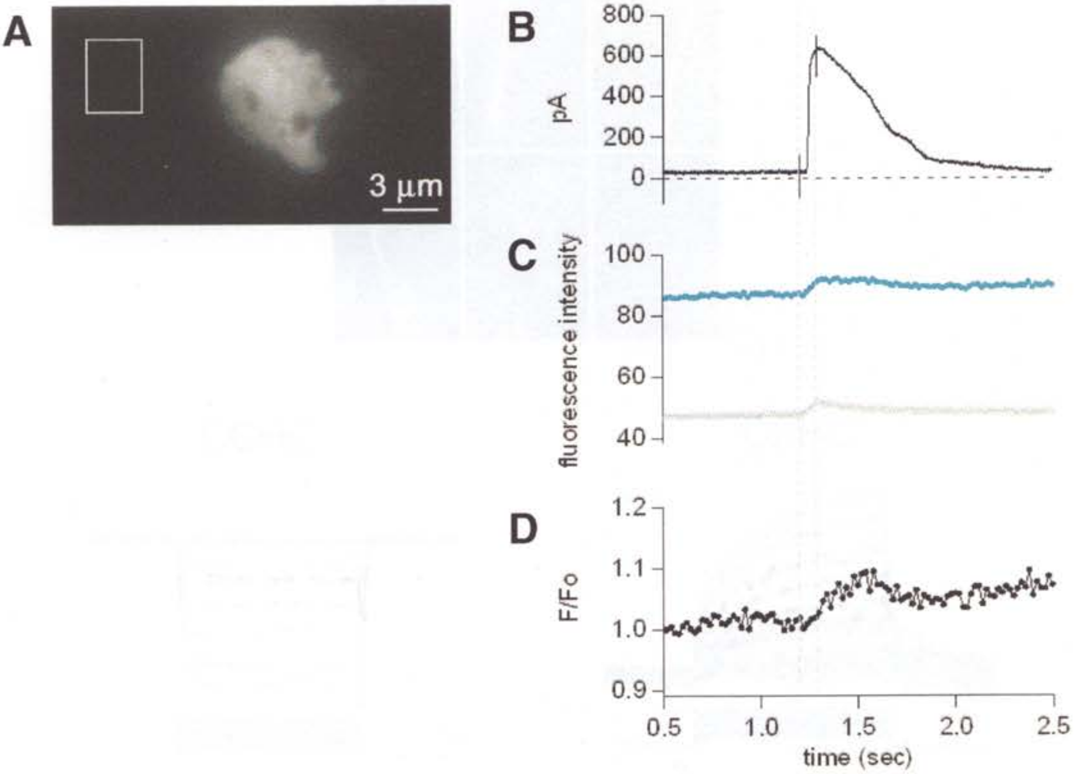

Fig. 48. An increase in whole-footprint fluorescence is detected in the one cell that exhibited a localized fluorescence increase. Subtraction of the glass fluorescence from footprint fluorescence in a cell that is both electrophysiologically responsive to ACh results in a general increase in footprint fluorescence. A, Footprint of the same cell shown in *Fig. 47* with the footprint region (blue) and glass region (white) drawn. B, Corresponding current response to a 90 ms 100 µM ACh puff at 1.2 sec. C, Traces show the non-glass-subtracted fluorescence traces of the footprint (blue) and of the glass (grey) regions in time. E, The F/F$_0$ trace following subtraction of the *grey* trace from the *blue* trace in *D.*

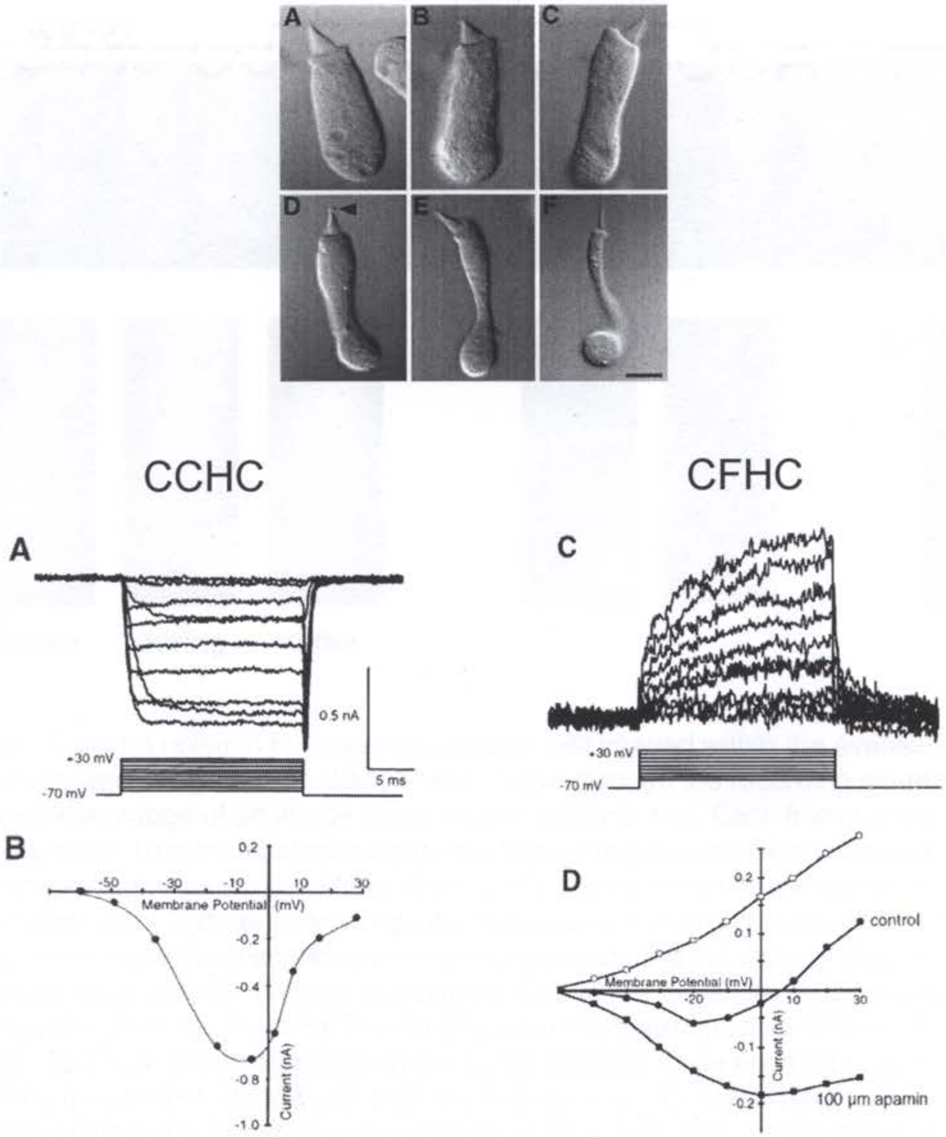

Fig. 49. Only the CFHC bullfrog saccular hair cell type exhibits an apamin-sensitive current. *Above*, A – F, DIC images of three bullfrog saccular hair cell types. A-C = central, cylindrical hair cell (CCHC). D and E = central, flask hair cell (CFHC), F = peripheral, elongated hair cell (PEHC). *Below,* A and B, Current traces for the CCHC type. *Below*, C and D, Current traces for the CFHC type. The CFHC type has an apamin-sensitive current, whereas the CCHC type does not (*From Chabbert, 1997).*

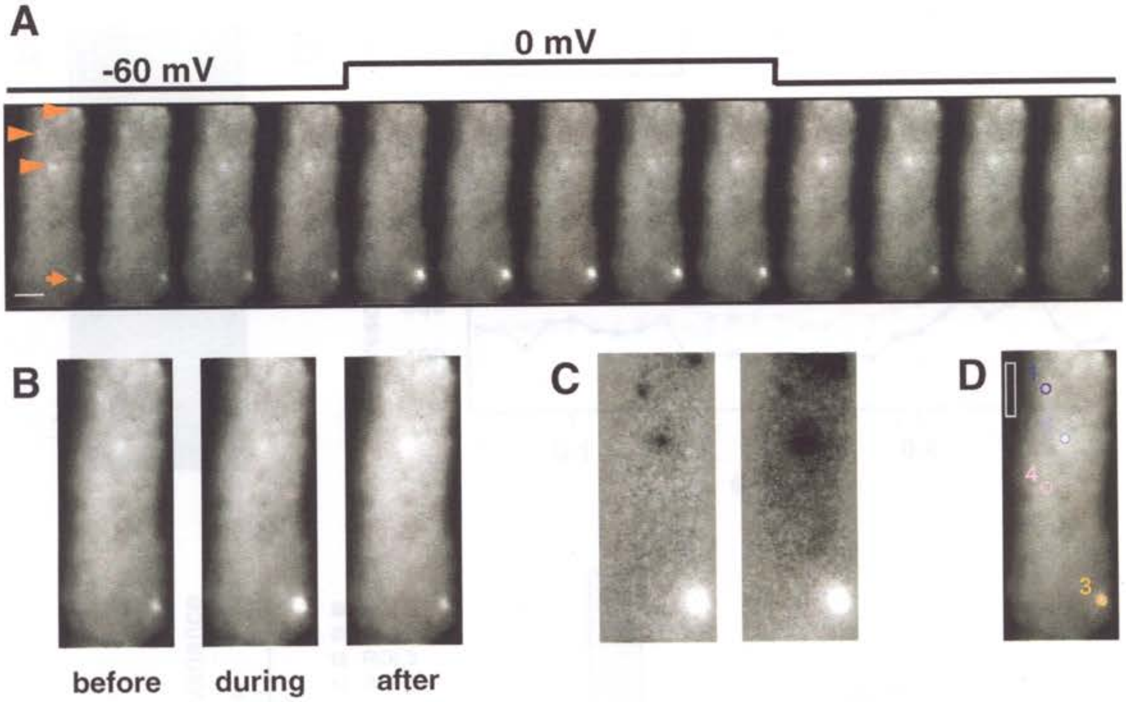

Fig. 50. Calcium noise in bullfrog saccular hair cell imaged within the evanescent field. Cells were dialysed with 200 µM Fluo-3 dye through the recording pipette. A, Sequential montage of an image stack shown at 25 Hz and. Each frame at the same intensity scale. Numbers below indicate the time in milliseconds and *asterisks* indicate when the voltage was stepped from -60 to 0 mV. *Arrow* points to the dense body and *arrowheads* point to three sites where the fluorescence intensity fluctuates. Note that as the dense body fluorescence intensity increases during the voltage step, the sites of calcium noise initially diminish in intensity. One of the three site regains activity whereas the other two increase in intensity upon membrane repolarization. *Scale bar* = 3 µm. B, Three image averages at the same intensity scale each representing 180 ms of the time before, during and after the voltage step. C, *left*, Subtracted image of the "before" from the "during" average image shown in *B*, *right*, subtracted image of the "after" average from the "during" average shown in *B*. Each subtracted image had 1000 pixel intensity units added to every pixel to avoid values less than 1 and scaled to the same intensities. Note that the dense body indicated in *A* is seen as a bright spot and the calcium noise sites also indicated in *A* are seen as dark spots in the subtracted images. D, Circular 5 x 5 pixel ROIs were drawn over the footprint image: ROI 1 (*blue*) and ROI 2 (*lt. blue*) indicate two of the three sites of calcium noise; the third site was too close to the image edge and was left out of the analysis, ROI 3 (*yellow*) dense body and ROI 4 (*pink*) neutral footprint region. A rectangular 5 x 24 pixel region was drawn over the glass where there was no cell, *white*. All images are the same scale as indicated in *A*.

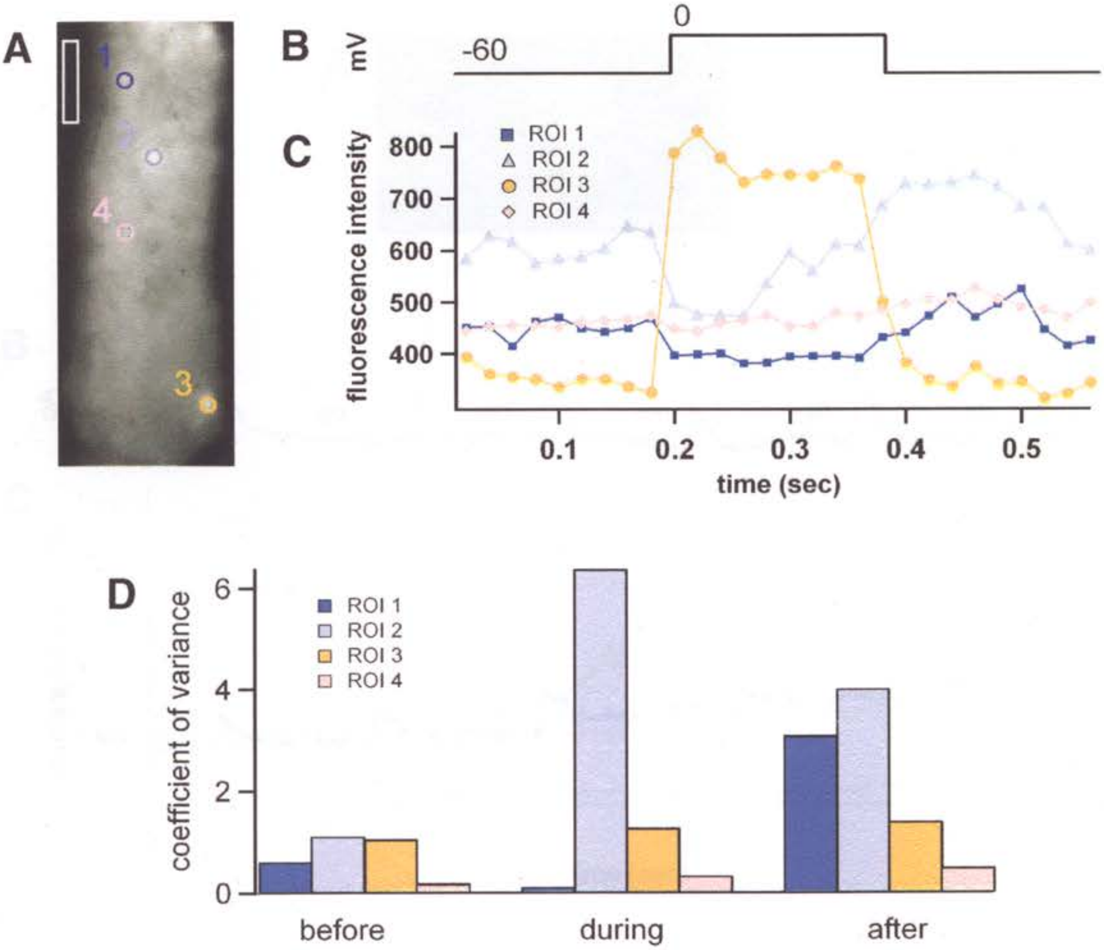

Fig. 51. The influence of membrane voltage on calcium noise in a bullfrog saccular hair cell. A, The same image with ROIs drawn as shown in *Fig. 1D*. B, Timing of the 180 ms voltage step from -60 to 0 mV. C, Glass subtracted fluorescence intensities at ROI 1 – 4 over time in the same time scale as *B*. Note the initial increase in fluorescence intensity at the dense body (ROI 3, *yellow circles*) and the decrease in intensity at ROI 1 (*blue squares*) and at ROI 2 (*lt. blue triangles*) follow the change in membrane voltage within 20 ms. ROI 2 begins to increase in intensity after 80 ms from the start of the voltage step whereas ROI 1 remains at a constant lowered and non-fluctuating intensity until the end of the voltage step. ROI 4 (*pink diamonds*) remained at a relatively constant intensity throughout the recording. D, Coefficient of variance (CV) at the four ROIs during the time before, during and after (180 ms each before (frames 1 – 9), during (fr. 10 – 18) and after (fr. 20 – 28). One frame immediately after the end of the voltage step was left out of the analysis). Note that the CV remains relatively constant at ROI 3 and 4 despite a large increase in intensity at ROI 3.

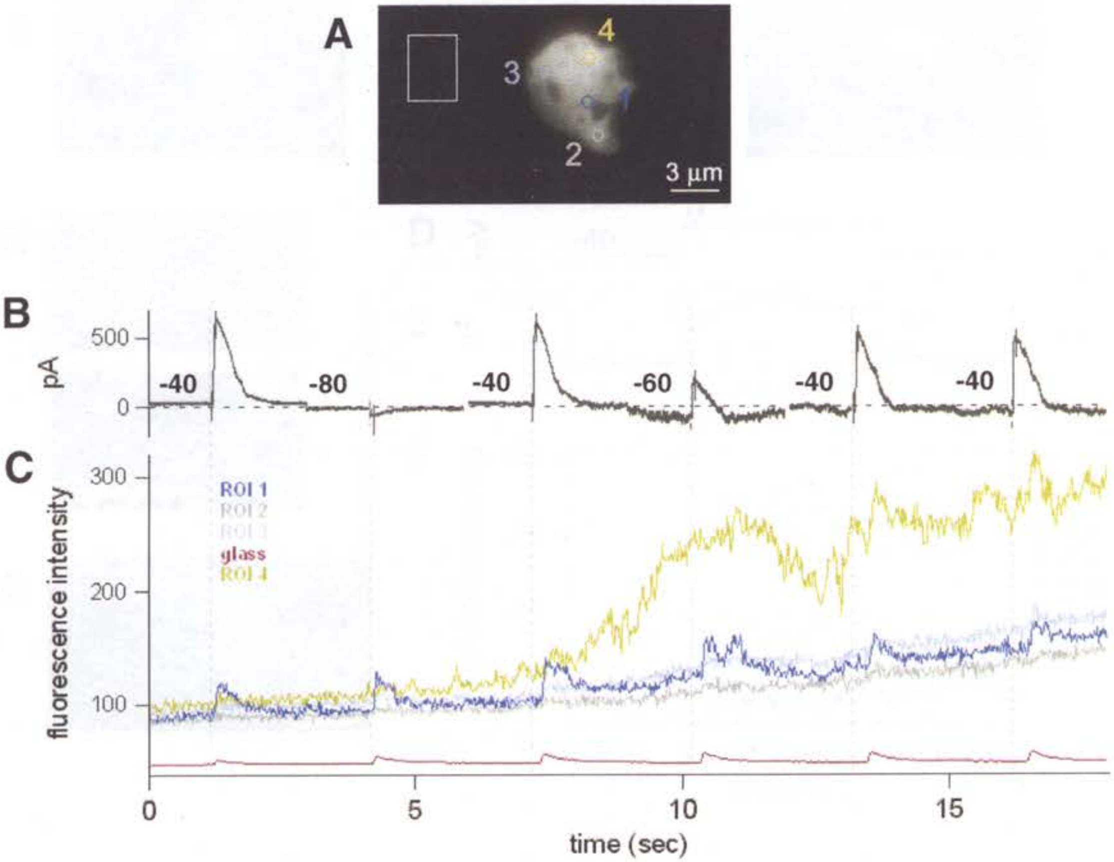

Fig. 52. Localized development of calcium noise in a chick hair cell. This is the full recording of the same experiment shown in Ch. III, Fig. 48. A, Same image and ROIs shown in Ch. III, Fig. 48 (*ROI 1 (blue)*, ACh responding site and *ROI 2 (grey)*, ACh non-responding site) with the addition of two more ROIs: ROI 3 (*lt. blue*) drawn over another non-responding footprint site and ROI 4 (*yellow*) drawn over a site where calcium noise slowly develops. B, Current responses to successive 90 ms ACh (100 µM) puffs applied every 3 sec starting at 1.2 s. Membrane voltage is changed every 3 sec as indicated. C, Non-glass-subtracted fluorescence intensity traces at each of the regions drawn in *A*, including the glass region, *purple trace*. Note that at ROI 4, an increase in fluorescence intensity and degree of fluctuation is seen but not within the other regions.

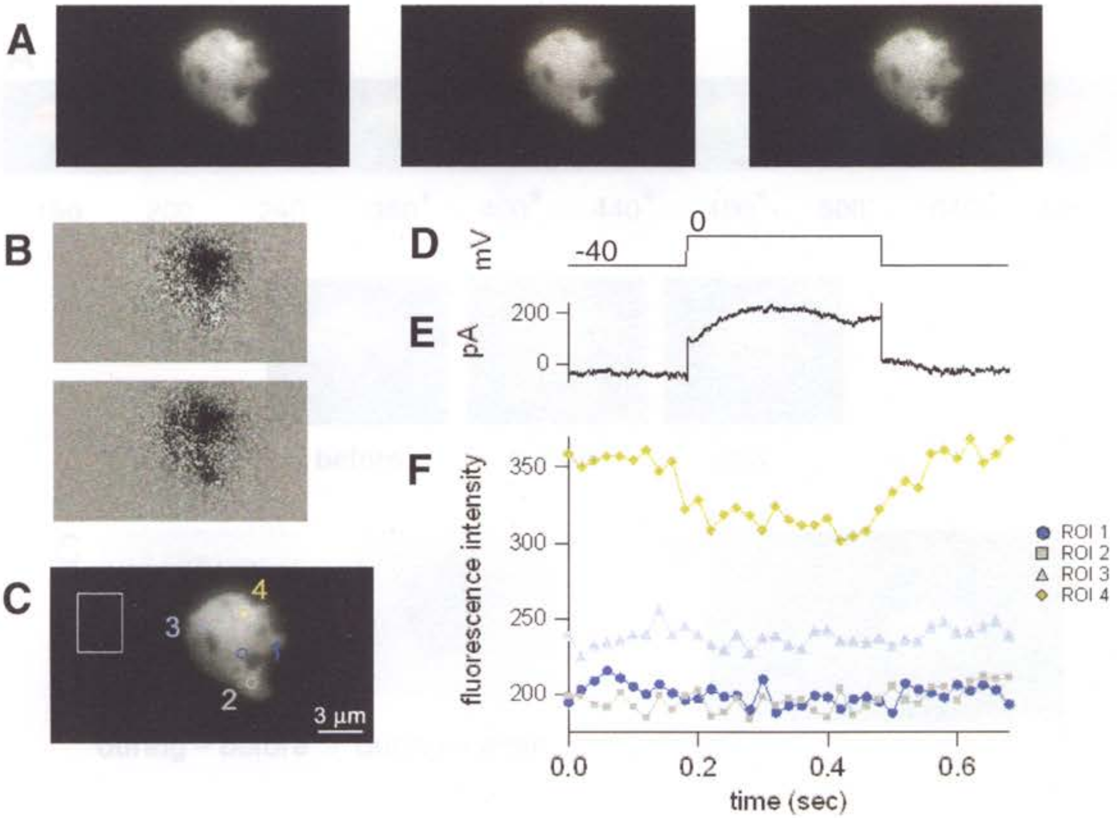

Fig. 53. Further analysis of localized site of calcium noise. Image subtraction and whole-cell V clamp recordings to illustrate the influence of membrane voltage on the fluorescence intensities at various regions drawn within the footprint. A, Image averages of the time before, during and after (*left*, *middle* and *right*, respectively) the voltage step each 200 ms. All three images have the same intensity scale. B, *upper*, Subtracted image of the "during" minus the "before" averages shown in *A*, lower, subtracted image of the "during" minus "after" averages shown in *A*. Both subtracted images have the same intensity scale. C, Same image with ROIs as shown in *Fig. 53 A*. D and E, A 300 ms voltage step from -40 to 0 mV and corresponding current trace, respectively. F, Glass-subtracted fluorescence intensities at ROI 1 – 4. Note that a voltage step from -40 to 0 mV results in diminished fluorescence intensity only at ROI 4, the site of calcium noise illustrated in *Fig. 52 C*, but not at the other three ROIs, including the site that responded to ACh puff (see *Chapter III*, *Fig. 47*).

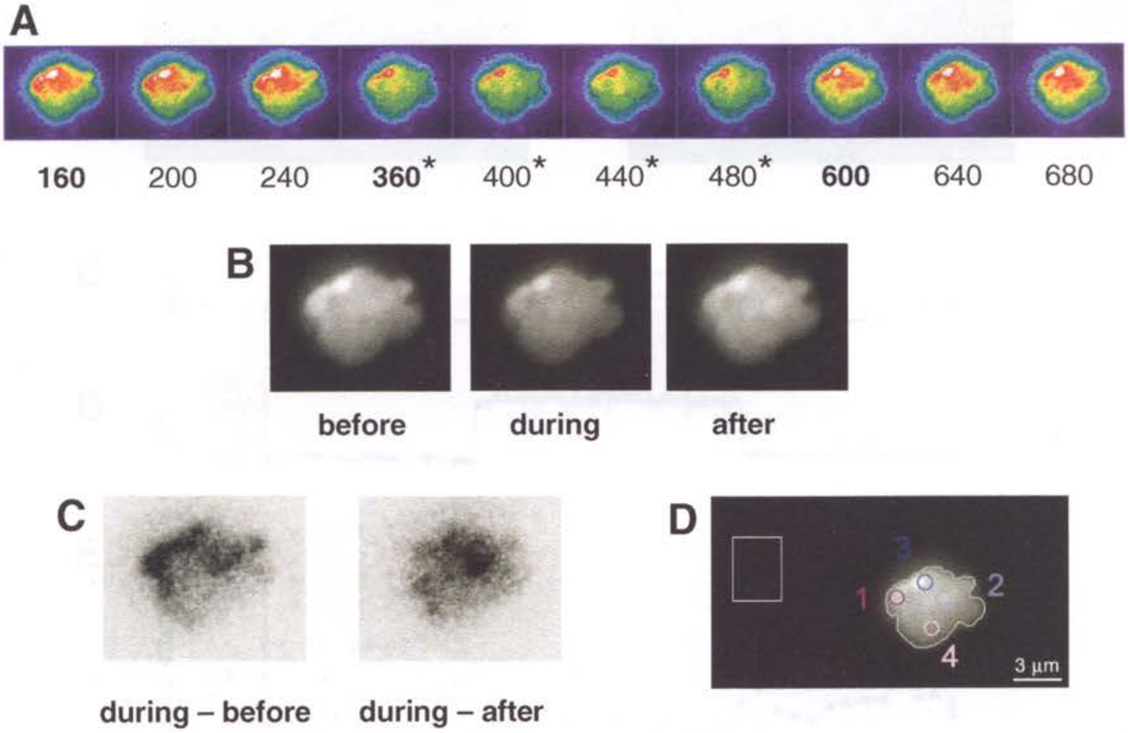

Fig. 54. Image subtraction of calcium noise in another chick SHC. A, depicts a montage of 40 ms images of the footprint by TIRF microscopy over time. Times below each frame indicate the time of each acquisition (in ms). The first frame following a gap in the image sequence is shown in ***bold***. *Asterisks* indicate the timing of the voltage step from -40 to 0 mV. Each image is scaled to the same range of intensity. B, image subtraction of 240 ms averages taken before, during and after the voltage step. Each image is scaled to the same range of intensity. C, Subtracted images as indicated below each image. Note that the dark spots before and after the voltage step are in different places and that the whole footprint is generally darker than background glass. Both images are scaled to the same range of intensities. D, Circular 10 x 10 pixel ROIs drawn over sites in the footprint determined by the subtracted images in *C*. Pixel size = 67 nm, *scale bar* = 3 µm.

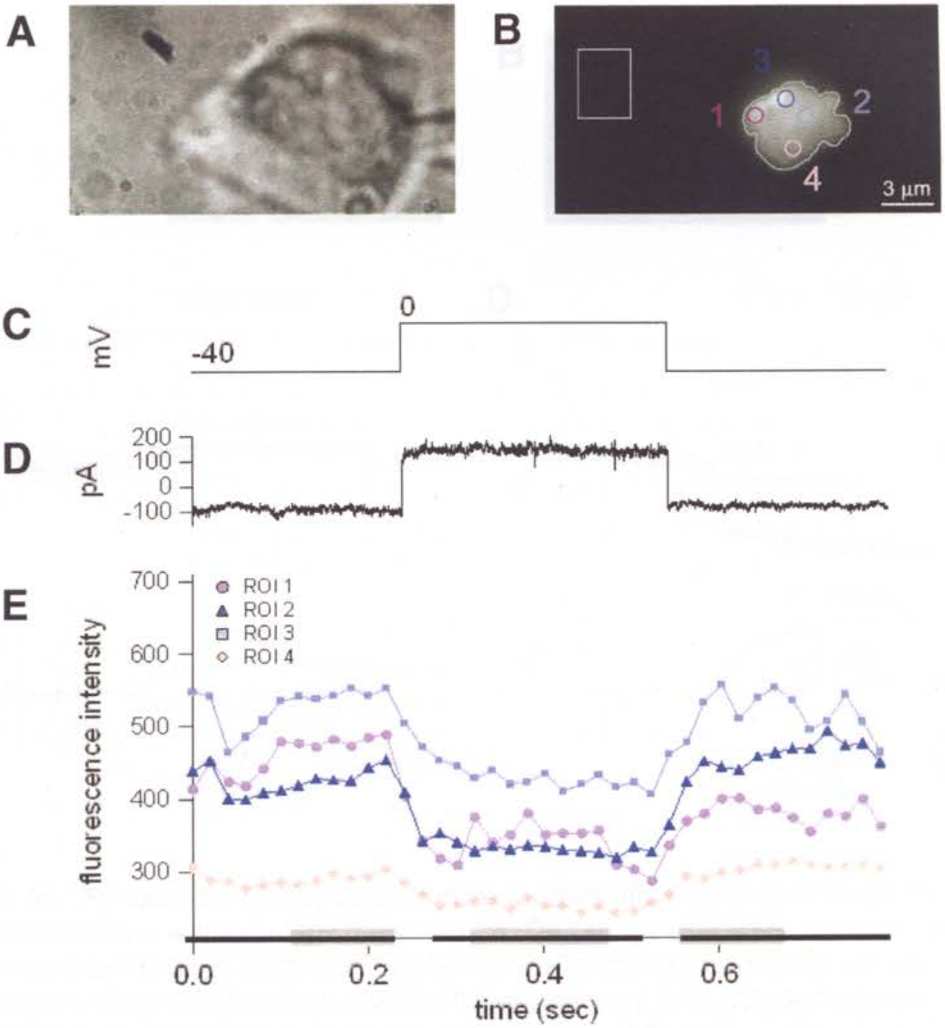

Fig. 55. The effect of membrane voltage on calcium noise localized throughout the footprint. A, DIC image of isolated chick SHC resting on its side and the voltage-clamp recording pipette on the right. ACh perfusion pipette pointing toward the cell from the left is not shown. B, Same image as shown in *Fig. 5 B* depicting the regions used for the measurement of fluorescence intensity over time. C, Timing of the 300 ms voltage step from -40 to 0 mV. D, Current response to the voltage step. E, Plot of the glass-subtracted fluorescence intensities at various 10 x 10 pixel ROIs, ROI 1 (*purple*), ROI 2 (*light blue*), ROI 3 (*blue*) and ROI 4 (*pink*). Each point is the fluorescence of the ROI minus the fluorescence intensity of the rectangular 30 x 40 pixel in the same image frame. *Black bars* on the x-axis indicate the frames that were shown in the montage of *Figure 54 A* and the *grey bars* indicate the frames used for the image averages shown in *Fig. 54 B.*

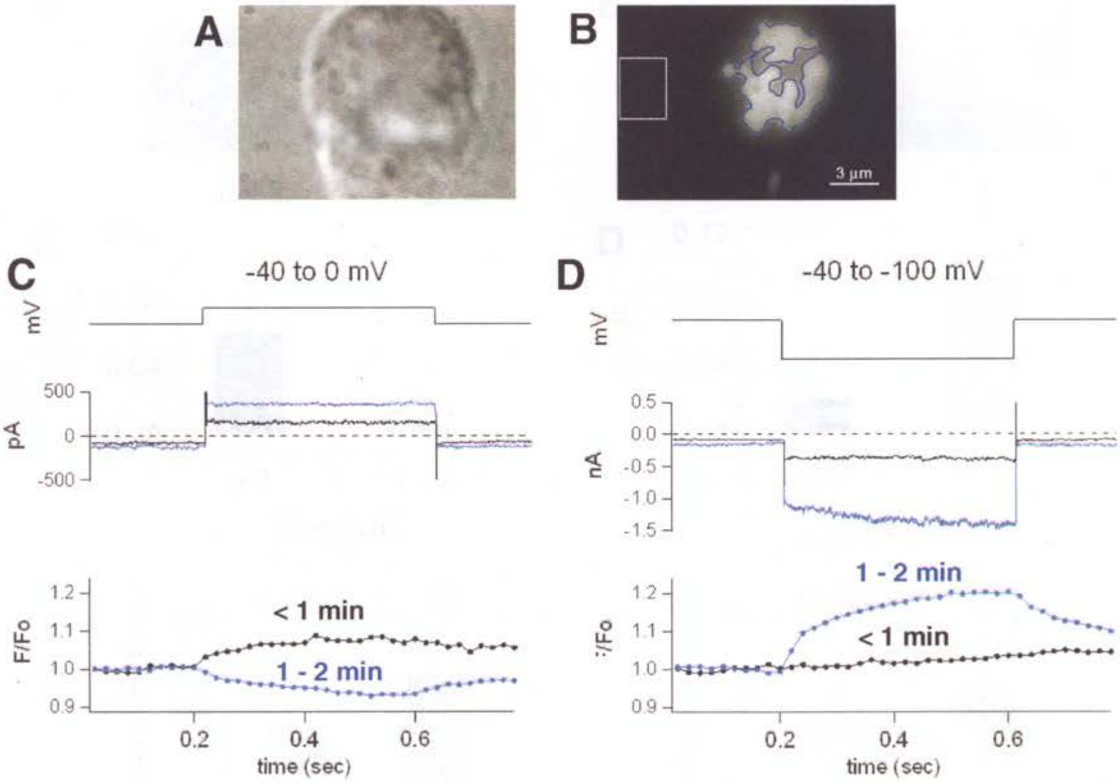

Fig. 56. An example of changes in whole-footprint fluorescence in response to two membrane voltage steps over time. A, DIC image of a chick cochlear SHC attached to the glass such that the hair bundle is facing towards the viewer. B, Footprint of the cell illuminated within the evanescent field. Whole footprint fluorescence intensities were measured within the ROI drawn along the perimeter in *blue*. A rectangular 30 x 40 pixel region, *white*, was drawn over the glass where there was no cell. Both *A* and *B* to same scale; *Scale bar = 3 µm*. C, *top*, depicts the 200 ms voltage step from -40 to 0 mV used in this experiment; *middle*, whole-cell current responses to the voltage step to 0 mV applied within 1 min (*black trace*) and between 1 – 2 min (*blue trace*); *bottom*, whole footprint F/F_0 responses to the same voltage step to 0 mV also applied within 1 min (*black trace*) and between 1 – 2 min (*blue trace*). Note that the slight increase in F/F_0 when the voltage step to 0 mV is applied within 1 min becomes a slight decrease in F/F_0 between 1 – 2 min. D, the same experiment and cell in *C* except that the voltage step is to -100 mV. Note the large increase in the inward current at -100 mV between 1 – 2 min (*blue trace*) in contrast to the response within 1 min (*black trace*). Also note the increase in F/F_0 during the voltage step applied between 1 – 2 min (*blue trace*) that was not there within 1 min (*black trace*).

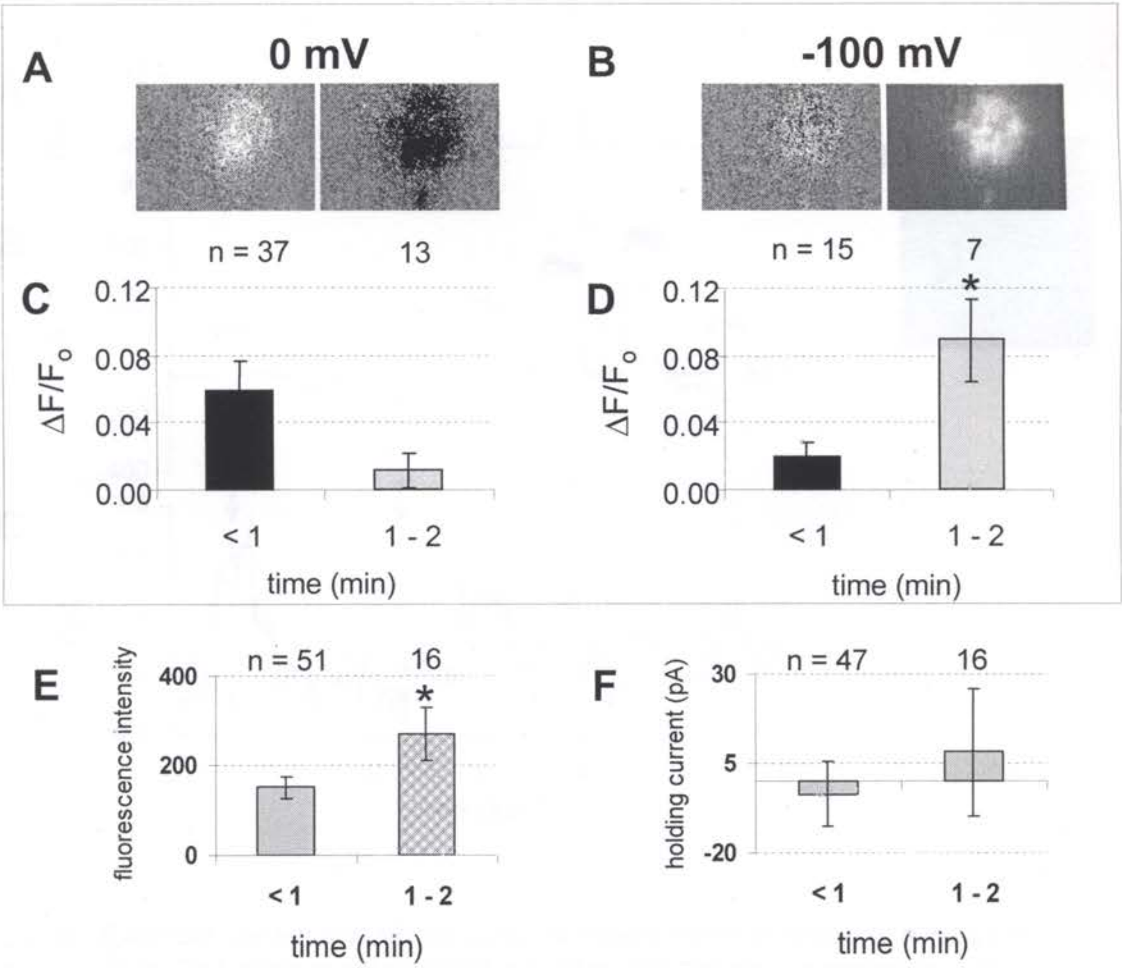

Fig. 57. Pooled whole-footprint $\Delta F/F_0$ responses to membrane voltage in chick SHCs. A, Subtracted images for the same cell shown in Fig. 57. Only the during minus before subtracted image is shown when the voltage step to 0 mV was applied at <1 min, *left*, and between 1 – 2 min, *right*. Images scaled to the same intensity range. B, Same cell, same image subtraction except voltage step was to -100 mV within <1 min, *left*, and between 1 – 2 min, *middle*. Images scaled to the same intensity range as images in *A*. Image at *right* is the same image at *middle* but scaled such as to limit oversaturation in the figure. C. Pooled $\Delta F/F_0$ responses from 43 different cells to voltage step to 0 mV applied within <1 and between 1 – 2 min. $\Delta F/F_0$ was calculated by subtracting the average glass-subtracted footprint intensity within 200 ms before the voltage step from the average intensity within 200 ms during the voltage step. D, Same as in *C* but to -100 mV. In *C and D*, n = number of different cells that contributed to the data point. Only one trace per cell/time point/voltage step was included. *Asterisk* indicates p = 0.003 in *D.* The value for p = 0.123 in *C*. E, Average intensity values for 200 ms at V_{hold} (-40 mV) before every voltage step trace (minus 6 traces) represented in *C* and *D*. F, Average I_{hold} for every trace (minus 9 traces) shown in *C* and *D* for the same 200 ms range used in *E*. The values for p = 0.022 in *E* and 0.52 in *F*. All statistics were calculated using a two-tail, t-Test assuming equal variances.

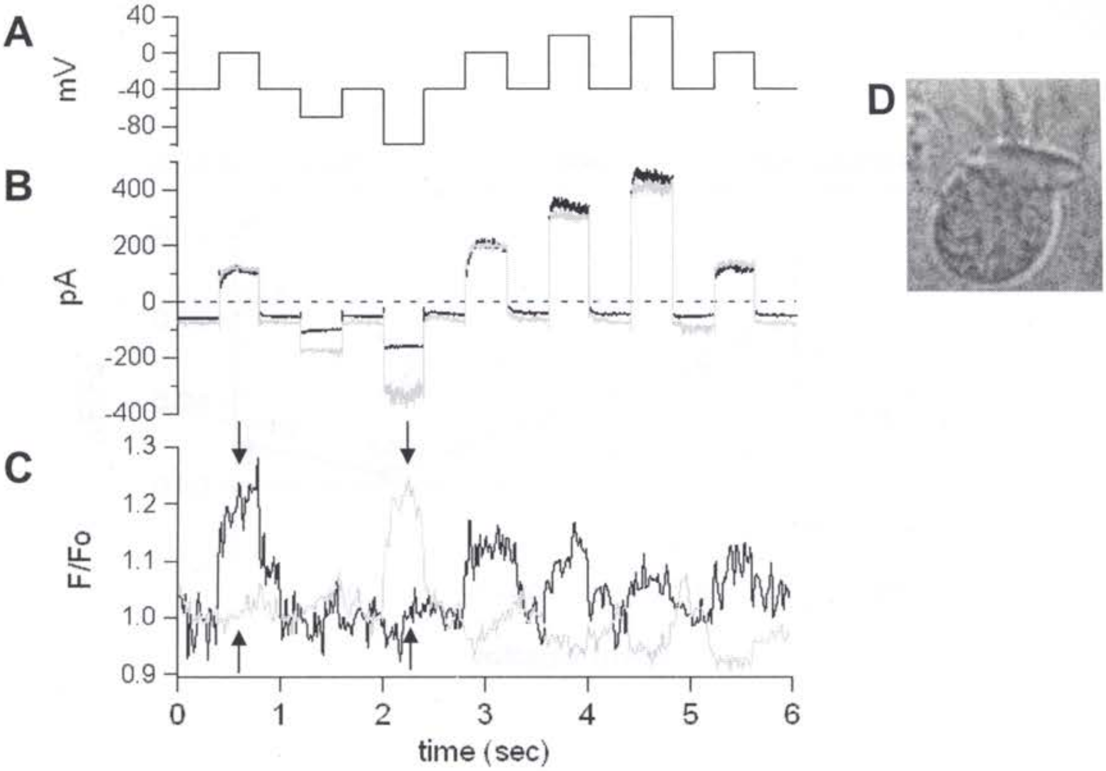

Fig. 58. Example current and whole-footprint fluorescence changes to a range of voltage steps. To further characterize the relationship between membrane voltage and whole footprint, multiple voltage steps were applied to chick cochlear SHCs. A, Example of the 6 sec voltage protocol applied to each cell. The voltage was changed every 400 ms. The membrane voltage was brought back to resting at -40 mV between each test voltage step. B, Example current responses to the voltage protocol above applied at <1 min, *black trace*, and between 1 – 2 min, *grey trace*. Note the increases in inwards currents at hyperpolarized potentials. C, Example footprint F/F_0 responses to the same voltage protocol above at <1 min, *black trace*, and between 1 – 2 min, *grey trace*. Note the loss of a positive F/F_0 response to 0 mV (compare traces between *black arrows*) and the gain of a positive response at -100mV from <1 to between 1 – 2 min (compare traces between *grey arrows*). Also note the negative F/F_0 responses at depolarizing potentials between 1 – 2 min. D, DIC image of the chick SHC recorded from.

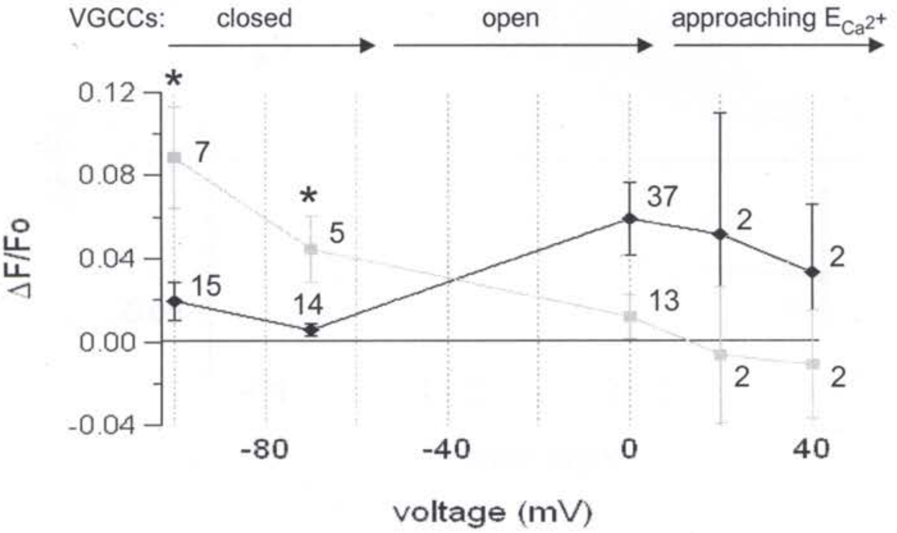

Fig. 59. Plot of pooled whole-footprint $\Delta F/F_0$ in response to a range of voltage steps. Whole-footprint $\Delta F/F_0$ were measured in response to multiple voltage steps applied within either 1 or 1 – 2 min from 43 chick SHCs. $\Delta F/F_0$ vs. Vm plot within 1 min, *black diamonds*, and within 1 – 2 min, *grey squares*. The relationship between footprint $\Delta F/F_0$ and membrane voltage resembles the concentration of cytosolic calcium that would result from calcium influx through VGCCs where channel activation occurs around -50 mV, peaks at around 0 mV and diminishes as the reversal potential for calcium is approached, *black diamonds*. This relationship changes after 1 min of recording and becomes linear in such a way that implies the free passage of calcium ions across the plasma membrane dictated by the driving force for calcium, *grey squares*. *Asterisks* indicate values for $p < 0.05$; The values for $p = 0.003$ at -100 mV and $p = 0.002$ at -70 mV calculated with t-Test, assuming equal variances, two-tail.

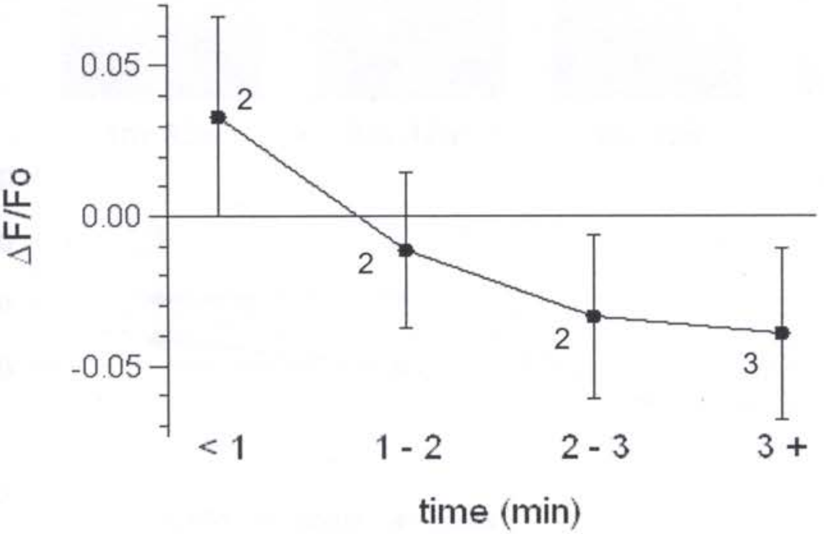

Fig. 60. Pooled whole-footprint $\Delta F/F_0$ responses to +40 mV. Responses were pooled from 3 chick hair cells over 3+ minutes of recording. Image subtraction of the averaged images in a stack before the voltage step from during shows a decrease in the fluorescence intensity of the footprint (not shown, but see *Fig. 58 C, grey trace* at positive membrane potentials). Further time points are plotted here and seem to suggest that calcium is removed from the cytosol within the evanescent field in a voltage-sensitive manner. However, the difference in the responses at <1 and 3+ min had a value for $p = 0.203$ (t-Test assuming equal variances, two-tail) and may not be significant. This decrease in $\Delta F/F_0$ below zero may reflect calcium uptake to basal levels rather than calcium efflux.

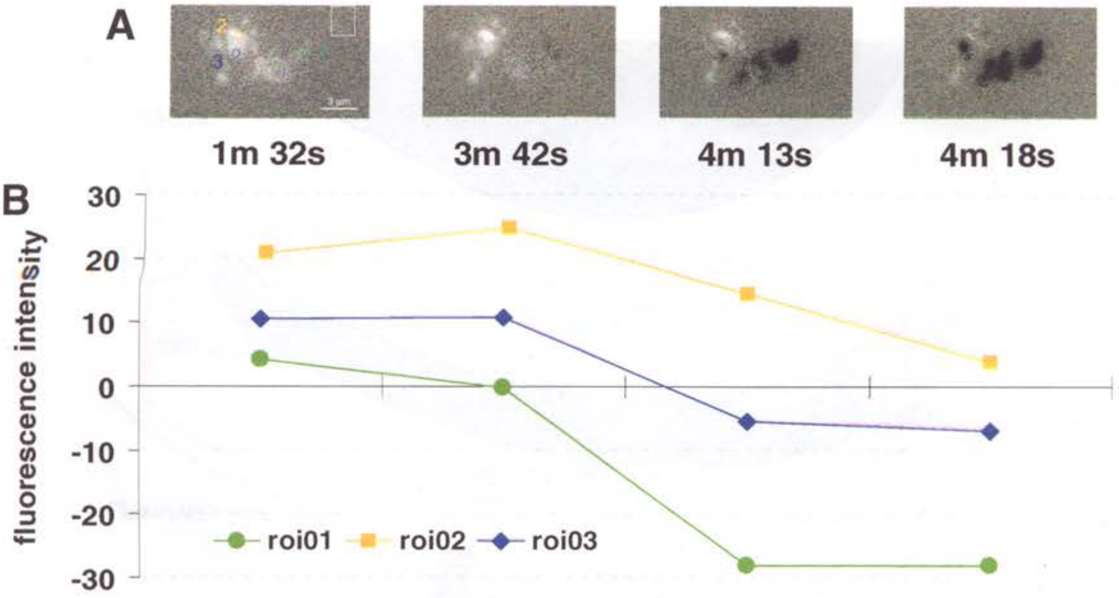

Fig. 61. Asynchronous development of a non-voltage gated calcium flux across the footprint over time. The $\Delta F/F_0$ responses to a voltage step from -40 to 0 mV were measured in three ROIs drawn within the footprint of a chick cochlear hair cell. A, *left-most image*, depicts the regions ROI 1 (*green*), 2 (yellow), 3 (blue) and a 30 x 40 pixel glass ROI (*white*). B, Glass-subtracted fluorescence intensity traces for each ROI drawn in *A* over four successive time points. Corresponding subtracted images ("before" from the "during" image averages of time before and during a voltage step to 0 mV) for each voltage step applied at the times indicated below each image. Times are relative to the first image acquired in the cell.

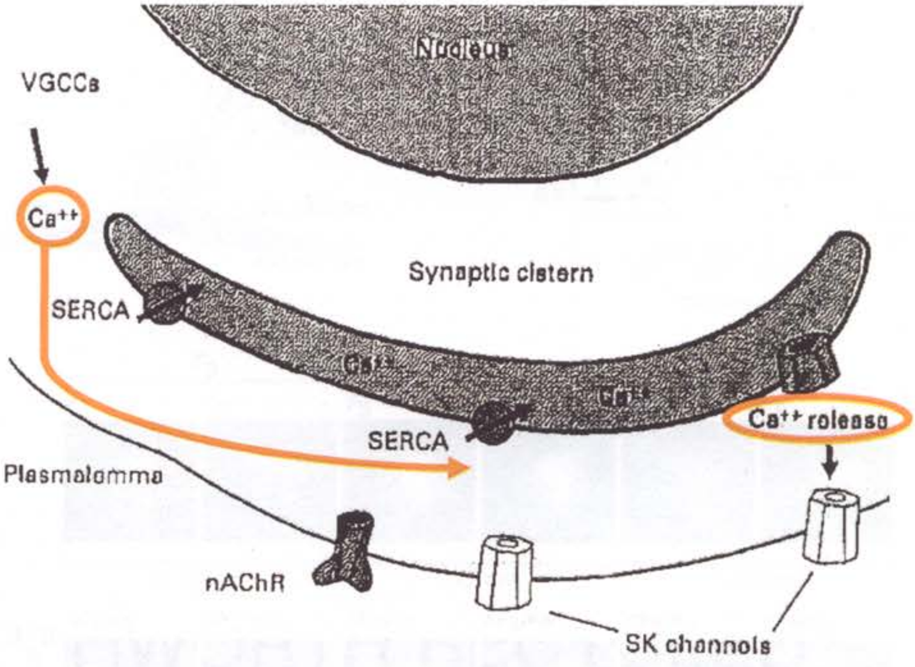

Fig. 62. Illustration to explain the appearance of transient calcium noise events. Stochastic calcium release from calcium store organelles, such as the synaptic cistern may be triggered by an elevated concentration in cytosolic calcium and activation of calcium-release receptors, such as IP_3 or ryanodine receptors. Increases in cytosolic calcium may arise following calcium influx through VGCCs. Alternatively, dialysis of endogenous calcium buffer with a high concentration of EGTA (11 mM was used in these experiments) could also stimulate homeostatic calcium release from store organelles through SERCA transporters found there. Calcium release from store organelles could be visualized by TIRF microscopy (*Adapted from Fuchs, 2000).*

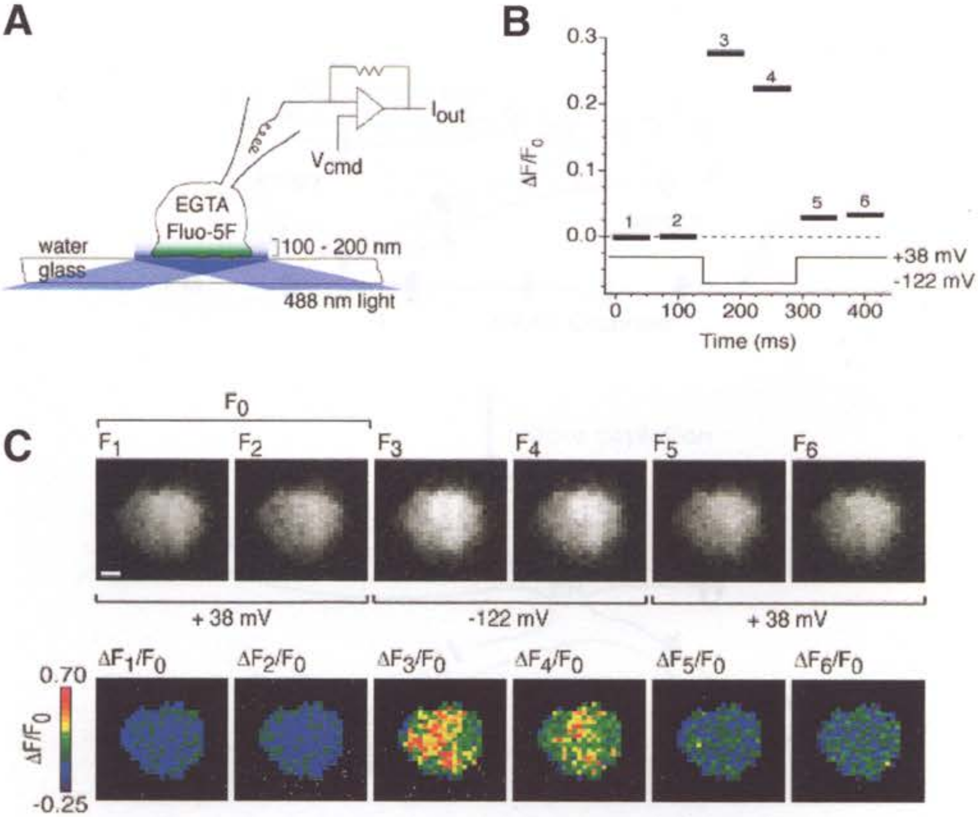

Fig. 63. A non-voltage-gated calcium flux was also observed in Jurkat T cells. Using similar experimental conditions as the experiments presented in this thesis, combined TIRF microscopy and voltage clamp recordings of Jurkat T-cells also reveals a voltage sensitive increase in Fluo dye fluorescence intensity at hyperpolarized potentials. A, Diagram of the experimental setup. B, A voltage step from +39 to -122 mV results in a ~2.5-fold increase in $\Delta F/F_0$ within 10 to 60 ms of the voltage change. C, *upper*, A series of TIRF microscopy images of the Jurkat T-cell footprint with respect to membrane voltage, *lower*, Pseudocolor images of $\Delta F/F_0$ where F_0 is the average of two frames, F_1 and F_2 shown above *(From Luik et al., 2006).*

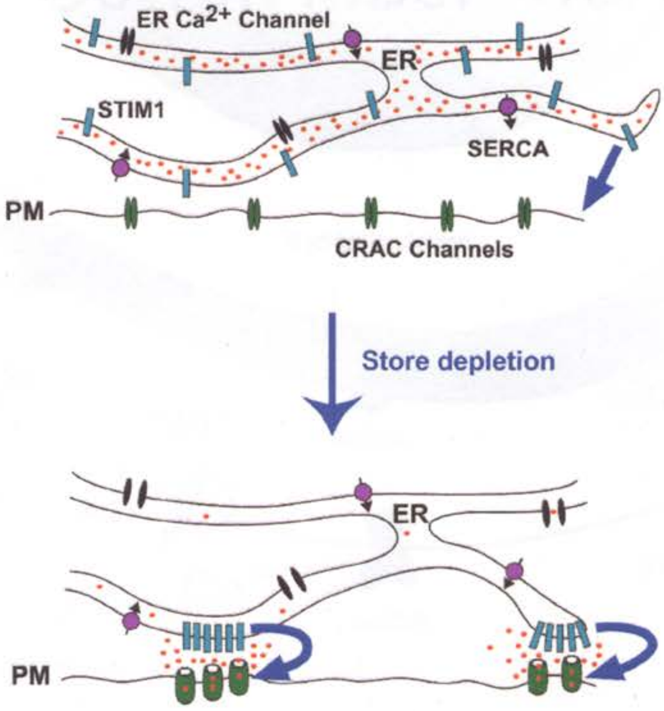

Fig. 64. Cartoon illustrating the formation of SOC channels. Following depletion of calcium from stores, The ER moves toward the plasma membrane such that stim1 molecules in the ER membrane and orai1 molecules co-localize to form SOC channels *(From Luik et al., 2006).*

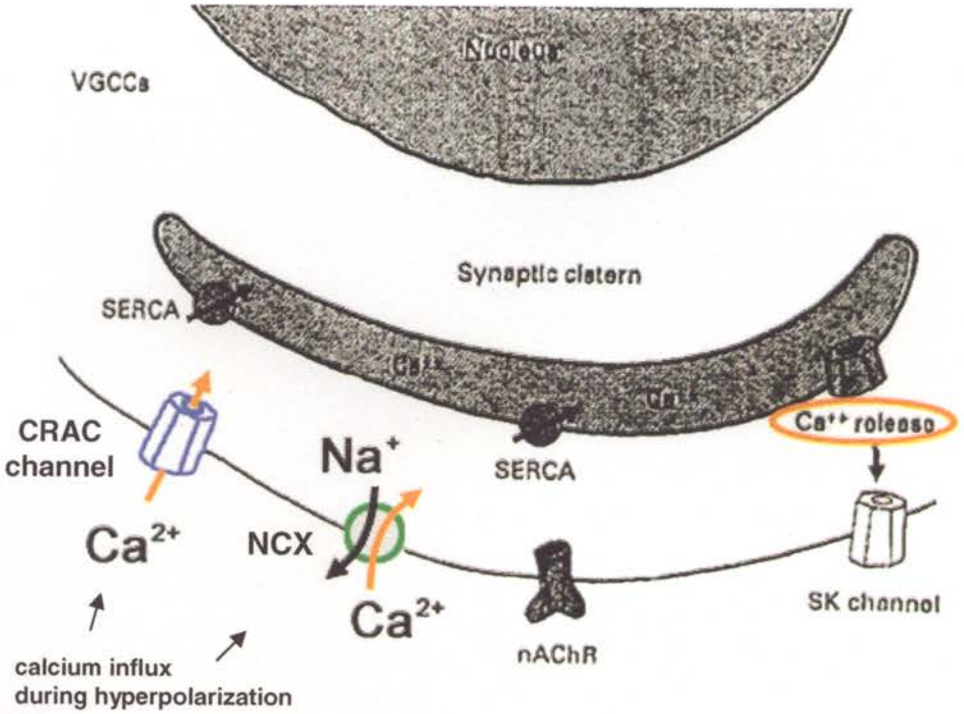

Fig. 65. Alternate explanations for the appearance of calcium noise and for the development of a non-voltage-gated calcium flux. Transient calcium noise events may also reflect stochastic calcium influx through SOC channels, i.e. CRAC channels, in response to depletion of calcium from store organelles following calcium release. The sensitivity of Fluo dye fluorescence intensity to changes in membrane voltage may be explained at least two ways. One is that SOC channels in the plasma membrane are open while voltage steps are applied and calcium ion flux is governed by the driving force for it. Another explanation is that the direction of calcium ion transport, such as through NCX, is influenced by changes in membrane voltage possibly leading to sodium efflux and calcium influx at hyperpolarized potentials or sodium influx and calcium efflux at positive potentials. Since the synaptic cistern and the plasma membrane can both fit within the evanescent field, calcium-permeable channels or transporters found at either site cannot be distinguished in these experiments *(Adapted from Fuchs, 2000).*